ANALYSIS OF FUSION REACTIONS AND SUBSEQUENT DECAY MECHANISMS AT LOW ENERGY REGIME

A THESIS

Submitted in the partial fulfillment of the requirement

for the award of degree of

DOCTOR OF PHILOSOPHY

under the guidance of

Dr. Manoj K. Sharma
(Professor)

by

Ishita Sharma

(Regn. No: 901412015)

School of Physics and Materials Science
Thapar Institute of Engineering and Technology
Patiala-147004, INDIA

February, 2020

Dedicated to

My Family

&

My Supervisor

CERTIFICATE

This is to certify that the thesis entitled "**ANALYSIS OF FUSION REACTIONS AND SUBSEQUENT DECAY MECHANISMS AT LOW ENERGY REGIME**" being submitted by **Ms. Ishita Sharma** for the fulfillment of the requirements for the award of Degree of Doctor of Philosophy in the School of Physics and Materials Science, Thapar Institute of Engineering and Technology, Patiala, is a record of the candidate's own work carried out by her under my supervision. The matter presented in this thesis has not been submitted in part or full for the award of any degree in any university or institute.

Supervisor

11.11.2020

Dr. Manoj K. Sharma

Professor

School of Physics and Materials Science

Thapar Institute of Engineering and Technology (TIET)

Patiala- 147004

Punjab (India)

Acknowledgments

Today I got an opportunity to pen down my sincere thank to God almighty for his abundant grace, enormous blessings and consistent guidance. God, you strengthened me and accompanied me during the odd phases of my life. Without your guidance nothing can be possible for me. Your consistent grace upon me is ineffable, thank you for being with me.

No words can sum up the gratitude that I owe to my supervisor Prof. Manoj Kumar Sharma who has always been a source of motivation and encouragement for me. His expertise guidance, valuable suggestions, constructive criticism and scientific wisdom flourished my knowledge and growth as a student. His motivational speeches and working spirit create a healthy environment in the lab and inspires us to work hard throughout the research work. His very common dialogue "Dhoondne se to bhagwan bhi mil jatey hain" (If one searches intently enough he can find God too) taught us to never give up in any situation. His challenging questions and careful editing polished my learning and writing skills to great extent. Apart from professionalism, he is an extraordinary human being with kind and exemplary heart. I am always thankful to him for believing in me and supporting me at all the time of my thesis work. I also express my sincere gratitude to Sonam maam for her motherly care, love and affection.

I wish to express humble and special thanks to Dr. Raj Kumar for his valuable suggestion, enduring knowledge, timely corrections, and scholarly guidance in each and every step of my research work. I am grateful to you for guiding me patiently and assisting me during this course of my Ph.D work. His gentle and pleasing personality made the environment lively. Utmost thanks for your cooperation and help.

I would like to extend my vote of thanks to the Doctoral committee: Dr. Alka Upadhyay, Dr. Soumendu Jana, Dr. A. K. Lal for their constructive advice and useful comments. I am also thankful to former and present dean Prof. O. P. Pandey and Rafat Siddique, for providing fellowship as a teaching associate in time and

grants to attend the conference during my research period. I also wish to thank Dr. Kulvir Singh for his encouragement and consistent moral support. Also, I am grateful to all the faculty members and the staff of the SPMS for their kind help and support. My sincere thanks go to Dr. Bhaskar Chandra Mohanty and Dr. Dheeraj for helping me to curb the plagiarism. Working as a Ph.D student was a magnificent and challenging experience to me. During this period, many people directly or indirectly contribute in shaping up my academic carrier. At this juncture, I have many people to thank for their help and support. I am greatly thankful to my super seniors Dr. Gudveen, Dr. Kiran, Dr. Gurvinder Kaur, Dr. Rajni, Dr. Manjeet Singh Gautam, and Dr. Aman Deep Kaur for their gentle guidance and suggestion during my Ph. D work. I owe special thanks to my lab mates Dr. Neha Grover, Dr. Kanishka Sharma, Dr. Aman Deep Kaur, Gurjit and Shivani for their invaluable help, moral support and delightful company. Thank you for making my time here enjoyable. I would like to express my heartfelt thanks to my fellow lab mates Nitin and Vishal for their co-operation and encouragement. I deeply appreciate my friends Dr. Rameez Ahmad, Chhavi Pahwa and Piyush Sharma who supported me and inspired me during the odd phases of my life. This thesis would not have been possible without them. Thank you for your kind friendship and lifelong memories. I express my special thanks to my childhood friends Jatin Katna and Rachna Negi for being there when I need you the most. Thank you for helping me through all those tough times of my life.

Probably my words fall short to express my deepest gratitude to my parents (Mrs. Savita Sharma and Mr. R. K. Sharma) for guiding me to reach new heights of my life. Thank you muma papa for bestowing love on me, for making me inspired and filling my life with happiness, peace and love. Thank you, for being a patience-listener, for giving me correct advice and sorting out my problems easily. I can never ever repay what you did for me. I dedicate this work to you for your sacrifice and love. I am also thankful to my brother Akshat Sharma and my sister in law Subhashini Sharma for their consistent support and endless love. Special thanks go

to my entire family and grandparents for their numerous blessings.

Last but not the least, I owe my special thanks to my husband Mr. Kapil Kant for his immense support, patience, co-operation and belief in me. His positive attitude and continuous encouragement helped me to reach my goals. Thankyou for being there with me without being judgemental whenever i need a mentor, friend or family. Also i am grateful to my mother in law (Mrs. Kanta Sharma) and father in law (Mr. Bimal Sharma) for their caring and understanding attitude towards me during the submission of my thesis. I am heartily thankful to you 'muma-papa'.

I gratefully acknowledge the funding source UGC-DAE CSR, Kolkata, that made my Ph.D work possible.

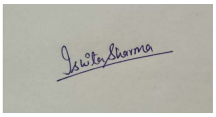

Patiala

Date 11/11/2020 (Ishita Sharma)

List of Publications

I. International Journals:

1. Relevance of Skyrme forces in the decay dynamics of $^{28}Si^{*}$ at stellar energies,
   Ishita Sharma, and Manoj K. Sharma, Nucl. Phys. A **994**, 121666 (2020).

2. Emission of light charged particles and fission fragments from Hf^{*} and Pt^{*} nuclei,
   Ishita Sharma and Manoj K. Sharma, Nucl. Phys. A **986**, 116-132 (2019).

3. Fragmentation analysis of $^{105}Ag^{*}$ nucleus governed via complete and incomplete fusion channels at $E_{c.m.}$=89 MeV,
   Ishita Sharma, and Manoj K. Sharma, (Accepted in Mod. Phys. Lett. A).

4. Fusion dynamics of compound nuclei with A_{CN} =166-202 investigated using different projectiles on ^{154}Sm target,
   Ishita Sharma, Raj. Kumar and Manoj K. Sharma, Braz. J. Phys. **50**, 64-70 (2020).

5. Investigation of the dynamics of $^{40,48}Ca$-induced reaction using different Skyrme forces,
   Ishita Sharma, Raj. Kumar and Manoj K. Sharma, Nucl. Phys. A **983**, 276-292 (2019).

6. Fusion dynamics of $^{30}Si+^{238}U$ reaction using variety of interaction potentials,
   Ishita Sharma, Manjeet S. Gautam and Manoj K. Sharma, Int. J. Mod. Phys. E **26**, 1750077 (2017).

7. Performance of Skyrme interactions on fusion dynamics of ^{6}Li induced reactions across the Coulomb barrier,

Ishita Sharma, Raj. Kumar and Manoj K. Sharma, Eur. Phys. J. A **53**, 140 (2017).

8. Probing the effect of neutron excess on the dynamics of Hf* compound system, **Ishita Sharma**, Raj. Kumar and Manoj K. Sharma, AIP publication **1953**, 140100 (2018).

9. Complete and incomplete fusion cross-sections for ^{7}Li+^{119}Sn reaction across the Coulomb barrier
Ishita Sharma, Neha Grover and Manoj K. Sharma, (under review, Indian J. Pure Appl. Phys.)

10. Dynamics of Se compound nucleus within the Skyrme energy density approach, Rajni, Deepika Jain, **Ishita Sharma** and Manoj. K. Sharma, Eur. Phys. J. A **53**, 208 (2017) [Not part of this thesis].

11. Analysis of dynamical behavior associated with ^{118,120,122}Xe isotopes,
Neha Grover, **Ishita Sharma**, Gurvinder Kaur and Manoj K. Sharma, Nucl. Phys. A **959**, 10-26 (2017) [Not part of this thesis].

II. In International/National Conferences, Symposiums and Workshops:

1. Probing the role of surface diffuseness and central radius on density distribution and barrier characteristics,
Ishita Sharma, Anu Nagpal, and Manoj K. Sharma, DAE-BRNS Symp. on Nucl. Phys., Vol. **64**, 412 (2019).

2. Complete and incomplete fusion cross-sections for ^{7}Li+^{119}Sn reaction across the Coulomb barrier,

Ishita Sharma, Neha Gover, and Manoj K. Sharma, International Conference on New Frontiers in Nuclear Physics, Banaras **58**, 440 (2013).

3. Dynamics of compound nuclei with A_{CN} 166-202 investigated using different projectiles on ^{154}Sm target,
   Ishita Sharma, Raj Kumar, and Manoj K. Sharma, International Conference on Hyperfine Interactions and their Applications, (2019).

4. Decay analysis of ^{12}C+^{16}O reaction using the generalized GSkI Skyrme interaction at stellar energies,
   Ishita Sharma, Raj Kumar, and Manoj K. Sharma, DAE-BRNS Symp. on Nucl. Phys. BARC(Mumbai), **63**, 604 (2018).

5. Probing the effect of neutron excess on the dynamics of Hf compound system,
   Ishita Sharma, Raj Kumar, and Manoj K. Sharma, 2^{nd} International Conference on Condensed Matter and Applied Physics, (2017).

6. Effect of incident channel properties on the fusion dynamics,
   Ishita Sharma, Raj Kumar, and Manoj K. Sharma, the DAE-BRNS Symp. on Nucl. Phys. **62**, 602 (2017).

7. Comparative analysis of Skyrme interactions in the decay of ^{136}Nd nucleus,
   Ishita Sharma, Raj Kumar, and Manoj K. Sharma, DAE Symp. on Nucl. Phys. **61**, 470 (2016).

8. Role of different Skyrme forces in the fusion of ^{48}Ti+^{58}Fe reaction,
   Ishita Sharma, Raj Kumar, and Manoj K. Sharma, 20th Punjab Science Congress (2016).

9. Role of spin orbit potential in two nucleon transfer reactions,
   Rajni, **Ishita Sharma**, and Manoj K. Sharma, DAE Symp. on Nucl. Phys. **60**,332 (2015).

Contents

List of Tables

List of Figures

Abstract

In the present thesis, an extensive study of heavy ion induced reactions is carried out in reference to fusion and subsequent decay processes. The analysis is done at energies across the Coulomb barrier and related anomalies are addressed adequately. Different methodologies are used to estimate the reaction dynamics. For the fusion process, Wong and ℓ-summed Wong model are applied, whereas, for the decay process dynamical cluster-decay model is used. In both the processes, nuclear interaction potential plays the eminent role, which is obtained either by Skyrme energy density formalism or via proximity theorem based proximity potential. Hence, the role of different nuclear interactions along with deformations, orientations, angular momentum, incident energies, N/Z effect are examined in the framework of Wong/ℓ-summed Wong and DCM model. The thesis is organized in eight chapters, the brief account of which is discussed below.

Chapter 1 represents the general introduction of nuclear reactions, their applications, extension of stable to exotic projectile beams, and various nuclear models used to assess the theoretical studies. Further, the low energy nuclear reactions comprising of compound nucleus formation and subsequent decay are emphasized in particular. The formation process is subdivided in two energy regimes i.e sub barrier and above barrier, the relevance of each regime is discussed in the chapter. Since, the sub barrier regime is sensitive to the structural effects and ion-ion potential, therefore, the influence of such effects and subsequent relevance in the reaction dynamics is discussed in detail. Besides this, various decay modes of excited compound nucleus are explored and discussed in this chapter.

The **Chapter 2** provides the broad description of methodologies used to address the fusion and decay mechanism of the heavy ion induced reactions. Firstly, the details of Wong formula and ℓ-summed Wong model used to examine the fusion process are discussed. Next, the total interaction potential is described which is used

as an important input in the formation and decay processes. The brief information of each contributing potential is given in the chapter. Particularly, the nuclear part of total interaction potential determined via energy density formalism is discussed in detail. In order to account the decay process, the dynamical cluster-decay model is used. The inclusion and the significance of various degrees of freedom such as separation distance R, deformations, orientation etc. and the model parameter known as neck length parameter is described concisely. Further, the description of preformation probability and the penetration probability used to address the decay dynamics and the cross sectional yield is also outlined.

In **Chapter 3**, the fusion dynamics of $^{30}Si + ^{238}U$ reaction has been studied using Wong and ℓ-summed Wong model. At sub barrier energies, the anomalously large hindrance in the fusion cross-sections signifies the importance of barrier modification effects for the adequate addressal of experimental data. Hence, the role of different Skyrme forces such as SIII, KDE0v1, SkT1, SSk, GSkI is examined to address the observed fusion hindrance around the Coulomb barrier. Among these, GSkI and SSk forces have quite similar behavior and thus are found to be more appropriate for complete addressal of fusion dynamics of chosen reaction. Within the Wong formalism, the effect of deformations and optimum orientations is duly incorporated and hence gives better description to observed data. Further, the fusion cross sections are predicted over extreme energies using SSk and GSkI forces within the ℓ-summed Wong approach. Besides this, the effect of mass, energy, and orientation of the colliding nuclei are analyzed in reference to the dynamics of heavy-ion induced ^{12}C+^{154}Sm, ^{16}O+^{154}Sm, ^{28}Si+^{154}Sm, and ^{48}Ca+^{154}Sm reactions undertaken across the Coulomb barrier. Here, different forms of nuclear potentials such as GSkI, SIII Skyrme force and the proximity potential mod Prox 88 are employed. The impact of different projectile target combinations on the corresponding barrier profile of interaction potentials is also examined.

In **Chapter 4**, the role of different Skyrme forces and associated neutron transfer effect is investigated in the view of $^{40,48}Ca + ^{96}Zr$ reactions. The fusion cross-sections

have been calculated using Wong formula and extended Wong model, wherein neutron transfer effect is studied by scaling the penetration probability of contributing channel(s). The decay analysis is carried out in the framework of dynamical cluster-decay model, where the neck length parameter ΔR and corresponding barrier modification ΔV_B are used to explore the neutron transfer effect in the decaying fragments. For fusion and subsequent decay, the nuclear potential is calculated using Skyrme interactions such as SIII, GSkI, SkT1, SkT2, and SkT3. In $^{40}Ca + ^{96}Zr$ case, the fusion hindrance is observed at sub barrier energies for the use of SIII, SkT1, SkT2 Skyrme forces. The cross sections are improved to some extent for GSkI force. Further, the inclusion of 1n-transfer channel in the calculations shows that the experimental data is adequately addressed for GSkI force, however, the correction of 1n-transfer channel for SkT1(or SIII, SkT2 forces) persists with the poor fit to experimental data. In the decay analysis, the interaction potentials significantly affect the structural properties of decaying fragments as clear from the behavior of fragmentation potential and preformation probability. Both, the fusion and decay analysis consistently advocate that GSkI force comprising of extended density-dependent term is able to address the sub barrier anomalies.

In **Chapter 5**, the decay of lighter compound system ^{28}Si* formed by ^{12}C+^{16}O reaction is analyzed at stellar energies span $E_{c.m.}$ = 4-5 MeV. The conventional SIII Skyrme force is used in conjunction with generalized GSkI and extended eMSL07 Skyrme forces having extended density-dependent terms, that can be potentially useful for the study of finite nuclei and the neutron stars. The DCM model is used to examine the emission of n, p, and α particles in the decay of ^{28}Si* nucleus along with other competing decay channels. The theoretical analysis advocates the emergence of ^{6}Li, ^{10}B, and ^{14}N fragments in the decay of ^{28}Si* nucleus, independent of the choice of Skyrme interactions and the angular momentum effects. The fragile nature of ^{6}Li nucleus may not allow it to survive the stellar conditions, and hence the breakup and /or radiative capture processes may appear in. The breakup of

^6Li is addressed in terms of Kinetic energy (K.E) value of A=6 fragment while the possibility of capture reaction is predicted in terms of positive Q values of radiative capture reactions ^{6}Li(n,γ)^{7}Li, ^{6}Li(p,γ)^{7}Be, and ^{6}Li(α,γ)^{10}B. It has been observed that the structure of fragmentation potential and preformation probability is independent of the choice of Skyrme forces, but their magnitude gets significantly influenced for the use of different Skyrme forces. The conventional SIII force could not reproduce the cross sections while eMSL07 and GSkI Skyrme forces give nice agreement with the experimental data.

In **Chapter 6**, the performance of selected five Skyrme forces (out of a set of 240), tested by Dutra *et al.*, is analyzed in view of fusion-fission dynamics. These forces are assumed to perform better for neutron rich systems, so the choice of reaction is accordingly made by opting for neutron rich target i.e. $^6Li + ^{238}U$ reaction. This reaction is diagnosed further in reference of fusion hindrance within the decay dynamics explored via cluster-decay model. In order to reduce computational time, three Skyrme forces are figured out with the criteria such that these forces cover the barrier characteristics of remaining two forces as well. The fission cross sections are successfully addressed at low energies for ^{6}Li+^{238}U reaction. However, at relatively higher energies, the excitation functions show theoretical suppression with respect to experimental data, which may be associated with possible presence of incomplete fusion (ICF). For ICF, we have considered that the ^{6}Li breaks into ^{4}He+^{2}H, as mentioned in experimental work. The calculations of ICF are carried out for ^{4}He+^{238}U reaction with the selected Skyrme forces at $E_{c.m.}$ = 26.20 and 27.51 MeV. These forces address the data nicely for compound nucleus (CN) as well as ICF processes. Here, the NRAPR force seems to require lesser barrier modification as compare to the other forces, therefore it can be used as an alternate choice for calculating the interaction potential. Additionally, the prediction of fission cross sections at lower energies has been done with DCM using NRAPR force. The ℓ dependent % barrier modification of the Skyrme forces undertaken is also worked out in reference to

fusion hindrance at below barrier energies.

In **Chapter 7**, the decay analysis is carried out for isotopes and isobars of ^{170,174}Hf* and ^{170,174}Pt* nuclei using the DCM model. The structural information from the excited Hf* and Pt* nuclei is extracted using the fragmentation potential and preformation probability, which in turn accordingly influence the cross section yields. The cross sections of evaporation residue and fission-fragments are calculated by optimizing the neck length ΔR with in the frame work of DCM model. The neck length ΔR provides useful information about the shape elongation of decaying fragments and in turn provides an insight of the reaction time scale. Applying the momentum conservation, the velocity and time scale of fission fragments is calculated for ^{170}Hf* nucleus, which comes out of the order of (0.7-1)$\times 10^{-21}$s and the same for light charged particle is 0.5×10^{-21}s.

Finally **Chapter 8** summarizes the results and conclusions attained in the above discussed chapters. For the extension of this work, a brief note on future scope is also given at the end.

Chapter 1

Introduction

Nuclear reactions occur in the earth's crust since the beginning of the universe, but the science of atomic radiations, radioactivity, nuclear structure, fusion-fission etc was developed about a century ago. After the discovery of nuclear fission in 1938, it had made a revolutionary impact on nuclear reaction dynamics and consequently caused significant modifications regarding understanding of nuclear behavior. For many years, the nuclear technology has faced society's disbelief due to possible creation of nuclear weapons and perceived problems in handling nuclear waste disposal. Since the beginning of 21^{st} century, the field of nuclear physics got evolved with numerous developments in the area of experimental and theoretical field, covering all aspects of subatomic physics, astrophysics, and range of applications in energy, national security, and biomedical etc. In nuclear physics particularly, the nuclear reactions provide a unified description and understanding of the nuclear structure, reaction mechanism, distribution of nuclear matter, effective interactions between nucleon, and so on. Since long ago, the nuclear reactions are being synthesized by striking stable beams on variety of target nuclei, which covers a chunk of those elements that are thought to exist on earth. However, various mechanisms relevant to synthesize the elements in the stellar process are being understood. Extending the study further, the discovery of exotic nuclei formed via short-lived radioactive isotopes opens new opportunities to expand the scope of nuclear reaction dynamics.

Globally, the interest disseminated evolution in the experimental field, and eventually advanced accelerator facilities were developed to produce radioactive beams at different energies. The accessibility of radioactive beam augments the understanding of exotic nuclear phenomena such as shell evolution, switching of magic numbers, neutron or proton halo nuclei, clustering effect, etc. Nowadays, the study of unstable exotic nuclei has become the forefront of research because it not only reveals new physics but also leads to the new insight of the nucleosynthesis processes [1].

Basically, the exotic nuclei are the extremely neutron/proton rich nuclei in which one or more nucleons exist in the unbound state(s). These unbounded nuclei disintegrate in about 10^{-21}s and hence possess very small lifetime. The interesting fact about these nuclei is that their characteristics features are significantly different from that of normal nuclei that lie in the valley of stability. The study and production of these unstable nuclei is relatively difficult because of their (i) low cross sections and (ii) very short half lives [2–5]. However consistent technological developments have made it possible to produce a whole series of exotic nuclei so as to study the properties of these nuclei. At present, the exotic nuclei are being studied in the laboratories such as GSI, GANIL, RIKEN, CERN, JINR, NSCL and ORNL using the accelerator facility: ISOL (isotope separation on line) and in-flight [6–8]. The weakly bound nature (^{6,7}Li, ^{9}Be, etc) and large spatial extension of halo nuclei (^{6,8}He, ^{11}Li, ^{11}Be, etc) are the two important characteristic features of exotic nuclei [9–11]. These nuclei being unstable and rare, could not be used as target nucleus and are being taken up as exotic beams that are directed towards the stable target nuclei. The study of exotic beam together with stable nuclei takes the field of nuclear physics to the next level and guides the theoretical approaches either by confirming predictions or by uncovering the missing aspects of related physics. In the theoretical studies, different models and approaches have been used to interpret numerous physical phenomena. A brief description of some theoretical models is given in the following section.

1.1 Nuclear models

The nucleus is a complex quantum mechanical system consisting of a finite number of nucleons bounded together by strong interactions. Being a many-body system, it exhibits several specific properties such as collective rotation, pairing co-relation, interplay of single-particle and collective degrees of freedom etc. The interplay of single and collective particle behavior presents a great challenge to such nuclear models. First of all, the liquid drop model (LDM) [12] was developed that considered the nucleus as an incompressible drop of liquid and helped to explain certain processes/properties such as nuclear fission, binding energies of nuclei and became a precursor of the collective description of nuclear structure. It explained the properties of the nucleus as a whole but has said nothing regarding the properties of the nucleonic composition of nucleus. Such properties are explained by shell model [13] which is the complete microscopic model and considered that the nucleons are filled in the nuclear shells, paired off with mutually opposite spins by following the Pauli's exclusion principle. However, there were some flaws in the prediction of this model regarding the magnetic moment which further gave birth to the collective model. This model includes the facet of both the liquid drop model as well as the shell model to explain the properties of magnetic and electric moment that neither of them explains separately [14]. It considered the collective motion of nucleons in the core, combined with the motion of loosely bound surface nucleons which give rise to rotational and vibrational motion of the entire nucleus. It explains commonly measured properties of nuclei such as nuclear shapes, magnetic moment, angular momentum, excited state energies, etc. Further improvements were made and unified deformed shell model such as Nilsson model [15] and Projected Shell Model [16] was devised to address the properties of heavier deformed nuclei. The numerous efforts were made there after and many refined nuclear models were made available. Such robust and reliable models of nuclear structure in the theoretical physics allow the understanding of nuclear phenomena associated with many-body quantum systems.

The availability of reliable nuclear models enabled the theoreticians to make numerous validations and predictions at femto scale. Another additive factor that helps to build up the success of theoretical nuclear physics is the high-performance computing system. The amalgamation of theoretical methodologies and computational facilities helped the scientific community to make significant advancement in this field. The advanced computational facilities have helped to develop the theoretical as well as experimental expertise in the area of nuclear physics. The properties and structural aspects of nuclei can be better understood in terms of nuclear reaction dynamics. The nuclear reactions are classified into three energy categories such as low energy, intermediate energy and high energy, but the present thesis is concerned with the study of low energy nuclear reaction dynamics, the details of which are given below.

1.2 Low Energy Nuclear Reaction (LENR)

The LENR is the core component of the nuclear field which deals with the origin and the properties of atomic nuclei. The LENR are generally worked out at beam energy < 15 MeV/nucleon, in which two nuclei interact together and transform from one species to another. The analysis of nuclear reactions in this domain depends upon the combination of three features: reaction mechanism, internal structure of the colliding nuclei and the nucleonic interactions between them. The reaction amid the incident beam and the target occurs either via direct reactions [17] or by compound nucleus route [18]. A brief account of direct and compound nuclear reaction is given below.

1. Direct reaction: It is a single-step reaction that takes place at a short interval of time, of the order of 10^{-22}s and ocurs on the surface rather than the volume of the interacting nuclei. In this process, a single nucleon or the cluster of the nucleons from the projectile nucleus interact with one or two nucleon(s) of the target without exciting the rest of the nucleus. The elastic, inelastic and

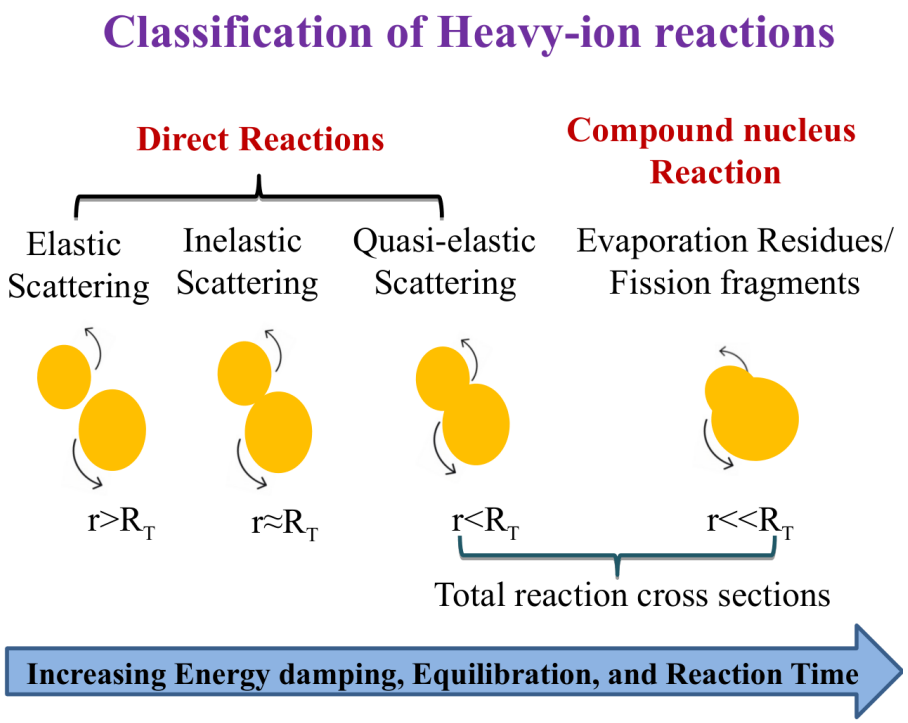

Figure 1.1: Schematic diagram of heavy ion collision processes distinguished on the basis of energy damping effect.

quasi elastic scattering are sub-categories of direct reactions [19]. In elastic and inelastic scattering, only the direction and kinetic energy of the projectile nucleus changes while the outgoing fragments are identical to the colliding partners. In the former case, energy of the target nucleus remains unchanged but for the latter case, the target nucleus is excited to higher energy and it de-excites via gamma emission. In the course of quasi elastic reaction, along with the exchange of energy, there is a transfer of mass between the projectile and target nucleus that brings the fundamental change in the transfer reaction in comparison to that of inelastic scattering. The present thesis is mainly focused on the compound nucleus reactions, the details of which are given below.

2. Compound nucleus reactions: In contrast to direct reactions, the compound nucleus process takes place at lower energies (due to energy damping) which is known to proceed via nucleon-nucleon interactions that lead to a fully equilibrated

intermediate system referred to as the compound nucleus. Since, the equilibration in energy, mass, angular momentum requires the time, therefore coalesce of the whole projectile nucleus with the target takes a relatively long time, of the order of 10^{-19}s. The pictorial presentation of direct and compound nucleus reactions is shown in Fig. 1.1. The process of evolution of the compound system is named as fusion process. To be more specific, fusion means the complete unification of the projectile-target nuclei in all degrees of freedom, that forms an equilibrated system in which momentum and energy of the incident beam are uniformly distributed amongst the nucleons of compound system. The enormous collisions between the nucleons cause the loss of information of the entrance channel. As a result, the decay of the compound system is in general independent of the way it was formed. This idea of memory loss between the entrance and exit channels was proposed by the Danish physicist Neil Bohr in 1936 [20]. The decay of compound nucleus is statistical in nature where single nucleon or small group of nucleons by statistical fluctuation accumulate sufficient energy and come out of the compound system. This thesis work deals with both fusion and decay analysis of compound nucleus. Firstly, the fusion process is discussed in detail and then the decay mechanism is explored in the subsequent section.

1.3 Fusion process

The fusion in heavy ion collision is an imperative process in many aspects. It contains rich physics at energies athwart the Coulomb barrier. On the basis of incident energy, it is broadly divided into two energy regime viz, the sub-barrier fusion and above barrier fusion. Interestingly, the mechanisms and associated properties in both the energy regime are quite different from each other. The sub-barrier fusion of lighter nuclei plays an imminent role in the evolution of massive stars while the fusion of heavier nuclei at the above barrier energies is considered as an essential route for the production of superheavy nuclei [21]. The relevant details are discussed below.

1.3.1 Sub barrier fusion

It is referred to the fusion of reacting nuclei at incident energy underneath the Coulomb barrier i.e. E<V_B, which is classically forbidden but occurs via quantum mechanical tunneling process. The outstanding feature of sub barrier fusion is the anomalous increase of fusion excitation function with respect to standard statistical model. It was first observed in the studies of Beckerman *et al.* [22] and Stokstad *et al.,* [23] in 1980. Soon the pioneering work of Beckerman *et al.* [24], Reisdorf *et al* [25], and Pengo *et al.* [26] added further information about the nature of variation in sub barrier cross-sections and global features of the phenomena were established. Several probes for the explanation of unexpected behavior have been made from the experimental and theoretical front. Later on, the interpretation of fusion enhancement was given in terms of neutron transfer effect, neck formation, static deformations and orientations, rotational and vibrational coupling and the nature of ion-ion potential. The brief of each terminology is given below.

(i)Neutron transfer effect: The neutron transfer effect shows remarkable influence in the sub barrier fusion process [27]. This is because the neutrons being neutral particles are insensitive towards the Coulomb field and their transfer takes place prior to the capture process. Further, the co-relation among the sub barrier cross-sections and the Q values of transferred neutron make this study even more interesting [28]. This is because the neutron transfer with positive Q value enhances the kinetic energy of the reaction that consequently increase the cross-sections at sub barrier energies, whereas, the channel with negative or zero Q value does not give rise to such effect. In view of this, the role of positive Q value neutron transfer (PQNT) in the fusion mechanism becomes the topic of great interest. Generally, the influence of the transfer channel is strong in some cases and weaker for other ones. Sargsyan *et al.* [29] suggests that with neutron transfer effect, the mass number and the deformations of colliding nuclei change significantly, which on the other hand, modify the barrier height and shape of the interaction potential and results in the

unexpected enhancement of the reaction cross-sections.

However, in some cases, the change in deformations is negligible, therefore the cross-sections seem to be weakly influenced by the transfer effect.

(ii)Neck formation: The neck formation between the two reacting nuclei is governed by the neutron transfer effect. One can say that neutron transfer effect and neck formation go hand in hand. Generally, the flow of neutrons develop the neck between the interacting nuclei and it is considered as a doorway state in the fusion process [30]. In other words, it induces the barrier lowering effect. Since, the separation distance with neck degree of freedom (R_N) is larger than the Coulomb barrier position (R_B), therefore, $V_N < V_B$, where V_N and V_B are the interaction potential at separation distance R_N and R_B respectively. As a result, it favors the sub barrier fusion process and enhances the fusion probability to a reasonable extent

(iii)Deformations and orientations: The sub barrier region is extremely sensitive to the nuclear shapes and the orientations of the interacting nuclei. No doubt, nuclear deformation plays an essential role in the overall reaction dynamics but it specifically imparts imperative effect on sub barrier fusion process. The above barrier fusion process ensues via classical mechanics, therefore, it does not require barrier adjustment for undergoing reaction mechanism. However, the tunneling process at deep barrier energies seeks for the barrier lowering effect. As the capture of the projectile at sub barrier energies is a slow process, therefore, the deformed nuclei may get enough time to orient themselves in order to lower the barrier height significantly. Hence, the deformation along with the orientation of the nuclei play vital role in addressing the fusion dynamics. A brief description of nuclear deformation and orientation is given below.

A very few nuclei have spherical shape in the ground state while most of the nuclei tend to deviate from the spherical configuration because their shells are partly filled. The valence nucleons outside the closed-shell induce a force on closed-shell that causes the polarization of the nucleus. Depending upon the strength of the polarization, a variety of nuclear shapes have been observed. The nuclei mainly

exhibit quadrupole(β_{2i}), octupole (β_{3i}) and hexadecapole (β_{4i}) deformations, where the quadrupole deformation is the most commonly observed and studied in the literature. On the basis of axial symmetry, the quadrupole deformation can be easily distinguished as a prolate (or elongated) shape having deformation parameter $\beta_{2i}>0$ and oblate (or flattened) shape with $\beta_{2i} < 0$. The deformation without axial symmetry resulting in elongation along the three axes of the system is referred to as the triaxial shape (or quadrupole deformation). Commonly, the prolate shape dominates over the oblate shape while the triaxial shape is rarest among them [31]. Further, on the basis of major to minor axis ratio, deformed nuclei fall in to different categories. When this ratio is 1.3 : 1, the nuclei are known to be normally deformed. For highly deformed nuclei, the ratio is around 1.5 : 1. If the ratio is 2:1, the nucleus is referred to as super deformed, while for relatively higher ratio i.e. 3:1 it is referred to as hyper deformed nucleus. The numerous experimental information confirms the importance of deformations in sub barrier fusion process as it has a straight forward impact on the interaction potential [32,33]. The sensitivity of fusion cross-section and fusion barrier is not limited to the quadrupole deformation only, but also the sign of hexadecupole deformation unambiguously affects the sub barrier fusion region in various heavy-ion reactions [32]. Apart from static deformations, the dynamic deformation (rotation and vibration mode) also manifests their effect on the reaction dynamics. Since, the collision of deformed nuclei can cause rotation or surface vibration of nuclei, which means they can go to rotational or vibrational excited states and coupling of these states with the intrinsic motion of nuclei shows a marvellous impact on the collision process.

Besides the shape, sign, and magnitude of the deformed nuclei, the nature of the nucleus alignment also influences the probability of compound nucleus formation via affecting the barrier height [34]. In comparison to the spherical case, it has been observed that the barrier is lower for elongated (noncompact) configuration having the largest interaction radius and it is higher for most compact configuration

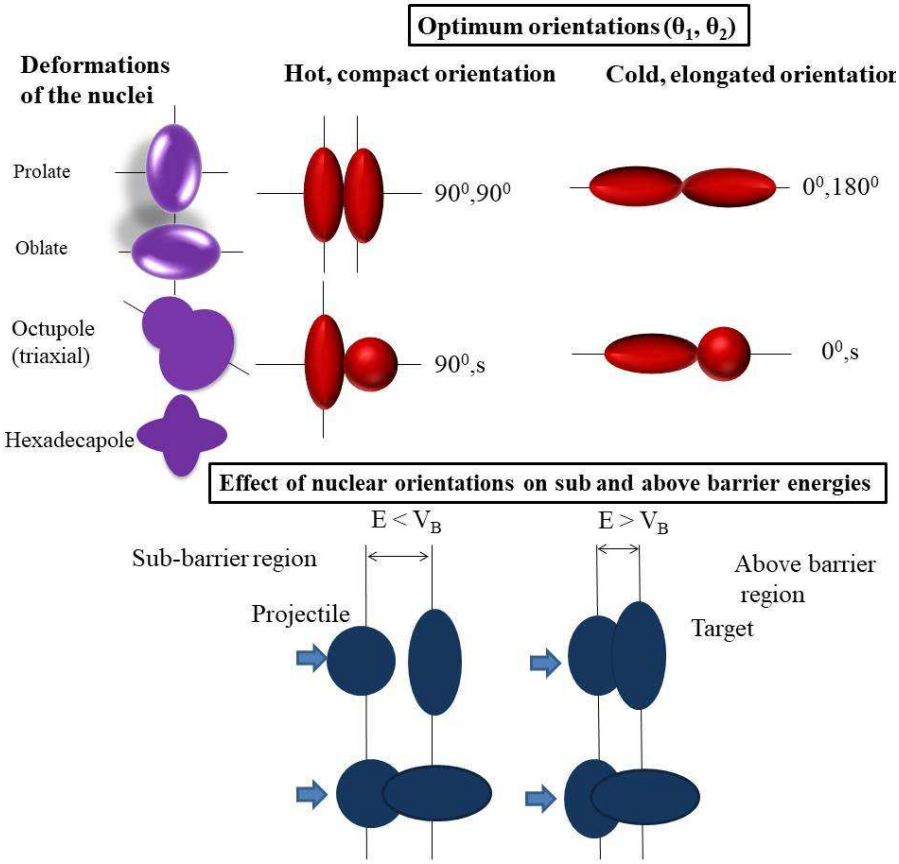

Figure 1.2: Shapes and orientations of the nuclei along with their relative effect on the sub barrier and above barrier energies.

having a smaller interaction radius. The fusion with elongated cold nuclear shape is refereed to as cold fusion and the most compact hot nuclear shape corresponds to hot fusion. These two criteria of deformed nuclei define the optimum orientations of the nuclei which play a vital role in addressing the anomaly of sub barrier region and helps to explain the synthesis of super-heavy element. It is to be noticed that only the signs of quadrupole moment alone decide the optimum orientations of the interacting nuclei, hence passive to the nature of hexadecupole deformation [34]. The pictorial representation of nuclear deformation, orientations and their impact around the Coulomb barrier energies is shown in Fig. 1.2. For the fusion process, the above barrier region is equally important like the sub barrier region because it

adds useful information regarding overall understanding of reaction dynamics. The detailed information of above barrier region is discussed in next section while the influence of ion-ion potential on the fusion process will be discussed in the subsequent section.

1.3.2 Above barrier fusion

At above barrier energies, the reaction mechanism is seen to be significantly modified. The compound nucleus formation tends to preclude and evolve into the Di-Nuclear System (DNS) that doesn't reach the complete equilibration in all degrees of freedom such as mass, charge, energy, angular momentum and spin. More specifically, two main competing reaction mechanisms exist at higher energies, one corresponds to Complete Fusion (CF) process that saturates at higher energy and the other one corresponds to the DNS which increases consistently with the increase in the incident energy. If only the complete fusion process exits at higher energies, the total excitation function is referred to as fusion cross-section whereas if there is the contribution from CF as well as DNS, the total excitation functions are referred as capture cross-sections. During the collision, the dynamics is greatly influenced by the nucleon-nucleon interactions. If the Coulomb and centrifugal potentials are sufficiently small, the two nuclei fuse inside the attractive potential well, equilibrate in all degrees of freedom and form the compound system. If the Coulomb and centrifugal fields are significantly large, no attractive potential pocket is formed. The interacting nuclei lose some part of their kinetic energy to overcome the barrier, as a result, they interact for a short while and separate apart. This gives rise to deep inelastic process which takes place typically in the energy around E=10 MeV/n. The study of deep inelastic collision started in the late 1970s that simulates the development of dissipative theories in nuclear dynamics [35]. Later on, the phenomenon of quasi fission was discovered in 1980 [35], which arises when the reactants get trapped in the attractive potential well after surmounting the Coulomb barrier and reseparate before achieving the equilibration in shape and mass degree of freedom.

A relatively large dissipation of kinetic energy takes place in this process. Interestingly, the dinuclear system is formed in both the processes, but in the later case, it lives for a sufficiently long time while it is short-lived in case of Deep Inelastic Collision (DIC). Experimentally, these processes are distinguished on the basis of kinetic energy, mass, charge, and angular momentum distribution. Generally, DIC takes place when lighter nuclei collides at higher energies and angular momentum ℓ values. For heavy-ion collision of massive nuclei, quasi fission is the dominant process that is known for hindrance in the way of CN formation [36]. The complexities in the fusion dynamics evolved when another competing process like fast fission contributes at higher incident energies. The process occurs when the angular momentum dependent fusion barrier gets vanished out. In analogy to quasi fission, full relaxation of kinetic energy and considerable mass transfer between the two nuclei takes place in the fast fission, but the only difference between quasi fission and fast fission lies in the values of angular momentum and excitation energy. The fast fission takes place only at higher values of ℓ whereas quasi fission occurs at relatively lower values of orbital angular momentum. Also at moderate excitation energies, fast fission is negligible.

Depending upon the nature of incoming channels, the above barrier region also encounters the incomplete fusion process, which is a strong competitor to CF in case of loosely bound and halo projectiles. In recent years, the fusion of loosely bound nuclei (both stable and radioactive) are intensively studied from the experimental and theoretical front [10, 37–40] Owing to low separation energy/binding energy, the weakly bound projectile breaks prior to the fusion with target nucleus. As a result, either of the breakup fragment interacts with the target nucleus while the remaining fragment moves in the forward direction as a spectator. Numerous studies on the reactions involving weakly bound and halo nuclei with heavy targets state that complete fusion is suppressed at above energies by about 30 percent. This suppression attributes to the incomplete fusion process whereas the total fusion process does not seem to be influenced by the breakup effect. For light mass targets,

the suppression in complete fusion is not clearly observed because for this case, the incomplete fusion is not as prominent as in the case of heavier targets. It apparently indicates that this reaction process is dominated in loosely bound projectile case having large mass asymmetry reaction channels.

The fusion dynamics is basically assessed by heavy-ion interaction potentials. Hence, the knowledge of nuclear potential is essential for understanding the nuclear formation and subsequent decay mechanisms.

1.4 Ion-Ion potential

The sub barrier fusion is attributed to the probability of quantum mechanical tunneling through the interaction potential, which is quantitatively understood in terms of the interplay between the repulsive Coulomb potential, angular momentum dependent centrifugal potential and attractive nuclear potential. The relative contribution of these potentials arises from masses and charges of the interacting nuclei, which finally forms a typical total interaction potential whose maxima at large separation distance is termed as fusion barrier and the deep minima at a small distance is referred to the potential pocket, which serves as a trap for the colliding nuclei to undergo a fusion process. The barrier at $\ell = 0$ and temperature T = 0 MeV is known as Coulomb barrier V_B with barrier position R_B. Basically, the barrier height is characterized by Coulomb repulsion V_C and ℓ dependent centrifugal potential V_ℓ, where the increase in the ℓ values serves to vanish the potential pocket which is actually assessed by the attractive nuclear potential. Over the last few decades, the analysis of nuclear potential has become one of the utmost challenging topics in low energy nuclear physics. Various models and methods have been developed to provide a plausible description of nucleon-nucleon potential between the nuclei. The most fundamental and traditional is 'ab initio' method which was started with the basic microscopic interactions between the nucleons and predicts the properties of finite nuclei. However, some advancements are required in this method which were

further added by implicating the techniques of many body theory such as Brueckner Hartree Fock, correlated basis function, expansion of no-core shell model (NCSM), etc. These techniques help to reproduce some properties of nuclei but precision in describing the properties still needs improvement [41]. Besides this, the phenomenological macroscopic analysis inspired by liquid drop model or refined droplet model was used. This model describes the average trend of binding energies but the actual nuclei seem to deviate from the average behavior and thus for better agreement, the shell corrections are included. This combined theory of macro-microscopic approach tuned to the higher predictive power of ground state properties but leaves some uncertainties when one moves from normal to exotic nuclei. Between the 'ab initio' and mic-mac theory, there lies two different models that work at the microscopic level but apply effective density functions [42]. One is the shell-model calculations in which effective interactions are taken from microscopic G matrix and the other is the self-consistent mean-field theory that relies on the unprejudiced, self-consistent estimation of nuclear mean-field, which is closely related to energy density functional theory [43]. The self-consistent Hartree Fock calculations have made considerable progress over the last decades but the discovery of phenomenological effective interactions namely Skyrme forces by Vautherin and Vanouce (1969) [44], Vautherin and Brink (1973) [45], introduction of Gogny force (1973) [46] and formulation of the relativistic mean-field by Walecka [47] form three standard models in mean-field theory which is widely used today and competes with other theories. Among these effective forces, the most simple and widely used interaction is the Skyrme-type effective nucleon-nucleon interaction proposed by T.H.R Skyrme in 1959 [48] and revived by Vautherin and Brink in 1973 [45].

Skyrme Interactions

The simple structure of Skyrme interaction allows to express the energy functional in terms of Hamiltonian density, which itself is expressed in terms of nucleon density

ρ, kinetic energy density τ and spin-orbit density $\vec{J}$ [45,46,48,49]. These interactions simplify the calculations with its zero range term and have been successfully used to describe the ground state properties of spherical and deformed nuclei. However, the excessive computational time for Hartree Fock calculations provides strong motivation to adopt semi-classical approach in which the local densities i.e. kinetic energy density and spin-orbit density are determined using so-called Extended Thomas Fermi model [50–54]. The Skyrme interactions contain various density-dependent terms, where each term has its fundamental role in describing the effective properties of nuclei and the fusion barrier. The standard form of Skyrme interactions consists of term ρ^2 which describes the two body attractive interaction which is counterbalanced by density dependent repulsive $\rho^{2+\alpha}$ term. The kinetic energy $\rho\tau$ term provides the effective mass of the nucleon while the surface term $\rho\nabla\tau$ is crucial to tune the correct trend of energy in finite nuclei. The spin-orbit term $\rho\nabla$J is indispensable to reproduce the correct sequence of single nucleon orbit [55]. With these terms, the different parameters have been associated that help to determine the saturation density ρ=0.16 fm^{-3}, Energy per nucleon E/A = -16 MeV of the finite nuclei [56]. Once these properties are determined, the values of incompressibility (K) and effective mass (m*) are deduced by α, as the relation of ρ^α is strongly associated with incompressibility and effective mass of the nuclear system [57–60]. Though all the terms in Skyrme Hamiltonian are the function of nucleon density ρ but the pure density dependent function is known for its crucial importance. In order to extend the study from finite nuclei to dense nuclear matter, the single density-dependent term does not seem to be sufficient, hence, the higher-order density-dependent terms are added [61]. Initially, the conventional Skyrme forces namely SI, SII, SIII were developed by Vautherin and Brink [45] which contain only single density-dependent term. With time, modifications and generalization of Skyrme forces were done by various authors Krewald *et al.* [62], Kohler *et al.* [63], Brack *et al.* [50], Giani *et al.* [64] who have introduced GS1-GS6, SKa-Skb, SKM, SKM* [50]. Recently, Agar-

wal *et al.* [58,65], Zhang *et al.* [66] have made substantial modifications in the Skyrme forces and proposed the generalized Skyrme forces that are suitable for the study of finite, iso-spin rich nuclei as well as the neutron stars. Depending on various microscopic properties such as m^*, K_0, ρ_0 etc, the Skyrme parameters α, x_0-x_3, t_0-t_3 are derived [56] and thus different Skyrme forces with different parameterizations are formed. Further, the ability and performance of 240 Skyrme interactions comprising of standardized and generalized set have been evaluated by Dutra *et al.* [67] which has shown that 16 out of 240 interactions satisfy the constraints applied on them [67]. In the present work, the behavior of the SKRA, NRAPR, LNS, KDE0v1, and SQMC700 Skyrme forces along with the GSkI, SSk, SkT1(T2, T3) forces are investigated across the Coulomb barrier for the interacting nuclei varying from normal to iso-spin rich cases. It is important to mention that nuclear potential in terms of Skyrme interactions can be obtained using sudden and frozen density approximation. Since the frozen density approximation gives more realistic results over the sudden approximations therefore, the calculations are performed with frozen density approximation [68]. Besides the Skyrme interactions, optical model based semi-microscopic folding potential is also available in the literature, but the present study is concerned with effective Skyrme interactions and the macroscopic approach based phenomenological potentials. The flow chart of nuclear potentials is presented in Fig. 1.3 and the detail of analytical/phenomenological method is discussed in the following section.

Phenomenological potentials

With time, the tedious job of two-and three-body interactions shifted the interest towards another group of models that take the entire macroscopic picture of the nuclei into account. Among the various types of analytical potentials such as Woods Saxon, Yukawa, bass potential, etc the proximity type potentials enjoy the special status and became the benchmark and backbone for many micro/macroscopic fusion

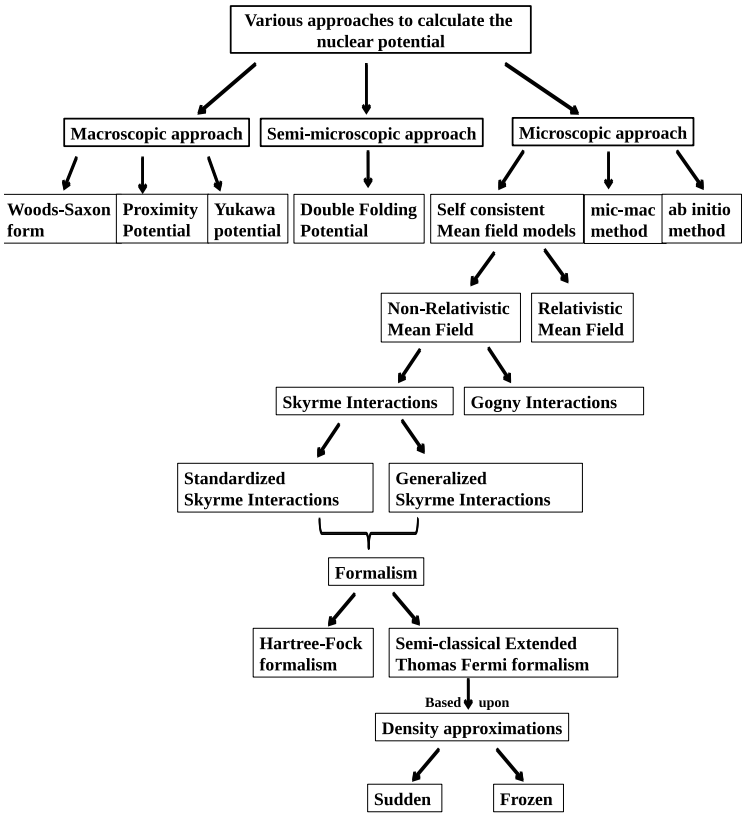

Figure 1.3: Flow chart of various methods used to determine the nuclear interaction potential.

models. The concept of phenomenological proximity potential was first proposed by Blocki *et al.* in 1970 [69]. Based on the proximity theorem, it is composed of two factors: one depends upon the shape and geometry of the colliding nuclei and second is the universal function which is independent of the shape and geometry and depends upon the separation distance s_0. The s_0 and mean curvature radius R encloses the shape and orientation effects. The systematic study on heavy-ion fusion reactions urges the refinement and modifications in the original proximity potential and thus potential is remodelled and parameterized with proximity concept and thus various proximity type potentials have been made available in the literature [70]. The behavior of such potentials in context of fusion barrier and cross-section yield

has been extensively studied in diverse reactions varying from the lighter to heavy mass region [71–73]. In the present thesis, the proximity 77 along with the energy density formalism based Skyrme interactions are used to address various reaction mechanisms around the Coulomb barrier. The sub barrier region provides worthy information about the interaction potentials and becomes a topic of prolonged interest that aims at testing the various theoretical models with the available data. This region is known for the complete fusion process and the fusion cross-sections are addressed using the Wong formula [74] and ℓ-summed extended Wong model [75]. The original Wong formula works well at energies nearby the Coulomb barrier, however, it fails to imitate the experimental data at energies higher and beneath the Coulomb barrier. To address the anomaly, the assumptions made in the Wong model are refined and extended Wong model was introduced [75].

The fusion of heavy-ions across the Coulomb barrier provides relative knowledge of the reaction mechanism, but experimentally the information is inferred from the decay process. With this proviso in mind, the decay of hot and excited compound nucleus being equally important, is discussed in the next section.

1.5 Decay of the excited compound nucleus

The compound nucleus (CN) formed via heavy ion induced collision is usually unstable in nature as it is formed in excited state having sufficiently large angular momentum, which eventually de-excites via various decay processes. Depending upon the energy and mass, the CN formed in low energy heavy ion collisions in general decays either via evaporation residue (ER) [76] or via fusion-fission (ff) mode [77].

Evaporation Residue: In evaporation, the neutrons, protons and alpha particles are statistically emitted along with complementary residual nucleus having mass slightly less than CN. In heavy-ion reactions, when the mass of compound nucleus $A_{CN} < 100$, the decay of compound nucleus takes place primarily via evaporation residue with very low probability of fissioning. In this case, the neutron emission

is the favorable decay mode at all the excitation energies because it experiences no Coulomb field. However, the charged particles such as proton and alpha particles start emerging at higher kinetic energy. Similarly, in the case of loosely bound or lighter mass A<20 projectile nuclei, the CN formed via incomplete fusion process also decays via emission of evaporation residues [78, 79]. The distinction between the ER emitted from CN formed by complete and incomplete fusion process is a difficult task in case of lighter systems [80]. When the heavier target is used, the probability of neutron emission over the charged particles is relatively higher and thus guarantees the discrimination between the processes on the basis of charge number identification. In the lighter mass region, the total fusion cross-sections are mainely populated via ER channel with some minor contribution of intermediate mass fragments (IMF) having mass range $5 \leq A \leq 20$.

Fission: For medium and heavy mass compound systems, fission starts competing with ER, therefore, the total fusion cross-sections are expressed as sum of ER and fission. In some cases, Intermediate-Mass Fragments (IMF), the Heavy-Mass Fragments (HMF) also contributes along with ER and ff and define the total fusion cross section as the sum of ER, IMF, HMF and ff. However, in the trans-lead or actinide region, fission is the predominate mode of decay and the cross-sections are obtained using the fission yield only. The fissioning of nuclei was first discovered by Hahn and Strassmann in 1939 [81], which considered it as a macroscopic phenomenon that evolves due to the collective motion of the whole nucleus. The liquid drop model is used to address the gross features of fission but it could not account the other properties such as asymmetric fission, fission isomer etc and thus it seeks for the inclusion of microscopic properties such as binding energies, shell effects, deformations, and level density parameter to interpret the fissioning of compound nucleus [82, 83]. Bulk of studies cover the fission cross-sections, fission-product mass distribution, nuclear-charge distribution, kinetic energy distribution, etc to have overall idea of the decay dynamics. To address the experimental findings, various

theories have been developed that drive the relevant information of mass distribution from potential energy surface using the microscopic-macroscopic or self-consistence microscopic approaches [84]. The mass distribution of fission fragments can be reproduced by using the theoretical models which in turn manifests that shell effects and pairing co-relation play vital role in the reaction process and help to explain the gradual transition from symmetric to asymmetric mass distribution with increasing mass, especially in the actinide region [84]. Also experimentally and theoretically, it was noticed that the probability of fission increases with an increase in the angular momentum. This is because the fission barrier disappears at the large value of angular momentum. After a certain ℓ value ($\ell > \ell_{crit.}$), it is impossible for the compound system to accumulate such higher ℓ values and retain it's memory loss. Henceforth, rather than a real compound system, di-nuclear system is formed that makes it difficult to disentangle the fission process from other competing processes especially the damping process that leads to fission without undergoing the CN formation. The total kinetic energy, mass, and angular distribution of damping processes such as deep inelastic collision, quasi fission and fast fission may overlap, and cause difficulties in addressing the mechanisms that produce the corresponding reaction products [85–89]. Pictorial description of various reaction processes is shown in Fig. 1.4. In the present thesis, the decay dynamics of excited compound system is analyzed using the Dynamical Cluster decay Model (DCM) [90–94] which is based upon Quantum Mechanical Fragmentation Theory [95]. The advantage of DCM model over various theoretical models is that it can be used to address various reaction processes prevailing in heavy-ion induced reactions at below as well as above the Coulomb barrier energies. Using the same approach, the role of different nuclear potentials is explored in view of various decay processes evolved in heavy ion induced reactions.

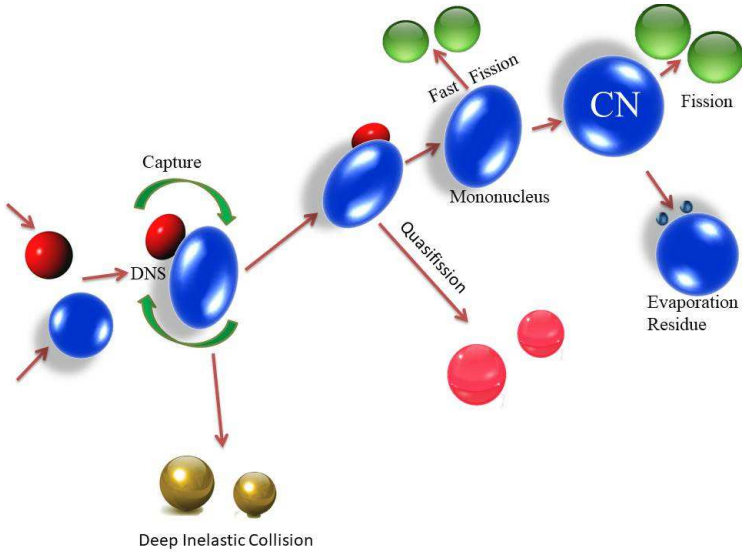

Figure 1.4: Schematic diagrams of various reaction processes prevail on the way towards the compound nucleus formation.

1.6 Motivation of the present work

The diverse applications of nuclear reactions rejuvenate the interest to explore the properties and the phenomena related to stable, unstable (exotic) and radioactive nuclei. In this domain, the strong nuclear force provides useful information not only because it explains the stability of the nucleus but it is also responsible for the understanding of fusion process. From the synthesis of super heavy nuclei, fusion reactions are proven to be extremely important in the dynamics of reactions that helps to unveil the unexplored physics. On the other hand, the fundamental decay process such as the nuclear fission also provides widespread information in the reaction mechanism and provides societal benefits spread from medical applications to the national security. Being a quantum many-body tunnelling problem, the comprehensive understanding of these complex phenomena is very challenging task and therefore several parameters such as energy, angular momentum, inertia, etc along with various degrees of freedom such as deformation, orientation, separation distance, etc are used to explain them. In view of above, the present thesis covers the fusion and subsequent decay mechanism associated with the stable and loosely

bound nuclei. Here, the formation process is analyzed using the Wong/ ℓ-summed Wong model and the decay process is explored via dynamical cluster decay model. Further, the role of different nuclear potentials are exercised in the reaction dynamics. The compound nuclei pertaining to different mass region of periodic table are explored in the present analysis with A_{CN} ranging from 28 to 268.

The detailed analysis and the observations are presented in chapters 3-7.

1.7 Planning of the Thesis

The thesis is planned in the following way:

After a comprehensive description of different nuclear models, nuclear formation and decay processes and the related quantities such as deformation, excitation energy, angular momentum, etc in this chapter, the overall work is covered in the subsequent chapters.

Chapter 2 carries out an overview of different methodologies opted for the analysis of fusion and subsequent decay mechanisms. In case of fusion process, the Wong/ℓ-summed Wong model is used to investigate the reaction dynamics. The total interaction potential defining the barrier of the colliding nuclei contains the nuclear interaction potentials comprising of the traditional proximity potential as well as the ones calculated using the Skyrme Energy Density Formalism (SEDF). Further, for the decay process, Dynamical Cluster-decay Model (DCM) is used to examine various decay modes observed in the complete fusion process. Besides this, other competing reaction processes such as incomplete fusion, quasi-fission, deep inelastic collision etc are also evaluated.

In **Chapter 3**, the fusion dynamics of superheavy $^{268}Sg^{*}$ compound nucleus formed via $^{30}Si+^{238}U$ reactions is analyzed using the Wong and ℓ-summed Wong model. It is observed that sub-barrier region exhibits large deviation in theoretical calculations in comparison with experimental data and hence signifies the importance of barrier modification effect. In view of this, the role of different Skyrme

forces such as SkT1, SSk, GSkI and KDE0v1 is analyzed along with usually used SIII Skyrme force. The GSkI and SSk Skyrme forces seem relatively good to analyze the below barrier fusion process while SkT1, KDE0v1, SIII forces are more appropriate to deal with the above barrier reaction dynamics. Since, the SSk and GSkI forces overestimate the experimental data at higher energies possibly because ℓ-values up to infinity are employed in Wong formula. For such cases, ℓ-summed Wong model is employed to handle the overestimation. Besides the nuclear interaction potentials, the role of deformations and optimum 'Hot' and 'Cold' orientations is also explored in the fusion dynamics. Moreover, the fusion cross-sections are predicted at extreme barrier energies using the SSk and GSkI Skyrme forces in the framework of ℓ-summed Wong model. Additionally, the fusion dynamics of ^{12}C+^{154}Sm, ^{16}O+^{154}Sm, ^{28}Si+^{154}Sm, ^{48}Ca+^{154}Sm reactions is extensively explored in view of mass, energy, deformation and orientation effect using the Skyrme forces SIII, GSkI and the proximity potential mod Prox 88.

In **Chapter 4**, the fusion and subsequent decay mechanisms of ^{136,144}Nd* compound nuclei formed in ^{40,48}Ca+^{96}Zr reactions are analyzed using the Wong/ℓ-summed Wong and Dynamical Cluster-decay Model (DCM) respectively. The role of different Skyrme interactions such as SIII, GSkI, SkT1, SkT2, SkT3 is investigated in view of fusion hindrance phenomena perceived in the sub barrier region. In the case of ^{40}Ca+^{96}Zr reaction, the hindrance phenomena is observed for the use of SIII, SkT1, SkT2 Skyrme forces. The GSkI Skyrme force on the other hand give relatively better comparison with data due to lower barrier height. When one neutron transfer channel is taken into account, the experimental data is adequately addressed for GSkI force while correction to 1n-transfer channel for SkT1 (or SIII, SkT2) continues with the poor fit. On the other hand, the fusion dynamics of ^{48}Ca+^{96}Zr reaction is adequately addressed via chosen Skyrme forces without the requirement of neutron transfer channel effect. In the decay process, the neck length ΔR and the barrier modification ΔV_B are used to explore the behavior of different Skyrme

interactions and neutron transfer effect in the decay process. The DCM based calculations signify that different Skyrme forces (GSkI and SkT1) provide similar mass distribution of outgoing fragments, except for the fission region. A drift from symmetric to relatively asymmetric fission is seen for GSkI and SkT1 force respectively. The experimental fusion excitation functions are duly reproduced using the GSkI and SkT1 Skyrme forces but the observation from ΔR signifies that GSkI Skyrme force requires less barrier modification than the SkT1 force. Thus, both the methodologies (ℓ-summed Wong and DCM) consistently advocate that the GSkI force is better to address the reaction dynamics particularly at below barrier region.

In **Chapter 5**, the DCM is used to examine the decay of light compound system i.e. ^{28}Si* at stellar energies in the range of 4-5 MeV. For this reaction of astrophysical interest, the recently developed eMSL07 Skyrme force is preferred which is known to include the extended density dependent term that makes it potentially suitable for the study of stellar reactions and neutron stars. The comparison of eMSL07 force is done with respect to traditionally used SIII and GSkI Skyrme forces. Using different Skyrme forces, the decay path of excited compound system is examined with respect to excitation energies and angular momentum effect. Apart from the emission of neutron, proton and alpha particles the emergence of ^{6}Li, ^{10}B and ^{14}N is also advocated in the decay of ^{28}Si* CN, independent of the choice of Skyrme forces, incident energy and angular momentum effect. Since, the fragile nature of the ^{6}Li may not allow it to survive the stellar conditions, therefore it may undergo breakup or radiative capture process. The possibilities of both the processes are examined using the eMSL07 Skyrme force. Finally, on the basis of cross sectional yield, it is observed that SIII Skyrme forces could not reproduce the experimental data while eMSL07 and GSkI force give decent result with the experimental observations.

After evaluating the reaction dynamics of stable projectile-target combinations, it is of further interest to extend the study for exotic projectile beam such as ^{6}Li using the suitable Skyrme interactions. Thus in **Chapter 6**, the dynamics of ^{6}Li+^{238}U

reaction is analyzed around the Coulomb barrier energies using the DCM model. In view of loosely bound nature of projectile ^{6}Li, the incomplete fusion (ICF) analysis is carried out along with complete fusion channel. For this reaction, the performance of NRAPR, SKRA, SQMC700, LNS, KDE0v1 Skyrme forces is investigated in reference to SIII and GSkI Skyrme forces. These forces are supposed to perform better for neutron rich case, therefore the choice of reaction is made accordingly. The barrier profile of chosen Skyrme forces depicts that NRAPR, SKRA and LNS cover the barrier characteristics of the remaining forces as well. Using these Skyrme forces, the fission cross-sections are successfully addressed at below barrier energies, however theoretical suppression at above barrier energies attributes towards the possible contribution of incomplete fusion process. In case of ICF, ^{6}Li is assumed to break into ^{4}He+^{2}H fragments, where the calculations for ICF is carried out for ^{4}He+^{238}U using selected forces at higher energies. It is observed that NRAPR, SKRA and LNS addressed the data nicely for complete and incomplete fusion processes. The NRAPR force requires less barrier alteration, and hence can be used as an alternate choice for determining the interaction potential. Further, the ℓ-dependent % barrier adaptation is also worked out for selected forces in reference to hindrance phenomena at sub barrier energies. Also, the prediction of cross-sections at sub barrier energies is carried out using the NRAPR Skyrme force.

Finally, in **Chapter 7**, the isotopic and isobaric analysis of Hf* and Pt* nuclei is carried out in context of decay process by using the dynamical cluster decay model. In this study, the nuclear proximity potential Prox 77 is used to examine the fusion-fission dynamics. The fragmentation paths of different isotopes are analyzed for spherical and deformed choice of nuclei. It is noticed that decay structures of ^{170,174}Hf* nuclei change drastically when deformations are taken into account. However, no noticeable change is observed in the decay path of ^{170,174}Pt* nuclei when deformed choice of fragmentation is used because the magnitude of deformation in Pt case is relatively small. Further, on exploring the isobaric mass distribution,

the effect of charge distribution Z is seen on the structure of decaying fragments while moving from Hf^* to Pt^* nucleus. In all the decaying systems, the evaporation cross-sections are nicely addressed at the available energies but the fission cross-sections show suppression at above barrier energies, which attributes towards the contribution from some nCN processes. Further, an effort is made to analyze the dynamical properties such as kinetic energy, velocity and time scale of the $^{170}Hf^*$ nucleus. The time scale of lighter and fission fragments implies that light fragments emit relatively earlier than the fission fragments.

Finally, **Chapter** 8 concludes the work reported in this thesis along with the scope of extension of this work for better understanding of dynamics involved.

Bibliography

[1] S-Gui Zhou, POS **37**, 373 (2016).

[2] M. Thoennessen , Rep. Prog. Phys. **67**, 1187-1232 (2004).

[3] R. F. Casten, B. M. Sherril, Prog. Part. Nucl. Phys. **45**, S171-S233 (2000).

[4] C. Beck *et al.*, Nucl. Phys. A **834**, 440c-445c (2010).

[5] M. Mazzocco *et al.*, Acta Phys. Polonica **44**, 437 (2013).

[6] K. Hagino, I. Tanihata and H. Sagawa, World Scientific Review, 9 (2019)

[7] H. J. Kluge, Nucl. Phys. A **701**, 495c (2002).

[8] A. Ozawa *et al.*, Nucl. Phys. A **693**, 32 (2002).

[9] J. Meng, P. Ring, Phys. Rev. Lett. **77**, 3963 (1996).

[10] L. F. Canto, P. R. S Gomes, R. Donangelo, and M. S. Hussein, Phys. Rep. **424**, 1 (2006).

[11] J. F. Liang, C. Signourni, Int. J. Mod. Phys. E **14**, 1121 (2005).

[12] A. Bohr and B. R. Mottelson, Nuclear Structure Vol. II: Nuclear deformations world Scientific ISBN 9810239807 (1998).

[13] M. G. Mayer, Phys. Rev. **75**, 1969 (1949); O. Haxel, D. Jensen, and H. E. Suess, Phys. Rev. **75**, 1766 (1949).

[14] A. Bohr and B. R. Mottelson, "Nuclear Structure, Vol. II," W. A. Benjamin, Reading, Massachusetts (1975).

[15] S. G. Nilsson, Mat. Fys. Medd. Dan. Vid. Selk. **29** 16 (1955).

[16] P. Verma, S. Singh, A. Bharti, S. K. Khosa, G. H. Bhat, J. A. Sheikh, Nucl. Phys. A **986**, 245-259 (2019).

[17] S. T. Butler, Phys. Rev. **80**, 1095 (1950); N. Austern, S. T. Butler, and H. McManus, Phys. Rev. **92**, 350 (1953).

[18] P. E. Hodgon, Rep. Prog. Phys. **50**, 1171-1228 (1987).

[19] W. E. Burcham, F. R. S., Contemp. Phys. **25**, 179-186 (1984).

[20] N. Bohr, Nature(London) **137**, 344 (1936).

[21] C. Y. Wong, Phys. Rev. C **86**, 064603 (2012).

[22] M. Beckerman *et al.*, Phys. Rev. Lett. **45**, 1472-1475 (1980).

[23] R. G. Stokstad *et al.* Z. Phys. A **295**, 269-286 (1980).

[24] M. Beckerman *et al.*, Phys. Rev. C **23** 1581-1589 (1981).

[25] W. Reisdorf *et al.* Phys. Rev. Lett. **49**, 1811-5 (1982).

[26] R. Pengo *et al.*, Nucl. Phys. A **411**, 255-274 (1983).

[27] S. Kalkal, S. Mandal, N. Madhavan *et al.*, Nucl. Phys. A **81**, 044610 (2010).

[28] Khushboo, N. Madhavan, S. Nath *et al.*, Phys. Rev. C **100**, 064612 (2019).

[29] V. V. Sargsyan, G. G. Adamian, N. V. Antonenko, W. Schied, and H. Q. Zhang, Phys. Rev. C **85**, 024616 (2012).

[30] P. H. Stelson, H. J. Kim, M. Beckerman, D. Shapira and R. L. Robinson, Phys. Rev. C **41**, 1584 (1990).

[31] N. Tajima and N. Suzuki, Phys. Rev. C **64**, 037301 (2001).

[32] M . Dasgupta, D. J. Hinde, N. Rowley, and A. M. Stefanini, Ann. Rev. Nucl. Part. Sci. **48**, 401-61 (1998)(and references therein).

[33] V. V. Sargsyan, G. G. Adamian, N. V. Antonenko, W. Scheid, and H. Q. Zhang, Phys. Rev. C **84** 064614 (2011).

[34] R. K. Gupta, M. Balasubramanium, R. Kumar, N. Singh, M. Manhas and W. Greiner. J. Phys. G: Nucl. Part. Phys. **31**, 631-644 (2005).

[35] J. Velkovska, C. R. Morton, R. L. McGrath, P. Chung, and I. Diózegi, Phys. Rev. C **59**, 1506 (1999).

[36] A. Nasirov, K. Kim, G. Mandaglio, G. Giardina and A. Muminove and Y. Kim, Eur. Phys. J. A **49**, 147 (2013).

[37] P. Eudes, Z. Basrak, F. Sebille, V. de la Motta and G. Royer, Eur. Phys. J. A **90**, 034609 (2014).

[38] M. Mazzocco, P. Scopel *et. al*, Nucl. Phys. A **746**, 497-500 (2004).

[39] A. Vitturi, Eur. Phys. J. Special Topics **156**, 237-248 (2008).

[40] L. Fortunato and A. Vitturi, AIP Conf. Proc. **853**, 390 (2006).

[41] M. Bender, P.-H. Hensen, Rev. Mod. Phys. **75**, 121 (2003).

[42] J. R. Stone, P.-G. Reinhard, Prog. Part. Nucl. Phys. **58**, 587-657 (2007).

[43] J. Euler, P. Klupfel and P.-G. Reinhard, J. Phys. G: Nucl. Part. Phys. **38**, 033101 (2011).

[44] D. Vautherin and M. Veneroni, Phys. Lett. **29b**, 203 (1969).

[45] D. Vautherin and D. M. Brink, Phys. Rev. C **5**, 626 (1972).

[46] D. Gogny, Proceedings of the international Conference on Nuclear Physics, Munich, edited by J. de Boer and H. J. Mang (North Holand, Amsterdam), P.48 (1973).

[47] J. D. Walecka, Ann. Phys. (N. Y.) **83**, 491 (1974).

[48] T. H. R Skyrme, Phil. Mag. **1**, 1043 (1956); Nucl. Phys. **9**, 615 (1959).

[49] Li Guo-qiang, Commun. Theor. Phys. **13**, 457-508 (1990).

[50] M. Brack, C. Guet, and H.-B Kakansson, Phys. Rep. **123**, 275-364 (1985).

[51] B. Grammoticos and A. Voros, Ann. Phys. **123**, 359 (1979).

[52] B. Grammoticos and A. Voros, Ann. Phys. **129**, 153 (1980)

[53] J. Bartel and K. Bencheikh, Eur. Phys. J. A **14**, 179-190 (2002).

[54] O. N. Ghodsi and F. Torabi, Phys. Rev. C. **92**, 064612 (2015).

[55] P.-G. Reinhard and M. Bender, Lect. Notes Phys. **641**, 249-268 (2004).

[56] L.-W. Chen, Che Ming. ko, B.-A. Li, and J. Xu, Phys. Rev. C **82**, 024321 (2010).

[57] B. Cochet and K. Bennaceus, P. Bonche, T. Duguet and J. Meyer, Nucl Phys. A **731**, 34-40 (2004).

[58] B. K. Agarwal, S. K. Dhiman and R. Kumar, Phys. Rev. C **73**, 034319 (2006).

[59] E. Chabanat, P. Bonche, P. Haesel, J. Meyer and R. Schaeffer, Nucl. Phys. A **627**, 710-746 (1997).

[60] J. Dobaczewski, H. Flocard and J. Treiner, Nucl. Phys. A **422**, 103-139 (1984).

[61] Z.-W Zuo, J-C Pei, X.-Y. Xiong and Yi Zhu, Chin. Phys. C **42**, 064106 (2018).

[62] S. Krewald, V. Klent, J. Speth and A. Faessler, Nucl. Phys. A **281**, 166 (1977).

[63] H. S. Kohler, Nucl. Phys. A **258**, 301 (1976).

[64] Giani, N. V. Glai and H. Sagawa, Phys. Lett. **106B**, 379 (1981).

[65] B. K. Agarwal, S. Shlomo and V. Kim. Au, Phys. Rev. C **72**, 014310 (2005).

[66] Z. Zhang and Lie-Wen Chen, Phys. Rev. C **94**, 064326 (2016).

[67] M. Dutra, O. Laurenço, J. S. SaMartin, A. Delfino, J. R. Stone and P. D. Stevenson, Phys. Rev. C **85**, 035201 (2012).

[68] R. Kumar, M. K. Sharma and R. K. Gupta, Nucl. Phys. A **870**, 42 (2011).

[69] J. Blocki, J. randrup, W. J. Swaitecki, and C. F. Tsang, Ann. Phys. (NY) **105**, 427 (1977).

[70] O. N. Ghodsi and A. Daei-Atollah, Phys. Rev. C **93**, 024612 (2016).

[71] I. Dutt and R. K. Puri, Phys. Rev. C **81**, 044615 (2010).

[72] I. Dutt and R. K. Puri, Phys. Rev. C **81**, 064609 (2010).

[73] R. Kumar and M. K. Sharma, Phys. Rev. C **85**, 054612 (2012).

[74] C. Y. Wong, Phys. Rev. Lett. **31**, 766 (1973).

[75] R. Kumar, M. Bansal, S. K. Arun and R. K. Gupta, Phys. Rev. C **80**,034618 (2009).

[76] V. Weisskopf, Phys. Rev. **52**, 295 (1937).

[77] N. Bohr and J. A. Wheeler, Phys. Rev. **56**, 426 (1939).

[78] F. K. Amanuel *et al.*, Phys. Rev. **84**, 024614 (2011).

[79] S. Mukherjee, A. Sharma, S. Sodaye, A. Goswami and B. S. Tomar, Int. J. Mod. Phys. E **15**, 237-245 (2006).

[80] M. K. Sharma, Unnati, B. P. Singh, R. Kumar, K. S. Golda, H.D. Bhardwaj, R. Prasad, Nucl. Phys. A **776**, 83-104 (2006).

[81] O. Hahn and F. Strassmann, Naturewiss **27**, 11 (1939).

[82] L. Meitner and O. R. Frisch, Nature **143**, 239 (1939).

[83] V. M. Strutinsky, Nucl. Phys. A **95** 420 (1967).

[84] K.-H. Schimdt, B. Jurodo, Rep. Prog. Phys. **81** 106301 (2018).

[85] G. G. Adamian, N. V. Antonenko, and W. Scheid, Phys. Rev. **68**, 034601 (2003).

[86] H. Q. Zhang, C. L. Zhang, C. L. Lin, A. K. Nasirov, G. Mandaglio, M. Manganaro and G. Giardina, J. Phys: Conf. Ser. **282**, 012013 (2011).

[87] G. Fazio *et al.*, Phys. Rev. C **72** 064614 (2005).

[88] V. V. Volkov, N. A. Antonenko, E. A. Cherenpanov, A. K. Nasirov, V. P. Permjakov, Phys. Lett. B **319** 425 (1993).

[89] S. Sodaye, R. Tripathi, B. V. John, K. Ramachandran, and P. K. Pujari, Phys. Rev. C **95**, 014612 (2017).

[90] R. K. Gupta and W. Greiner, Int. J. Mod. Phys. E **3** 335 (1994).

[91] R. K. Gupta, Cluster in Nuclei, Lecture Notes in Physics 818, Vol. I, edited by C. Beck (Springer-Verlag, Berlin), p. 223 (2010).

[92] M. Kaur, R. Kumar and M. K. Sharma, Phys. Rev. C **85** 014609 (2012).

[93] A. Kaur, S. Chopra, and R. K. Gupta, Phys. Rev. C **90**, 024619 (2014).

[94] I. Sharma, R. Kumar and M. K. Sharma, Eur. Phys. J. A, **53** 140 (2017).

[95] R. K. Gupta and W. Greiner, in heavy Elements and Related Related New Phenomena, edited by W. Greiner and R. K. Gupta (World Sceintific, Singapore), Vol I, p.397; ibid Vol I, p.536 (1999).

Chapter 2

Methodology

2.1 Introduction

The study of nuclear reactions aim at describing the mechanisms that nourish during the evolution of the nuclear systems when it undergoes a modification of its shape, energy, density, etc. due to nucleonic interactions of the colliding partners. These parameters act as an input to examine the reaction process and the cross sections corresponding to them. In the nuclear reactions, the knowledge of fusion cross-section is of a great importance because it helps to interpret the reaction dynamics adequately. The fusion cross-sections for low energy nuclear reactions are analyzed in terms of simple formula which starts with one-dimensional penetration probability through the potential barrier formed by Coulomb, nuclear, and centrifugal potentials. The fusion cross-sections can be estimated by using Wong formula [1–3] which is generally applied at energies near the Coulomb barrier. At higher incident energies, the modified version of Wong formula known as extended Wong model [4] is used in which explicit summation over ℓ-values is introduced, and works equally well in addressing the fusion as well as capture cross-sections.

For the better understanding of heavy-ion collision process, an appropriate knowledge of nucleus-nucleus potential is must. In view of this, different approaches are used to derive simple parametrization of nuclear potential and among them

'pocket formula' based proximity potential [5] and semi-classical energy density formalism based Skyrme interactions [6] are extensively used. Both the approaches follow different routes to deal with the nuclear proximity interaction. One is based upon the macroscopic study of the finite nucleus while the other is evolved from the microscopic analysis on finite and infinite nuclear matter. Within the Skyrme interactions, Hamiltonian energy in terms of local densities is used to evaluate the nuclear potential V_N, while in proximity potential, analytical expression of universal function and surface coefficient with suitable parameters are used to examine the nuclear part. Employing different nuclear potentials, fusion analysis is carried out using the Wong and ℓ-summed Wong model.

Once the fusion takes place, an excited compound system is formed which could not sustain the excessive mass, energy and angular momentum values, and therefore undergoes the decay process. To address the decay mechanism, Dynamical Cluster-decay Model (DCM) [7–14] is used, which works on the ideology of Quantum Mechanical Fragmentation Theory (QMFT) [15–22]. This theory is hinged on the fact that the fragments are pre-born in the compound nucleus prior to the decay process. In order to deal with pre-formed fragments, the quantum mechanical fragmentation approach is used for the estimation of preformation probability by solving the Schrodinger equation in mass fragmentation co-ordinate. After the fragments are formed, their penetration probability through the Coulomb barrier is determined using the semi-classical WKB approximation.

As the name suggests, the DCM model governs the binary decay of hot ($T\neq0$), rotated ($\ell\neq0$) and excited compound system that uses the collective clusterization approach to provide relevant information regarding the decay mechanism evolved. The DCM has an advantage to endorse the structure information through fragmentation potential and preformation probability of the decaying fragments. However, the origin of structural information lies in the deformations and the shell effects associated with the pre-born fragments. Incorporating various parameters such as level density, diffuseness parameter etc and degrees of freedom like deformations,

orientations, separation distance etc, the model is extensively used to address the decay dynamics of compound nuclei formed in heavy ion induced reactions.

The chapter is organized as follows: Wong and ℓ-summed Wong model is discussed in Sec 2.2. The interaction potentials that help to govern the fusion and decay processes are discussed in Sec 2.3. Finally, the decay dynamics examined using dynamical cluster decay model is explained in Sec 2.4.

2.2 Fusion analysis using Wong and ℓ-summed Wong model

The total fusion cross-section as a function of center of mass energy $E_{c.m.}$ for a given entrance channel A_1 and A_2 is expressed as

$$\sigma(E_{c.m.},\theta_i) = \frac{\pi\hbar^2}{2\mu E_{c.m.}}\sum_{\ell}^{\infty}(2\ell+1)P_\ell(E_{c.m.},\theta_i), \tag{2.1}$$

where P_ℓ is the penetration probability through the potential barrier V_T^ℓ(R,$E_{c.m.}$, θ_i) for each angular momentum (ℓ) wave, where the summation of all the P_ℓ is weighted with the factor (2ℓ+1). The total interaction potential V_T^ℓ(R,$E_{c.m.}$, θ_i) between projectile (Z_1, A_1) and target (Z_2, A_2) nuclei is defined as the sum of temperature-dependent Coulomb (V_C) [23], nuclear (V_N) [5] and centrifugal (V_ℓ) [23] potentials and is given by,

$$V_T^\ell(R,E_{c.m.},\theta_i) = V_N(A_i,R,T,\beta_{\lambda i},\theta_i) + V_C(Z_i,R,T,\beta_{\lambda i},\theta_i) + V_\ell(A_i,R,T,\beta_{\lambda i},\theta_i), \tag{2.2}$$

which duly incorporates the effect of static quadrupole deformations ($\beta_{\lambda_2 i}$) and optimum orientations θ_i(i=1,2) of the colliding nuclei (discussed later in sec 2.3). In 1973, Wong [1] provided an approximate expression for Eq. (2.1), which is termed as Wong formula, and works under the following three approximations,

Firstly, in parabolic approximation, the total interaction potential is assumed as parabolic function and the penetration probability P in terms of barrier height ($\mathrm{V}_B^\ell(\mathrm{E}_{c.m.},\theta_i)$), barrier position ($R_B^\ell$) and curvature ($\hbar\omega_\ell(E_{c.m.},\theta_i)$) is calculated analytically using the Hill-Wheeler [24] formula as

$$P_\ell = \left[1+\exp\left(\frac{2\pi(V_B^\ell(E_{c.m.},\theta_i)-E_{c.m.})}{\hbar\omega_\ell(E_{c.m.},\theta_i)}\right)\right]^{-1}, \tag{2.3}$$

with $\hbar\omega_\ell(E_{c.m.},\theta_i)$ determined at the barrier position $R=R_B^\ell$ corresponding to the barrier height $V_B^\ell(E_{c.m.},\theta_i)$ as

$$\hbar\omega_\ell(E_{c.m.},\theta_i) = \hbar\left[|d^2V^\ell(R)/dR^2|_{R=R_B^\ell}/\mu\right]^{1/2}, \tag{2.4}$$

and, the R_B^ℓ obtained from the condition

$$|dV_T^\ell(R)/dR|_{R=R_B^\ell} = 0 \tag{2.5}$$

Secondly, the barrier characteristics are assumed to be ℓ-independent, which implies that barrier height, barrier position, and barrier curvature are calculated for s-wave only i.e.

i) $\hbar\omega_\ell \approx \hbar\omega_0$, $R=R_B^0$, and (ii) $V_B^\ell \approx V_B^0 + \frac{\hbar^2\ell(\ell+1)}{2\mu {R_B^0}^2}$,

where,

$$V_B^0 = V_P(A_i, R=R_B^0, \beta_{\lambda i}, E_{c.m.}, \theta_i) + V_C(Z_i, R=R_B^0, \beta_{\lambda i}, E_{c.m.}, \theta_i) \tag{2.6}$$

Lastly, in the continuum approximation, the angular momentum ℓ is considered as a continuum variable and the summation in Eq. (2.1) is replaced by an integral

$$\sigma(E_{c.m.},\theta_i) = \frac{\pi\hbar^2}{2\mu E_{c.m.}}\sum_{\ell=0}^{\infty}(2\ell+1)P_\ell(E_{c.m.},\theta_i) \rightarrow \frac{\pi\hbar^2}{2\mu E_{c.m.}}\int_0^{\infty} d\ell(2\ell+1)P_\ell(E_{c.m.},\theta_i) \tag{2.7}$$

Using these approximations, the fusion cross-section is obtained as

$$\sigma(E_{c.m.},\theta_i) = \frac{{R_B^0}^2\hbar\omega_0}{2E_{c.m.}}\ln\left[1+\exp\left(\frac{2\pi}{\hbar\omega_0}(E_{c.m.}-V_B^0(\theta_i)\right)\right], \tag{2.8}$$

which on integration over the orientation angle θ_i (i=1,2) at given center of mass energy $E_{c.m.}$ gives,

$$\sigma(E_{c.m.}) = \int_{\theta_i=0}^{\pi/2}\sigma(E_{c.m.},\theta_i)sin\theta_i d\theta_i. \tag{2.9}$$

The fusion cross-sections calculated using the above mentioned Wong formula provide decent description of experimental data at energies near the Coulomb barrier. However, at sub and above barrier energies, it shows deviation from the experimental data. The sub barrier anomalies are addressed by including the structural effects and different forms of nuclear potentials V_N while the above barrier energies being independent of structural and V_N effects are resolved by introducing ℓ-summed extended Wong model [4]. The fusion cross sections in ℓ-summed Wong model is determined as

$$\sigma(E_{c.m.},\theta_i) = \frac{\pi\hbar^2}{2\mu E_{c.m.}}\sum_{\ell=0}^{\ell_{max}}(2\ell+1)P_\ell(E_{c.m.},\theta_i), \tag{2.10}$$

where ℓ_{max} is the maximum angular momentum calculated using the sharp cut-off approximation [25]. Also, the barrier penetration probability P_ℓ is determined in terms of ℓ-dependent barrier characteristics such as V_B^ℓ, R_B^ℓ and $\hbar\omega_B^\ell$. In other words, the explicit ℓ-dependence is introduced in the extended Wong model and the

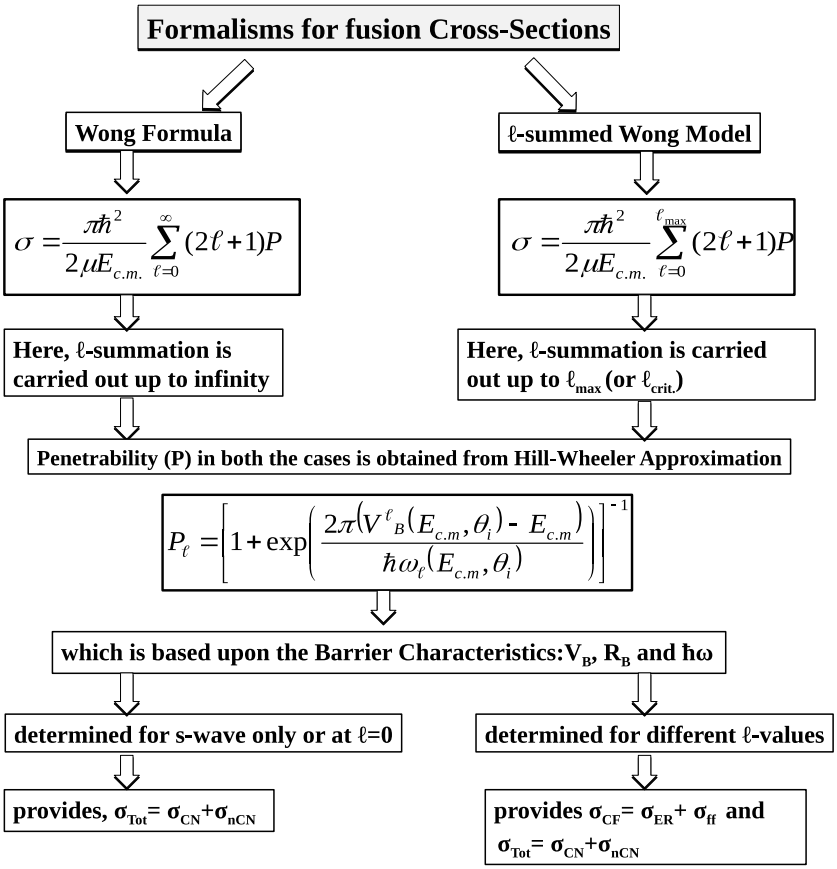

Figure 2.1: Flow chart for estimation of fusion cross sections

summation over partial waves is limited to ℓ_{max} value. This makes the model more accessible for the calculations of fusion and the capture processes. For simplification, a flow chart of Wong and ℓ-summed Wong formalism is shown in Fig 2.1.

Further, to estimate the neutron transfer effect, the penetration probability P_ℓ(or transmission probability) is reformulated as

$$P_\ell(E_{c.m.}) = P_\ell + \sum_i \frac{k_i}{k_0} P_\ell^i, \ i = 1, 2 \tag{2.11}$$

where, P^i and k_i is Hill-Wheeler penetrability and wave vectors of different channels (such as ^{40}Ca,^{41}Ca.....^{48}Ca respectively). The wave vector of each channel is expressed as

$$k_i = \sqrt{\frac{2\mu(E_{c.m.(i)} - V_i)}{\hbar^2}} \tag{2.12}$$

with

$$\mu = \frac{m_1 m_2}{m_1 + m_2} \tag{2.13}$$

here μ represents the reduced mass and m_1, m_2 corresponds to the mass of projectile and target nuclei. $E_{c.m.(i)}$ denotes the center of mass energy, and V_i is the interaction potential. Here, the center of mass energy, $E_{c.m.(i)}$ of different transfer channels such as ^{40}Ca,^{41}Ca... is determined using the Q value, given as

$$E_{c.m.(i)}(^{40+i}Ca) = E_{c.m.}(^{40}Ca) + Q(^{40+i}Ca), i = 1, 2... \tag{2.14}$$

Replacing the extended Wong expression in Eq. (2.10) with Eq. (2.11), the total fusion cross section is expressed as

$$\sigma(E_{c.m.}) = \frac{\pi\hbar}{2\mu E_{c.m.}} \sum_{\ell=0}^{\ell_{max}} (2l+1)[P_\ell + \sum_i \frac{k_i}{k_0} P_\ell^i], i = 1, 2. \tag{2.15}$$

For any theoretical model, the comprehensive information of total interactions potentials between the reacting nuclei is essential, therefore brief discussion of each potential used in this thesis work is given in the following section.

2.3 Interaction potential

The total interaction potential between two reacting nuclei is defined as the combined effect of repulsive Coulomb potential, centrifugal potential and the attractive nuclear potential, as

$$V(R,T) \quad = V_C(R, Z_i, \beta_{\lambda i}, \theta_i, T) + +V_\ell(R, A_i, \beta_{\lambda i}, \theta_i, T) + V_N(R, A_i, \beta_{\lambda i}, \theta_i, T). \quad (2.16)$$

In the above equation, each potential term includes the temperature, deformation (β_i) and orientation (θ_i) effect via radius vector R_i,

$$R_i(\alpha_i, T) = R_{0i}(T)[1 + \sum_\lambda \beta_{\lambda i} Y_\lambda^{(0)}(\alpha_i)], \quad (2.17)$$

with [26]

$$R_{0i}(T) = [1.28A_i^{1/3} - 0.76 + 0.8A_i^{-1/3}](1 + 0.0007T^2) \quad (2.18)$$

In Eq. (2.17), α_i refers to an angle formed by radius vector R_i of the colliding nuclei with the symmetric axis, measured in the clockwise direction. A plot representing the nature of different potentials is shown in Fig. 2.2 and a brief discussion of each component is given in the following subsections.

2.3.1 Coulomb Potential

It is the repulsive potential existing between two charged nuclei separated by radial distance R. For the spherically symmetric case, the Coulomb potential has the form

$$V_c(Z_i, T) \quad = \quad \frac{Z_1 Z_2 e^2}{R(T)} \quad (2.19)$$

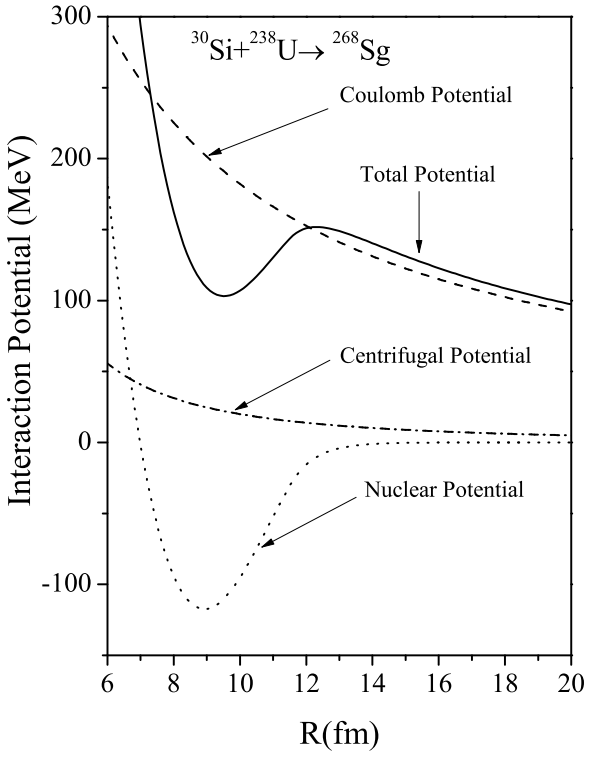

Figure 2.2: Plot of different potentials that contribute in the heavy ion fusion process.

which, in the case of deformed and the oriented nuclei is modified [27–29] as

$$V_c(Z_i, \beta_{\lambda i}, \theta_i, \alpha_i, T) = \frac{Z_1 Z_2 e^2}{R(T)} + 3Z_1 Z_2 e^2 \sum_{\lambda, i=1,2} \frac{1}{2\lambda+1} \frac{R_i^{\lambda}(\alpha_i, T)}{R(T)^{\lambda+1}} Y_{\lambda}^{(0)}(\theta_i) \Big[\beta_{\lambda i} + \frac{4}{7}\beta_{\lambda i}^2 Y_{\lambda}^{(0)}(\theta_i)\Big], \quad (2.20)$$

$\beta_{\lambda i}$ (λ =2,3,4 for i=1,2) represents the nuclear deformations and $Y_{\lambda}^{(0)}(\theta_i)$ refers to spherical harmonics function.

2.3.2 Centrifugal Potential

It is an apparent potential experienced by any object when it moves in a circular path. It arises due to the inertia of the body and always directed in the outward

direction. The potential effectively behaves as repulsive potential due to the contribution of $\frac{\ell(\ell+1)}{R^2}$ term attributed from rotational or angular momentum ℓ effect via

$$V_\ell(A_i, T, \beta_{\lambda i}, \theta_i, \alpha_i) = \frac{\ell(\ell+1)\hbar^2}{2I(T)}. \tag{2.21}$$

Here, I(T) refers to the moment of inertia, defined under two different conditions; (a) when the two bodies with nucleon mass m and reduced mass μ move with touching configuration [30], i.e. R= R_1+R_2, then

$$I_S(T) = \mu R^2 + \frac{2}{5}A_1 m R_1^2(\alpha_1, T) + \frac{2}{5}A_2 m R_2^2(\alpha_2, T). \tag{2.22}$$

and (b) when the bodies are separated with R > R_1+R_2, they are known to interact by non-sticking limitation as [31].

$$I_{NS}(T) = \mu R^2 \tag{2.23}$$

For the fusion process, where R > R_1+R_2 the non-sticking limit is preferred for the addressal of fusion cross-sections using the Wong formula, while to assess the decay cross-sections, where R= R_1+R_2 the sticking limit is more appropriate, which results in the higher value of angular momentum.

2.3.3 Nuclear Potential

The nuclear part of interaction potential comes into the picture when two nuclei are separated by a distance less than $\sim$ 2 fm. Experimentally, it is difficult to determine the nuclear potential between the projectile and target nucleon due to the contribution of large number of interactions between them, therefore simple concept of parameterizations is used to obtain the nuclear interaction potentials. In this section, the macroscopic formalism based proximity 77 potential [5] and

microscopic formalism based Skyrme interactions [6] are discussed. Firstly, the proximity potential is discussed in the upcoming section.

Proximity Potential

The proximity potential is based upon the 'pocket formula' that describes the nuclear force as the product of two functions; one depends on the shape and geometry of the interacting nuclei and the other is the function of shortest distance s_0 between them. Initially, the temperature independent formula was developed for the spherical nuclei, which later on modified by the authors of [32] by adding temperature dependence and deformation effect as

$$V_N(A_i, R, T, \beta_{\lambda i}, \theta_i) = 4\pi \bar{R}(T)\gamma b(T)\Phi(s_0(T)). \tag{2.24}$$

The terms γ, b, $\bar{R}$ referred to the shape and geometry of two reacting nuclei and $\Phi(s_0)$ is the universal function with separation distance s_0. Here, γ stands for surface energy coefficient obtained from Myers and Swaiteki formula [33] having the form

$$\gamma = \gamma_0 \left[1 - k_s \left(\frac{N-Z}{A}\right)^2\right] MeVfm^{-2} \tag{2.25}$$

where N and Z are the neutron and proton numbers of the parent nucleus respectively with surface energy constant γ_0 and surface asymmetry constant k_s having the value 0.9517 MeV/fm^2 and 1.7826 respectively. The surface width (or surface diffuseness) 'b' of the nuclear surface lies close to unity i.e. 0.99, which on adding the temperature dependence reads as b(T)=0.99(1+0.009T^2) [26].

The mean curvature radius $\bar{R}$ for spherical nuclei is given as [5]

$$\overline{R} = \frac{R_1 R_2}{R_1 + R_2} \tag{2.26}$$

which for deformed and oriented nuclei is modified as [5]

$$\frac{1}{\bar{R}^2} = \frac{1}{R_{11}R_{12}} + \frac{1}{R_{21}R_{22}} + \left[\frac{1}{R_{11}R_{21}} + \frac{1}{R_{12}R_{22}}\right] sin^2\phi + \left[\frac{1}{R_{11}R_{22}} + \frac{1}{R_{21}R_{12}}\right] cos^2\phi. \quad (2.27)$$

Here, R_{i1} and R_{i2} represent the radii of curvature of the two nuclei (i=1,2) at the points of closest approach and ϕ is the azimuthal angle between the principal planes of curvature of two nuclei, taken as ϕ=0^o for co-planar nuclei.

The parametrization of universal function $\phi(\zeta=s_0/b)$ was obtained using the nuclear Thomas-Fermi model with Seyler-Blanchard phenomenological nucleon-nucleon interaction expressed as

$$\Phi(\zeta) = \begin{cases} -\frac{1}{2}(\zeta - 2.54)^2 - 0.0852(\zeta - 2.54)^3; \zeta \leq 1.2511 \\ -3.437exp(-\frac{\zeta}{0.75}); \zeta \geq 1.2511 \end{cases} \quad (2.28)$$

with, ζ=s_0/b is minimum separation distance defined in terms of surface diffuseness b. The above discussed proximity potential is labelled as proximity 1977. On adjusting the surface energy coefficients and parametrization in universal function, other versions of proximity formalism such as proximity 88, mod prox 88 etc are made available in literature [34] which adequately helps to resolve the sub barrier anomalies of fusion reaction.

Skyrme Energy Density Formalism (SEDF)

The original form of phenomenological Skyrme interaction parameterized by Vautherin and Brink [6, 35, 36] is referred to as standard Skyrme interactions in which the total energy density of the nucleus is expressed in terms of Hamiltonian density as

H= K + H_0 + H_3 + H_{eff} + H_{fin} + H_{SO} + H_{sg}

where, K= $(\hbar^2/2\mathrm{m})\tau$ is the kinetic energy term and H_0, H_3, H_{eff}, H_{fin}, H_{SO}, H_{sg} are zero-range term, density-dependent, effective mass, finite range, spin-orbit and tensor coupling with spin and gradient terms respectively, that reads as

$$H_0 = \tfrac{1}{4}t_0\left[(2+x_0)\rho^2 - (2x_0+1)(\rho_n^2+\rho_p^2)\right] \tag{2.29}$$

$$H_3 = \frac{1}{24}t_3\rho^\alpha\left[(2+x_3)\rho^2 - (2x_3+1)(\rho_n^2+\rho_p^2)\right] \tag{2.30}$$

$$H_{eff} = \frac{1}{8}\left[t_1(2+x_1)+t_2(2+x_2)\right]\rho\tau$$

$$-\frac{1}{8}\left[t_1(2x_1+1)-t_2(2x_2+1\right](\rho_n\tau_n+\rho_p\tau_p) \tag{2.31}$$

$$H_{fin} = \frac{1}{32}\left[3t_1(2+x_1)-t_2(2+x_2)\right](\vec{\nabla}\rho)^2$$

$$-\frac{1}{32}\left[3t_1(2x_1+1)+t_2(2x_2+1)\right]$$

$$\times\left[(\vec{\nabla}\rho_n)^2+(\vec{\nabla}\rho_p)^2\right] \tag{2.32}$$

$$H_{SO} = -\tfrac{1}{2}W_0\left[\rho\vec{\nabla}\cdot\vec{J}+\rho_n\vec{\nabla}\cdot\vec{J}_n+\rho_p\vec{\nabla}\cdot\vec{J}_p\right] \tag{2.33}$$

$$H_{sg} = -\frac{1}{16}\left[(t_1x_1+t_2x_2)\vec{J}^2\right]$$

$$+\left[\frac{1}{16}(t_1-t_2)(J_p^2+J_n^2)\right] \tag{2.34}$$

Here, ρ=ρ_n+ρ_p, τ=τ_n+τ_p and $\vec{J}=\vec{J}_n$+$\vec{J}_p$ are nuclear density, kinetic energy density and spin-orbit density where n and p represent neutron and proton respectively. The standardized Hamiltonian with single density-dependent term is suitable for the study of finite nuclei, however, insufficient for the analysis of very high density nuclear matter such as neutron stars. In order to generalize the Skyrme interac-

tions for finite nuclei and neutron star matter, efforts have been made to extend the Skyrme Hamiltonian by making value additions in the density and momentum-dependent terms. The more natural and convenient way to extend the Skyrme force is to add the higher order density-dependent term that imparts large impact on the characteristics behavior of the Skyrme forces. Such an effort has been made by the authors of Ref. [37] that replaces the density dependent H_3 term with

$$\frac{1}{4}[\sum_{i=0}^{3} t_{3i}\rho^{\alpha_1}[(2+x_{3i})\rho^2 - (2x_{3i}+1)(\rho_n^2+\rho_p^2)] \tag{2.35}$$

and proposed the generalized GSkI, GSkII and SSk Skyrme forces. In the present thesis, various sets of Skyrme forces such as NRAPR [38], SQMC700 [39], LNS [40], KDE0v1 [41], SKRA [42], SkT1, SkT2, SkT3 [43], GSkI [37], SSK [37], have been used to test their behavior in the nuclear reaction dynamics. The choice for Skyrme forces is made from the work of Dutra *et al.* [44], that separated out the few Skyrme interactions from the set of 240 Skyrme forces. Using these Skyrme forces, heavy-ion reactions comprising of the compound nucleus and non-compound nucleus processes are duly analyzed in the vicinity of Coulomb barrier.

Analogous to proximity potentials, each Skyrme force has a different set of parameters such as $t_0 \sim t_3$, $x_0 \sim x_3$, α, W_0, that are determined by fitting various ground state properties of finite nuclei and hence the different Skyrme forces exhibit different barrier characteristics. However, the density functionals such as nuclear density (ρ), kinetic energy density (τ) and the spin-orbit density ($\vec{J}$) of the nucleus are obtained from the simple Thomas-Fermi approach as discussed below.

Density functionals

The density functionals were determined using the Hartree-Fock formalism [35], which makes such calculations relatively more complex. Subsequently, the semiclassical approximation was preferred over the exact quantum mechanical solution of

densities. Within this approximation, τ_q and $\vec{J}_q$ as a function of ρ_q and its derivatives, are obtained from so-called Extended Thomas-Fermi model [45]. The ETF functionals are of semiclassical in nature and being so, they are suited well for the calculations and also their results lie very close to the one obtained from exact variation. A brief overview of each density functional is discussed below.

1. *Nuclear Density:* The nuclear density (ρ) obtained from two-parameter Fermi density distribution [45, 46] (made temperature-dependent via R_i) is given as

$$\rho_i(z_i) = \rho_{0i}(T)\left[1+\exp\left(\frac{z_i - R_i(T)}{a_i(T)}\right)\right]^{-1} \quad -\infty \leq z \leq \infty \tag{2.36}$$

where, central density $\rho_{0i}(T)$ has the form

$$\rho_{0i}(T) = \frac{3A_i}{4\pi R_i^3(T)}\left[1+\frac{\pi^2 a_i^2(T)}{R_i^2(T)}\right]^{-1}. \tag{2.37}$$

and $z_2 = R - z_1 = [R_1(\alpha_1) + R_2(\alpha_2) + s] - z_1$.

The ρ_i is defined as $\rho_i = \rho_{n_i} + \rho_{p_i}$, and the local densities of neutron and proton are obtained by $\rho_{n_i} = (N_i/A_i)\rho_i$ and $\rho_{p_i} = (Z_i/A_i)\rho_i$.

The radius vector $\mathrm{R}_i(T)$ as per Eq. (2.17) comprises of half density radii R_{0i} and a_i is the surface thickness parameter which for SEDF case are obtained from the polynomial fits of [48, 49]. For temperature dependence in half density radii (R_{0i}) and surface thickness parameter a_i is introduced as per [50]

$$\begin{aligned} R_{0i}(T) &= R_{0i}(T=0)[1+0.0005T^2], \\ a_i(T) &= a_i(T=0)[1+0.01T^2]. \end{aligned} \tag{2.38}$$

2. *Kinetic energy density*: In the Extended Thomas-Fermi formalism [46], the

kinetic energy density is determined from the expression

$$\tau_q(\vec{r}) = \frac{3}{5}(3\pi^2)^{2/3}\rho_q^{5/3} + \frac{1}{36}\frac{(\vec{\nabla}\rho_q)^2}{\rho_q} + \frac{1}{3}\Delta\rho_q + \frac{1}{6}\frac{\vec{\nabla}\rho_q\cdot\vec{\nabla}f_q + \rho_q\Delta f_q}{f_q} - \frac{1}{12}\rho_q\left(\frac{\vec{\nabla}f_q}{f_q}\right)^2 + \frac{1}{2}\rho_q\left(\frac{2m}{\hbar^2}\right)^2\left(\frac{W_0}{2}\frac{\vec{\nabla}(\rho+\rho_q)}{f_q}\right)^2, \quad (2.39)$$

where the first term represents well known Thomas-Fermi expression for kinetic energy density and remaining terms show their contribution from semi-classical correction to kinetic energy density up to second order term (being enough for numerical convergence) with W_0 is the spin orbit parameter and f_q is the effective mass form factor (q = n or p) [46] given as

$$f_q(\vec{r}) = 1 + \frac{2m}{\hbar^2}\frac{1}{4}\left\{t_1(1+\frac{x_1}{2}) + t_2(1+\frac{x_2}{2})\right\}\rho(\vec{r}) - \frac{2m}{\hbar^2}\frac{1}{4}\left\{t_1(x_1+\frac{1}{2}) - t_2(x_2+\frac{1}{2})\right\}\rho_q(\vec{r}). \quad (2.40)$$

3. *Spin-orbit Density*: The Spin term $J(\vec{r})$ being pure quantal property with no classical analog, have negligible contribution to TF in the lowest order. Therefore, the second order contribution in terms of local densities ρ_q and/ or ρ (q= n or p) and spin orbit parameter W $_0$ is used which defines $J(\vec{r})$ [46] as

$$\vec{J}_q(\vec{r}) = -\frac{2m}{\hbar^2}\frac{1}{2}W_0\frac{1}{f_q}\rho_q\vec{\nabla}(\rho+\rho_q), \quad (2.41)$$

In the semi-classical energy density formalism, the densities are added as per frozen approximation i.e.

$$\rho = \rho_1 + \rho_2 (i = 1, 2), \quad (2.42)$$

$$\begin{aligned}\tau(\rho) &= [\tau_{1n}(\rho_{1n}) + \tau_{1p}(\rho_{1p})] + [\tau_{2n}(\rho_{2n}) + \tau_{2p}(\rho_{2p})],\\ \vec{J}(\rho) &= [\vec{J}_{1n}(\rho_{1n}) + \vec{J}_{1p}(\rho_{1p})] + [\vec{J}_{2n}(\rho_{2n}) + \vec{J}_{2p}(\rho_{2p})],\end{aligned} \tag{2.43}$$

Finally, the nuclear potential in terms of Hamiltonian density is calculated by using the Slab approximation method [5, 47] as

$$\begin{aligned}V_N(R) &= 2\pi\bar{R}\int_{s_0}^{\infty} e(s)ds\\ &= 2\pi\bar{R}\int \left\{H(\rho,\tau,\vec{J}) - [H_1(\rho_1,\tau_1,\vec{J}_1) + H_2(\rho_2,\tau_2,\vec{J}_2)]\right\} dZ\\ &= 2\pi\bar{R}\int \left\{(H(\rho) - [H_1(\rho_1) + H_2(\rho_2)]) + \left(H(\vec{J}) - [H_1(\vec{J}_1) + H_2(\vec{J}_2)]\right)\right\} dZ\\ &= V_P(R) + V_J(R).\end{aligned} \tag{2.44}$$

where, $\bar{R}$ represents the geometry of the systems and e(s) is the universal function depending on the separation distance s_0. The advantage of calculating nuclear potential using SEDF route is that one can find individual contribution of Spin independent and spin dependent potential. Consequently one may see the corresponding effect of such spin saturated and spin unsaturated components in the overall evolution of nuclear dynamics.

The nuclear potential plays effective role in describing the fusion as well as decay processes, therefore different nuclear potentials are applied in the Wong and Dynamical Cluster-decay Model(DCM) (discussed in the next section) for comprehensive analysis of heavy-ion reaction dynamics.

2.4 Decay analysis of exotic nuclei using the Dynamical Cluster-decay Model (DCM)

For the decay process, dynamical cluster decay model is used which provides a relevant description of the two body channels in the decay of hot and excited compound

nucleus. The essential components of this model are (i) collective potential energy obtained using the Strutinsky renormalization method [51], and (ii) the kinetic energy defined by the mass parameter $B_{\eta\eta}$. The kinetic energy (K) term is known to govern the dynamics of the nuclear system whereas the potential energy (V) defines the static properties of the compound nucleus. Both the potential and kinetic energy of the system express the total Hamiltonian in terms of collective co-ordinates as

$$H = K(\eta, \beta, \theta, R, \varepsilon) + V(\eta, \beta, \theta, R, \varepsilon), \tag{2.45}$$

where, η stands for mass (and charge) asymmetry [15, 21] defined as, $\eta_A = (A_1 - A_2)/(A_1 + A_2)$ (and $\eta_Z = (Z_1 - Z_2)/(Z_1 + Z_2)$; $\beta_{\lambda i}$ (λ=2, 3, 4... and i=1, 2) is the deformation co-ordinate with $\theta_i (i = 1, 2)$ as the orientation degree of freedom of deformed nuclei. The relative separation coordinate between the two fragments is represented by 'R' and ε is the neck parameter which is expressed as the ratio of actual barrier E_0 to the fixed barrier height E' of two center oscillator i.e. $\varepsilon = E_0/E'$. For $\epsilon = 1$, the neck is considered to be fully squeezed in, while for broad neck formation $\epsilon = 0$ (corresponding to the asymptotic region).

For potential energy V(η, β, θ, R, ε), the minimization in η-co-ordinate automatically fixes the β, θ and ε co-ordinates. Hence, the Schrödinger equation in terms of η and R variables can be written as

$$H(_\eta, R)\psi(\eta, R) = E(\eta, R)\psi(\eta, R) \tag{2.46}$$

where

$$H(\eta, R) = K(\eta) + K(R) + K(\eta, R) + V(\eta) + V(R) + V(\eta, R) \tag{2.47}$$

and

$$E(\eta, R) = E(\eta) + E(R) \tag{2.48}$$

Since the contribution of coupling terms K(η, R) and V(η, R) are expected small [15, 16], therefore these terms are not included in the further calculations. The decoupled Schrödinger equation in η and R co-ordinate is written as

$$\left[-\frac{\hbar^2}{2\sqrt{B_{\eta\eta}}}\frac{\partial}{\partial\eta}\frac{1}{\sqrt{B_{\eta\eta}}}\frac{\partial}{\partial\eta}+V(\eta)\right]\psi^{\nu}(\eta)=E^{\nu}_{\eta}\psi^{\nu}(\eta), \tag{2.49}$$

and

$$\left[-\frac{\hbar^2}{2\sqrt{B_{RR}}}\frac{\partial}{\partial R}\frac{1}{\sqrt{B_{RR}}}\frac{\partial}{\partial R}+V(R)\right]\psi^{\nu}(R)=E^{\nu}_{R}\psi^{\nu}(R), \tag{2.50}$$

where quantum number ν= 0,1,2...etc refers to the vibrational states of the nucleus and V(η), V(R) represent the total interaction potential and the fragmentation potential respectively. The solution of Schrodinger equation in R motion provides the penetration probability of each fragment through the barrier V(R) (discussed in section 2.2), while solving the Schrödinger equation in η provides the preformation probability of the favorable channels, which is basically governed by fragmentation potential V(η), as discussed below.

2.4.1 Fragmentation potential

It is defined as the potential experienced by the nascent fragments born prior to the decay of compound nucleus. It is expressed as the sum of binding energy (B.E) of the fragments and the interaction potential, V(R,T). The binding energy of each fragment is determined using the macro-microscopic Strutinsky renormalization method, B.E=V_{LDM}+δU [51], where temperature-dependent liquid drop V_{LDM} is the macroscopic part of the binding energy, estimated using the Davidson plots [52] in the framework of the semi-empirical mass formula of Seeger [53]. However, the shell corrections δU are estimated according to the "empirical" formula of Myers and Swaitecki [33], also taken to be T-dependent. In the fragmentation potential, the

inclusion of shell effects along with the surface effects such as deformations and orientation of the nuclei help to describe the extra stability of the fragments pre-born in the compound system. Mathematically, the fragmentation potential is written as

$$\begin{aligned} V(\eta, R, \ell, T) &= \sum_{i=1}^{2} V_{LDM}(Z_i, A_i, T, \beta_{\lambda i}) + \sum_{i=1}^{2} \delta U_i \exp(-T^2/T_0^2) \\ &+ V_C(Z_i, R, T, \beta_{\lambda i}, \theta_i, \phi) + V_N(A_i, R, T, \beta_{\lambda i}, \theta_i, \phi) \\ &+ V_\ell(A_i, R, T, \beta_{\lambda i}, \theta_i, \phi). \end{aligned} \tag{2.51}$$

2.5 Solution of Schrödinger equation in η co-ordinate

The fragmentation potential obtained using the equation Eq. (2.51) goes as input to the stationary Schrödinger equation Eq. (2.49), which on solving numerically, ($\mid \psi^{\nu}(A_2) \mid^2$), in η co-ordinate gives the preformation probability P_0 of decaying fragments as

$$P_0(A_2) \propto \mid \psi^{\nu}(A_2) \mid^2 \tag{2.52}$$

In the case of ground state process, vibration state ν=0 is occupied. However, if the system is excited, the higher values of ν(=1,2,3....) also start contributing. The possible consequences of such excitations are included by assuming Boltzmann like occupation of the excited state as

$$\mid \psi(\eta) \mid^2 = \sum_{\nu=0}^{\infty} \mid \psi^{\nu}(\eta) \mid^2 exp(\frac{-E^{\nu}}{T}) \tag{2.53}$$

Then, the preformation yield or mass distribution yield, proportional to the probability $\mid \psi_R^{\nu}(A_2) \mid^2$ of a certain mass fragment η at fixed R, when scaled to say, A_2 of one of the fragment is given by

$$P_0 = \mid \psi_R^{\nu}(A_2) \mid^2 \frac{2}{A}\sqrt{B_{\eta\eta(A_2)}} \tag{2.54}$$

The term B$\eta\eta$, in the above equation, is the classical mass parameter of Kroger and Scheid [57] which is based on the hydrodynamical mass flow.

2.5.1 Analytical calculations for penetration probability 'P'

Instead of solving Eq. (2.50) in R motion, an analytical expression using WKB approximation [58] is employed to determine the penetration probability of fragments through the barrier, as

$$P = \exp\left[-\frac{2}{\hbar}\int_{R_a}^{R_b}\{2\mu[V(R,T) - Q_{eff}]\}^{1/2}dR\right]. \tag{2.55}$$

V(R,T) is the interaction potential and the $Q_{eff.}$ is the effective Q value of the decay process such that V(R_a)= V(R_b)=$Q_{eff.}$=TKE. Here, Q_{eff} is the total kinetic energy value shared between the two fragments, while the fraction of kinetic energy carried away by light particle [59] is defined as

$$K.E. = (A_1/A_{CN})Q_{eff}. \tag{2.56}$$

where A_1 and A_{CN} is the mass number of the lighter fragment and the compound system. However, V(R_a) and V(R_b) as discussed above refer to the potentials at R_a and R_b, with R_a and R_b representing the entry and exit points of the tunnelling path. The first turning point is defined as

$$\begin{aligned} R_a &= R_1(\alpha_1, T) + R_2(\alpha_2, T) + \Delta R(\eta, T) \\ &= R_t(\alpha_i, T) + \Delta R(\eta, T), \end{aligned} \tag{2.57}$$

Here, R_i is the radius vector of each fragment calculated as per Eq. (2.17) and ΔR is the relative separation distance between the two fragments, which is assumed to assimilate the effect of neck formation and hence referred to as neck length parameter ΔR. It is analogous to the one used in Scission point model [60] and saddle point model [61] for the calculation of evaporation residue and fission fragment cross-section. Besides this, it also helps to define the effective barrier lowering parameter ΔV_B and aided to deduce the time scale of fragments. The barrier lowering for each ℓ is defined as the difference between the actual barrier used $V(R_a, \ell)$ decided by first turning point R_a and the calculated barrier height $V_B(\ell)$ as $\Delta V_B(\ell) = V(R_a,\ell) - V_B(\ell)$

For the assessment of reaction time, total kinetic energy (TKE) of decaying fragments resulting from the Coulomb repulsion calculated at $R=R_b$ is given as

$$TKE = e^2 Z_1 Z_2 / R_b \tag{2.58}$$

where e^2 =1.44 MeV fm, Z_i (i=1,2) are the atomic numbers of the two outgoing fragments. The TKE is used to assess the velocity of fission fragments as a function of atomic number, which is determined using the semi-statistical approach of Wilkins and collaborators [62–64] as

$$V(Z_2, A_2) = (2TKE/[A_2(1 + A_2/A_1)])^{1/2} \tag{2.59}$$

Using Eqs. (2.58) and (2.59), the time scale of fission/light charged particles is evaluated as

$$\tau = R_b / V(Z_2, A_2) \tag{2.60}$$

2.6 Decay Cross sections

Once the preformation probability P_0 and the penetration probability P are determined, the decay cross-sections within the DCM are obtained using the expression

$$\sigma(A_1, A_2) = \frac{\pi}{k^2} \sum_{\ell_{min}}^{\ell_{max}} (2\ell + 1) P_0 P;\ k = \sqrt{\frac{2\mu E_{c.m}}{\hbar^2}} \tag{2.61}$$

with μ as the reduced mass and $E_{c.m.}$ the center of mass energy that is used to calculate the temperature of excited compound system as

$$E^*_{CN} = E_{c.m} + Q_{in} = \frac{1}{a} A_{CN} T^2 - T \tag{2.62}$$

having level density parameter 'a' = 9-11. Q_{in} = B_1+B_2-B_{CN}, where B_i as the binding energies.

The cross-sections for the compound nucleus process such as evaporation residue ($A_2 \leq 4$)and fusion-fission (A_{ff} ($A_{CN}/2$) $\pm$ 20) are determined using the expression

$$\sigma_{ER} = \sum_{A=1}^{4or5} \sigma(A_1, A_2) \tag{2.63}$$

and

$$\sigma_{ff} = 2 \sum_{A_{CN}/2-20}^{A_{CN}/2} \sigma(A_1, A_2) \tag{2.64}$$

In the case of incomplete fusion process, the evaporation residues emitted from the composite system are determined using the same formula as given Eq. (2.63). But, the $E_{c.m.}$ (= $\frac{A_T}{A_{CN}} \times E_{lab}$) used in the expression is obtained by normalizing the incident beam energy E_{lab} carried away by a new projectile after the break up process as

$$E^{ICF}_{beam} = \frac{E_{lab}}{A} * A^{ICF}, \tag{2.65}$$

where E_{lab}/A is the original beam energy per nucleon with which the initial projectile is expected to strike the target nucleus, and E^{ICF}_{beam} is the fraction of energy carried away by new projectile (A^{ICF}) after the breakup process [65]. The flow chart of

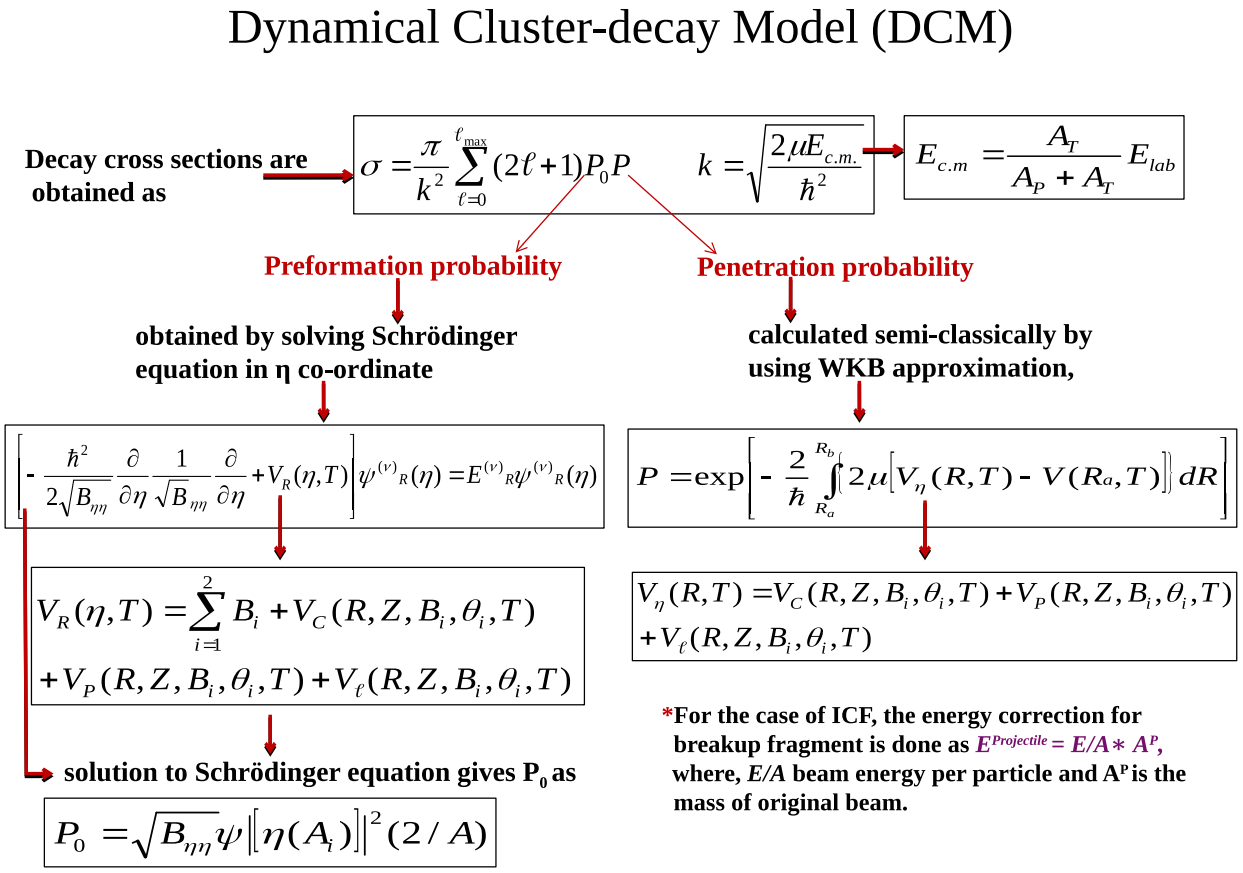

Figure 2.3: Flow chart of dynamical cluster decay model.

dynamical cluster decay model is illustrated in Fig 2.3

Using these methodologies, the calculations are done for a number of heavy ion induced reactions. The results obtained are discussed in the subsequent chapters.

Bibliography

[1] C. Y. Wong, Phys. Rev. Lett. **31**, 766 (1973).

[2] N. Rowley and K. Hagino Phys. Rev. C **91**, 044617 (2017).

[3] N. W. Lwin, N. N. Htike and K. Hagino Phys. Rev. C **95**, 064601 (2017).

[4] R. Kumar, M. Bansal, S. K. Arun, and R. K. Gupta, Phys. Rev. C **80**, 034618 (2009).

[5] J. Blocki, J. Randrup, W. J. Swiatecki, and C. F. Tsang, Ann. Phys. (N.Y.) **105**, 427 (1977).

[6] D. Vautherin and D. M. Brink, Phys. Rev. C **5**, 626 (1972).

[7] R. K. Gupta, R. Kumar, N. K. Dhiman, M. Balasubraniam, W. Scheid, and C. Beck, Phys. Rev. C **68**, 014610 (2003).

[8] M. Balasubraniam, R. Kumar, R. K. Gupta, C. Beck, and W. Scheid, J. Phys. G **29**, 2703 (2003).

[9] B. B. Singh, M. K. Sharma, and R. K. Gupta, Phys. Rev. C **77**, 054613 (2008).

[10] M. K. Sharma, G. Sawhney, R. K. Gupta, and W. Greiner, J. Phys. G: Nucl. Part. Phys. **38**, 105101 (2011).

[11] R. K. Gupta, M. Balasubramaniam, R. Kumar, D. Singh, C. Beck, and W. Greiner, Phys. Rev. C **71**, 014601 (2005).

[12] K. Sandhu, M. K. Sharma, and R. K. Gupta, Phys. Rev. C **85**, 024604 (2012); Rajni, R. Kumar, and M. K. Sharma, Phys. Rev C **90**, 044604 (2014)

[13] I. Sharma, R. Kumar and M. K. Sharma, Eur. Phys. J. A **53**, 140 (2017).

[14] M. Kaur, R. Kumar, and M. K. Sharma, Phys. Rev. C **85**, 014609 (2012).

[15] J. Maruhn and W. Greiner, Phys. Rev. Lett. **32**, 548 (1974).

[16] R. K. Gupta, W. Scheid and W. Greiner, Phys. Rev. Lett. **35**, 353 (1975).

[17] S. Yamaji, W. Scheid, H. J. Fink and W. Greiner, Z. Phys. A **278**, 69 (1976); S. Yamaji, W. Scheid, H. J. Fink and W. Greiner, J. Phys. G: Nucl. Phys. **2**, L189 (1976); S. Yamaji, K. H. Ziegenhain, H. J. Fink, W. Greiner and W. Scheid, J. Phys. G: Nucl. Phys. **3**, 1283 (1977).

[18] A. Săndulescu, R. K. Gupta, W. Scheid and W. Greiner, Phys. Lett. **60B**, 225 (1976); R. K. Gupta, A. Săndulescu and W. Greiner, Phys. Lett. **67B**, 257 (1977); Rev. Roum. Phys. **23**, 51 (1978).

[19] R. K. Gupta, A. Săndulescu and W. Greiner, Z. Naturforsch. **32a**, 704 (1977); R. K. Gupta, Z. Physik. A **281**, 159 (1977).

[20] R. K. Gupta, C. Pirvulescu, A. Săndulescu and W. Greiner, Z. Phys. A **283**, 217 (1977); Sovt. J. Nucl. Phys. **28**, 160 (1978); A. Săndulescu, H. J. Lustig, J. Hahn, and W. Greiner, J. Phys. G: Nucl. Phys. **4**, L279 (1978).

[21] H. J. Fink and W. Greiner and R. K. Gupta and S. Liran and J. H. Maruhn and W. Scheid and O. Zohni, in Proceedings of Int. Conf. on Reaction between Complex Nuclei, Nashville, **21**, (Amsterdam: North Holland), pages 2 (1974).

[22] R. K. Gupta, IANCAS Bull. (India), **6**, 2 (1990).

[23] K. Alder and A. Winther, Nucl. Phys. A **132**, 1-4 (1969).

[24] D. L. Hill and J. A. Wheeler, Phys. Rev. **89**, 1102 (1953); T. D. Thomas, Phys. Rev. **116**, 703 (1959).

[25] M. Beckerman, J. Ball, H. Enge, M. Salomaa, A. Sperduto, S. Gazes, A. DiRienzo, and J. D. Molitoris, Phys. Rev. C **23**, 1581 (1981).

[26] G. Royer and J. Mignen, J. Phys. G: Nucl. Part. Phys. **18**, 1781 (1992).

[27] R. K. Gupta, M. Balasubramaniam, R. Kumar, N. Singh, M. Manhas and W. Greiner, J. Phys. G: Nucl. Part. Phys. **31**, 631 (2005).

[28] M. Münchow, D. Hahn and W. Scheid, Nucl. Phys. A **388**, 381 (1982).

[29] M. J. Rhoades-Brown, V. E. Oberacker, M. Seiwert and W. Greiner, Z. Phys. A **310**, 287 (1983)

[30] N. Cindro and D. Pocanic, J. Phys. G: Nucl. Part. Phys. **6**, 359-366 (1980).

[31] R. Aroumougame, N. Malhotra, S. S. Malik, and R. K. Gupta, Phys. Rev. C **35**, 3 (1987).

[32] R. K. Gupta, N. Singh, and M. Manhas, Phys. Rev. C **70**, 034608 (2004).

[33] W. Myers and W. J. Swiatecki, Nucl. Phys. **81**, 1 (1966).

[34] I. Dutt and R. K. Puri, Phys. Rev. C **81**, 044615 (2010).

[35] E. Chabanat, R. Bonche, R. Haensel, J. Meyer, R. Schaeffer, Nucl. Phys. A **635**, 231-256 (1998).

[36] L. W. Chen, C. M. Ko, B. A. Li, and J. Xu, Phys. Rev. C **82**, 024321 (2010).

[37] B. K. Agrawal, S. K. Dhiman, and R. Kumar, Phys. Rev. C **73**, 034319 (2006).

[38] A. W. Steiner, M. Prakash, J. M. Lattimer, and P. J. Ellis, Phys. Rep. **411**, 325 (2005).

[39] P. A. M. Guichon, H. H. Matevosyan, N. Sandulescu, and A. W. Thomas, Nucl. Phys. A **722**, 1 (2006).

[40] L. G. Cao, U. Lombardo, C. W. Shen, and N. Van Giai, Phys. Rev. C **73**, 014313 (2006).

[41] B. K. Agrawal, S. Shlomo, and V. K. Au, Phys. Rev. C **72**, 014310 (2005).

[42] M. Rashdan, Mod. Phys. Lett. A **15**, 1287 (2000).

[43] F. Tondeur, M. Brack, M. Farine, and J. M. Pearson, Nucl. Phys. A **420**, 297 (1984).

[44] M. Dutra, O. Lourenço, J. S. Sá Martins, A. Delfino, J. R. Stone, P. D. Stevenson, Phys. Rev. C **85**, 035201 (2012).

[45] M. Brack, C. Guet, H.-B. H åkansson, Phys. Rep. **123**, 275 (1985).

[46] J. Bartel, K. Bencheikh, Eur. Phys. J. A **53**, 179 (2002).

[47] P. Chattopadhyay and Raj K. Gupta **30**, 1191 (1984).

[48] L. R. B. Elton, *Nuclear Sizes* (Oxford University Press, London), (1961).

[49] H. de Vries, C. W. de Jager, and C. de Vries, At. Data Nucl. Data Tables **36**, 495 (1987).

[50] S. Shlomo and J. B. Natowitz, Phys. Rev. C **44**, 2878 (1991).

[51] V. M. Strutinsky, Nucl. Phys. A **95**, 420 (1967).

[52] N. J. Davidson, S. S. Hsiao, J. Markram, H. G. Miller, and Y. Tzeng, Nucl. Phys. A **570**, 61c (1994).

[53] P. A. Seeger, Nucl. Phys. **25**, 1 (1961).

[54] G. Audi and A. H. Wapstra, Nucl. Phys. A **595**, 4 (1995).

[55] P. Möller, J. R. Nix, W. D. Myers, and W. J. Swiatecki, At. Data Nucl. Data Tables **59**, 185 (1995).

[56] M. Balasubraniam, R. Kumar, R. K. Gupta, C. Beck, and W. Scheid, J. Phys. G 29, 2703 (2003).

[57] H. Kröger and W. Scheid, J. Phys. G **6**, L85 (1980).

[58] G. Wentzel, Z. Phys. **38**, 518 (1926); H. A. Kramers, Z. Phys. **39**, 828 (1926); L. Brillouin, Comptes Rendus de Academie des Sciences **183**, 24 (1926).

[59] M. K. Sharma, R. K. Gupta and W. Scheid, J. Phys. G: Nucl. Part. Phys. **26**, L45 (2000).

[60] T. Matsuse, C. Beck, R. Nouicer, and D. Mahboub, Phys. Rev. C **55**, 1380 (1997).

[61] S. J. Sanders, Phys. Rev. C **44**, 2676 (1991).

[62] J. L. Rodriguez-Sanchez *et. al*, Phys. Rev. C **91**, 064616 (2015).

[63] B. D. Wilkins, E. P. Steinberg, and R. R. Chasman, Phys. Rev. C **14**, 1832 (1976).

[64] M. Caamañ*o et. al*, Phys. Rev. C **88**, 024605 (2013).

[65] G. Kaur, N. Grover, K. Sandhu and M. K. Sharma, Phys. Rev. C **927**, 232-248 (2014).

Chapter 3

Fusion analysis using variety of nuclear potentials

3.1 Introduction

The study of fusion mechanism governed via heavy ion induced reactions is focused around the penetration of collision partners through the Coulomb barrier and the formation of compound nucleus (CN). The barrier penetration is found to be greatly influenced by deformations and orientations of colliding nuclei, which play a vital role to understand the reaction mechanism. The deformed nuclei modify the interaction barrier and enhance the fusion probability as compared to spherical colliding partners. This provides better understanding of low energy phenomena such as fusion enhancement observed at sub barrier energies in medium and heavy mass nuclei. It is always of interest to study this effect in the super heavy mass region. The fusion mechanism of super heavy nuclei is significantly different from the light mass nuclei because of the subsequential increase of Coulomb repulsion between the interacting nuclei. Therefore, actinide target and low Z-projectile from C to Si have been used to produce heavy element isotopes up to Z=112. The super heavy nuclei may be synthesized via cold fusion or hot fusion approaches. For low Z-super heavy systems up to Z=112, cold fusion is preferred. Whereas, for relatively higher

Z-super heavy systems hot fusion seems to provide a better option. In case of hot fusion, the prolate deformed actinide targets prefer to form equatorial configuration and provide a better synthesis option for higher Z-super heavy systems (Z>112) at relatively higher incident energies. When the energy decreases below Coulomb barrier, cold polar configurations play an eminent role. The polar orientations in turn increase the relative separation between colliding nuclei, consequently the interaction barrier height reduces, and the fusion cross-sections show enhancement in the sub barrier region. Thus, the reaction mechanism in case of super heavy nuclei changes drastically across the Coulomb barrier.

In view of above, the reaction mechanism of $^{268}Sg^{*}$ [1, 2] compound nucleus formed in ^{30}Si + ^{238}U reaction is analyzed across the Coulomb barrier by using different theoretical methods such as Wong and ℓ-summed Wong model. As the fusion cross-section is sensitive to interaction barrier (particularly at near and sub barrier barrier region), so different nuclear potentials have been used to analyze the fusion excitation data in heavy ion reactions. In this chapter, nuclear potential obtained via Skyrme Energy Density Formalism (SEDF) [3,4] are used to investigate the dynamics of this reaction. In SEDF approach, the Skyrme parameters have been defined by different authors in order to explain the surface as well as bulk properties of nuclei and thus provide several sets of Skyrme forces [5–7]. Some, modifications in the Skyrme Hamiltonian have been done, and additional terms were introduced in the Hamiltonian density of Skyrme interaction as per Ref. [8]. The experimental data of normal and isospin rich nuclei were used to fit the parameters of proposed GSkI, GSkII, SSk [8] Skyrme forces. Thus, these Skyrme forces are found to be more sensitive towards the isospin effect and neutron-proton asymmetry as compared to old forces like SIII, SkM, Ska [9] etc. The extensive study on various Skyrme forces [10] reported that among 240 Skyrme forces only 16 are shown to satisfy macroscopic constraints applied on them. From the set of 16 Skyrme forces, we choose newly developed GSkI, KDE0v1 [11] forces along with old form of SkT1 [12]

force to study their comparative behavior with SIII and SSk Skyrme forces.

Using different Skyrme forces in the framework of Wong and ℓ-summed Wong model [13], the fusion process of ^{30}Si + ^{238}U reaction is examined across the barrier. The cross-sections in Wong formula [14] underestimate the experimental data at low energies while at higher energies, the calculations overestimate the available data. The underestimation of data is resolved by opting appropriate Skyrme force(s) while the overestimation of data is addressed using ℓ-summed Wong model. It is observed that SSk (or GSkI force of similar barrier characteristics) along with cold orientation approach gives reasonable addressal of experimental data for the fusion of super heavy nucleus ^{268}Sg*. Besides this, the calculations are extended for the set of reactions comprising of different projectiles such as ^{12}C, ^{16}O, ^{28}Si, and ^{48}Ca interacting with ^{154}Sm target nucleus forming the compound nuclei in the mass range A_{CN}=166-208. The calculations are carried out using the ℓ-summed Wong model wherein the effect of SIII and GSkI Skyrme forces (with extreme barrier heights) is examined and the results are compared with the phenomenological potential mod Prox 88. The impact of cold optimum orientation is also evaluated in the sub barrier fusion dynamics of chosen reactions. Additionally, the influence of different projectile beams on the corresponding barrier profile of interaction potentials is analyzed, which suggests that GSkI force is suitable for the heavier symmetric reactions. The observations from above analysis suggest that deformation, orientations and different nuclear potentials induce consistent barrier modification effects, which in turn helps to describe the fusion mechanism of chosen reactions across the Coulomb barrier. The calculations and results are discussed in section 3.2 and the conclusions drawn are described in section 3.3.

3.2 Calculations and results

In this work, the role of different Skyrme potentials and the surface effects of colliding nuclei are exercised in the vicinity of Coulomb barrier. The analysis is divided

into two subsections. In section A, the fusion of ^{30}Si + ^{238}U reaction is examined using SIII, GSkI, KDE0v1, SKT1 and SSk Skyrme forces by including deformations and orientation effects within the Wong and ℓ-summed Wong model. Based upon the performance of Skyrme interactions, the fusion cross sections are predicted at extreme energies by using the ℓ-summed Wong approach. In section B, the effect of mass, energy, deformations and orientation of the nuclei are analyzed in reference to the dynamics of heavy-ion induced reactions spread across the Coulomb barrier. The Skyrme forces with extreme barrier characterization i.e SIII and GSkI are used to examine their corresponding impact on the fusion dynamics of ^{12}C+^{154}Sm, ^{16}O+^{154}Sm, ^{28}Si+^{154}Sm, ^{48}Ca+^{154}Sm reactions. The results obtained for these Skyrme forces are compared with the proximity potential mod Prox 88. Besides this, the role of different projectile beams on corresponding barrier profile of interaction potentials is analyzed.

3.2.1 Fusion analysis of ^{268}Sg* superheavy nucleus

Firstly using the Wong formula, the barrier profile of ^{30}Si + ^{238}U reaction has been studied with chosen Skyrme forces at temperature T=0 MeV. Fig. 3.1 shows the scattering potential as a function of separation distance R(fm), calculated for deformed choice of nuclei using SkTI, SSk, GSkI, KDE0v1 and SIII forces. The Fig. 3.1 clearly shows that SSk has the lowest barrier height while KDE0v1, SIII and SkT1 forces (having similar barrier characteristics) possess the highest barrier. Here, one may notice that the barrier profile of GSkI force is quite similar to SSk force. Among the selected forces, the role of SIII and GSkI Skyrme forces was analyzed recently [15], therefore in this work the calculations are carried out for KDE0v1, SkT1 and SSk forces so as to cover the wide range of barrier distributions. It is pertinent to mention that Skyrme forces with different barrier characteristics impart relevant modifications in the barrier profile which in turn influences the fusion probability to a significant extent.

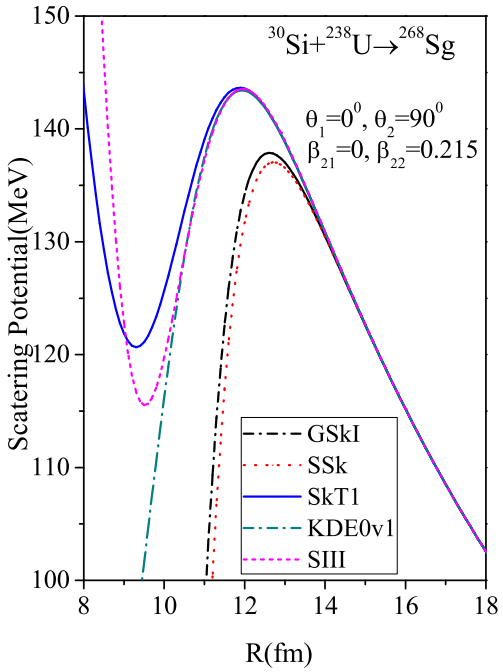

Figure 3.1: Scattering potential (MeV) as a function of separation distance R (fm) calculated for deformed choice of colliding nuclei at T=0 MeV, and ℓ=0 $\hbar$ using different sets of Skyrme interactions within the Wong formula.

The fusion cross-sections of ^{30}Si +^{238}U reaction are calculated using KDE0v1, SSk and SkT1 forces within the Wong formula. The calculations are compared with experimental data [2] and the results are shown in Fig. 3.2. This figure depicts that SkT1 and KDE0v1 forces give decent agreement with observed data at higher barrier region but at sub-barrier region, both the forces underestimate the available data. However, SSk force shows opposite behavior with respect to KDE0v1 and SkT1 forces. The SSk force is found to give comparatively better results at sub-barrier region, but it overestimates the data at higher energies. It is to be noticed that these calculations are done with spherical choice of nuclei. Further, the calculations incorporate static quadrupole deformations of projectile(^{30}Si) and target(^{238}U), taken from theoretical prediction of Moller *et al.* [16], to analyze their effect on the fusion cross-sections.

Here, Fig. 3.3 shows the comparison of experimental data with calculated fusion cross sections using SSk, SkT1 and KDE0v1 forces and including the deformations

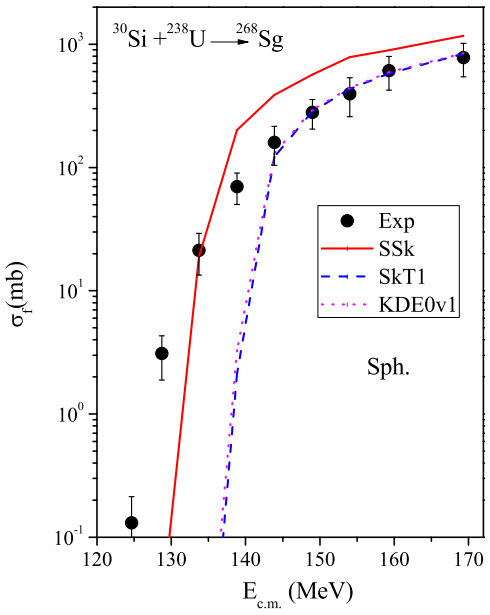

Figure 3.2: Fusion cross-sections calculated for spherical choice of nuclei using SSk, SkT1 and KDE0v1 forces within Wong model are compared with experimental data of $^{30}Si + ^{238}U$ reaction [2].

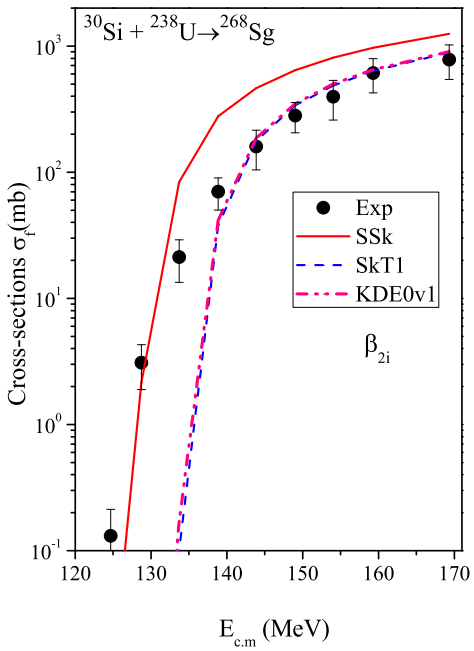

Figure 3.3: Same as Fig. 3.2 but for β_2 deformed nuclei.

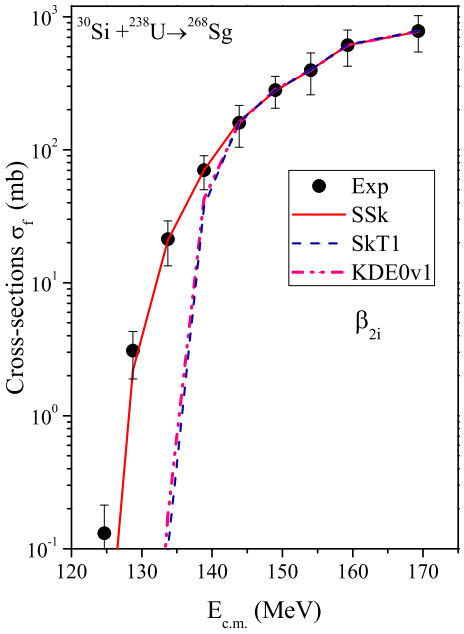

Figure 3.4: Fusion cross-sections for deformed nuclei are calculated with chosen Skyrme forces using ℓ-summed Wong formula.

effects. One may observe that the cross-sections calculated with SSk force show small improvement after inclusion of deformations at the sub barrier region. However, no significant change is noticed for SkT1 and KDE0v1 forces, particularly at below barrier region. The SSk force overestimates the experimental data at higher energy region, and this issue is resolved by replacing Wong formula with ℓ-summed Wong model.

In case of Wong formula, the cross-sections are obtained by summing over-all values of angular momentum, as a result the calculated values overestimate the experimental data. On the other hand, ℓ-summed Wong formula restricts the summation up to fixed values of angular momentum (as per ref. [17]) and provide better agreement with experimental data at above barrier region. This is evident from Fig. 3.3 and Fig. 3.4. In Fig. 3.4, the fusion excitation functions are calculated as a function of $E_{c.m.}$, within the ℓ-summed Wong formula by using selected Skyrme forces i.e. SSk, SkT1 and KDE0v1 forces. Fig. 3.4 illustrates that within the ℓ-summed

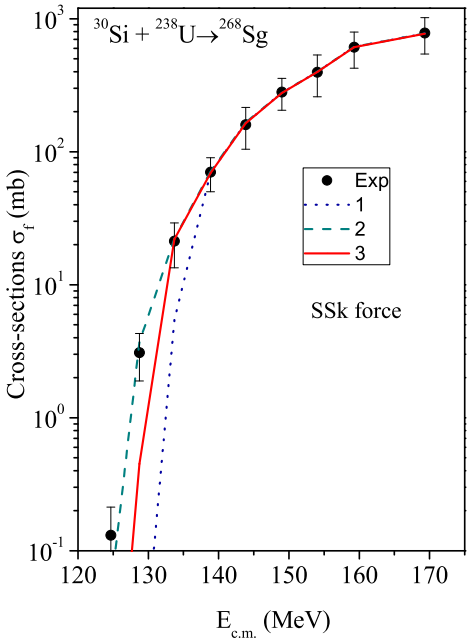

Figure 3.5: Fusion cross-sections calculated for 1. Hot optimum orientations 2. Cold optimum orientations and 3. taking all orientations from 0^0-90^0 with SSk force using ℓ-summed Wong formula.

approach, all the chosen Skyrme forces perform better at higher energies. Even, the Skyrme forces which differ in several MeV at the barrier lead to almost similar results with little variation in ℓ_{max} values. This is because at higher energies i.e. $E_{c.m.} > V_B$, the centrifugal potential starts dominating over the nuclear potential. However, at sub barrier energies, SkT1 and KDE0v1 forces do not fit the available data while only SSk force gives relatively better agreement with experimental data. This means that SSk force (and GSkI similar to SSk force) being sensitive to isospin effect, performs better over entire energy range with in the ℓ-summed Wong model.

Using SSk force, an attempt is made to study the effect of different configurations of colliding nuclei [18] within the ℓ-summed Wong approach. The excitation functions are calculated over a wide range of $E_{c.m.}$ with β_2 deformed dynamical configuration at optimum orientations. The calculations are compared with observed data and shown in Fig. 3.5. The Fig. 3.5 depicts that cross-sections calculated using

Table 3.1: The predictions of fusion cross section for ^{30}Si $+^{238}$U reaction across the Coulomb barrier is done using ℓ-summed Wong approach. Last two $E_{c.m.}$ values correspond to sub barrier energies.

		$\ell_{max}\hbar$		σ (mb)	
S.No.	$E_{c.m.}$	SSk	GSkI	SSk	GSkI
1	174.32	78	78	877	877.369
2	179.32	83	83	964.564	964.564
3	184.32	89	89	1076.657	1076.66
4	189.32	95	95	1192.905	1192.904
5	114.66	33	26	2.7×10^{-8}	5.9×10^{-9}
6	119.66	39	34	3.88×10^{-5}	8.77×10^{-6}

cold polar configuration at sub barrier region give better agreement with experimental data [2] as compared to the hot equatorial configuration. It might be because the polar orientations correspond to large interaction radius and lowest barrier. However, the cross-sections calculated over θ- integration lie in between cold and hot orientation. It suggests that cold polar orientations perform better at sub-barrier regime. However, the orientation degree of freedom does not play important role at higher energies. This observation is in agreement with the earlier work carried using the dynamical cluster decay model [19].

After the successful addressal of experimental data, the fusion cross sections are predicted at extreme energies using ℓ-summed Wong approach. In ℓ-summed Wong model, the fusion cross sections at two center of mass energies below the barrier *i.e.* $E_{c.m.}$ = 114.6 and 119.6 MeV are estimated via cold polar orientation and at four center of mass energies above the barrier *i.e.* $E_{c.m.}$ = 174.32, 179.32, 184.32 and 189.32 MeV by using hot equatorial orientation. These calculations are performed using SSk and GSkI Skyrme forces. The predictions are made by extrapolating the ℓ_{max} values as a function of center of mass energy $E_{c.m.}$ using

the linear polynomial equation *i.e.* ℓ_{max} = -112.69 + 1.0967 $E_{c.m.}$ at above barrier energies. While, at sub barrier energies, the angular momentum values are summed up until the cross sections i.e. σ_f reduces to infinitesimal small value. The calculated cross sections are shown in Table 3.1, which illustrates that both the interactions give nice agreement at higher energies while at deep barrier energies, SSk and GSkI forces show significant difference. At below barrier region, the different Skyrme forces address the quantum mechanical tunnelling in different way, while at above barrier energies the fusion cross section does not depend much on the choice of Skyrme forces. From this analysis, it is concluded that SSk and GSkI forces serve better to address the sub barrier fusion dynamics. However, it is of great interests to examine the relative behavior of Skyrme based potential and the proximity based potential in the vicinity of Coulomb barrier. In view of this, further study is carried out to examine the fusion dynamics of various compound nuclei lying in the different mass region, by using the SIII, GSkI (equivalent to SSk) Skyrme forces along with mod Prox 88 potential in the framework of ℓ-summed Wong model. The results are discussed in the next sub section.

3.2.2 Fusion analysis of compound nuclei A_{CN}=166-202

In this analysis, the role of deformation and the projectile-target mass/charge asymmetry is assessed in view of compound nucleus formation at near Coulomb barrier energies. Also, the effect of orientation and nucleus-nucleus potentials on the fusion process is widely studied at energies around the Coulomb barrier. The theoretical calculations are performed by using the ℓ-summed Wong formalism for different fusion reactions i.e. ^{12}C,^{16}O,^{28}Si,^{48}Ca+^{154}Sm [20–23]. In these reactions, the mass of projectile nucleus is varied while the target ^{154}Sm remains the same. For the fusion process, the ion-ion potential plays an important role in explaining the fusion hindrance phenomena [24] by influencing the tunneling probability of interacting nuclei. Therefore, SIII and GSkI forces along with the modified proximity potential

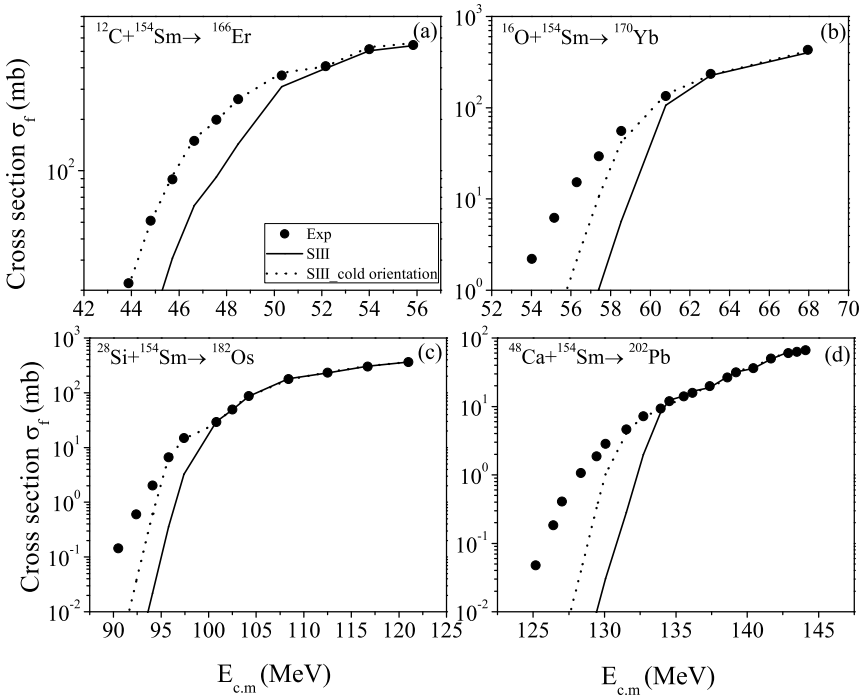

Figure 3.6: The fusion cross-section of ^{12}C, ^{16}O, ^{28}Si, ^{48}Ca + ^{154}Sm reactions calculated using the SIII Skyrme force within the extended Wong formalism. The solid line is referred to the calculations done by integrating θ from 0^0 to 90^0, while dotted lines are referred to the calculation obtained using the Cold orientation approach (only for 0^0,180^0).

(mod Prox 88) [25] are used in the study.

Using the ℓ-summed Wong model, the fusion cross sections of ^{12}C+^{154}Sm reaction are calculated in the vicinity of Coulomb barrier by using the SIII Skyrme force and the results are compared with the experimental data as shown in Fig. 3.6(a) (solid line). The result depicts that the fusion process is hindered at sub barrier energies. These calculations are done by including the quadrupole deformations of the interacting nuclei and the orientation angles are integrated from θ_i=0^0 to 90^0. From Fig. 3.6(b), it is clear that as the mass of projectile nucleus increases from ^{12}C to ^{16}O, the impact of fusion hindrance persists at lower incident energies, and it's magnitude increases with an increase in the mass (charge) of the projectile nu-

cleus. The fusion hindrance becomes more pronounced while replacing ^{16}O with ^{28}Si and ^{48}Ca nuclei (as a projectile), as evident from Figs. 3.6 (c, d). The increase in fusion hindrance indicates that within the SIII force, the asymmetric channels are relatively more preferable for the fusion process as compared to the symmetric one. The impact of the symmetric channel at sub barrier energies is directly related to the Coulomb factor Z_1Z_2, which simultaneously affects the barrier profile and the tunneling probability of the interacting nuclei. Hence, to overcome the inhibition of sub barrier fusion process, the cold orientation approach (θ_i=0^0, 180^0) is applied with the SIII Skyrme force, as shown in Fig. 3.6 (dotted lines). Since in sub barrier region, the colliding nuclei possess lower kinetic energy and hence have lower velocities; they may get enough time to orient themselves in order to enhance the penetration probability as well as cross-sectional yield [26]. By using the cold orientation approach, fusion cross-sections are improved to some extent, but the comparison with experimental data is still bad at the lowest energies. In view of this SIII Skyrme force is replaced by generalized GSkI force for further calculations. Further, it is of interest to compare the influence of nucleus-nucleus potentials having different forms, as one may get a better picture of the nuclear interactions in terms of mass (charge), and orientation of the reacting nuclei. So, the proximity based mod Prox 88 potential is used in conjunction with the GSkI force as this potential performs better [25]. Using the two different forms of nuclear potentials (i.e. GSkI and mod Prox 88), the cross-sections of ^{12}C, ^{16}O, ^{28}Si, and ^{48}Ca +^{154}Sm reactions are calculated within the framework of extended Wong model. The results are shown in Fig. 3.7.

Fig. 3.7 shows the comparison of fusion cross-sections calculated using the GSkI Skyrme force and mod Prox 88 proximity potential for the reactions under study. It is clear from this figure that one gets better agreement with the experimental data for ^{12}C+^{154}Sm reaction while opting GSkI and mod Prox 88 potential. However, the fusion hindrance in ^{16}O induced reaction is still observed for the case of GSkI

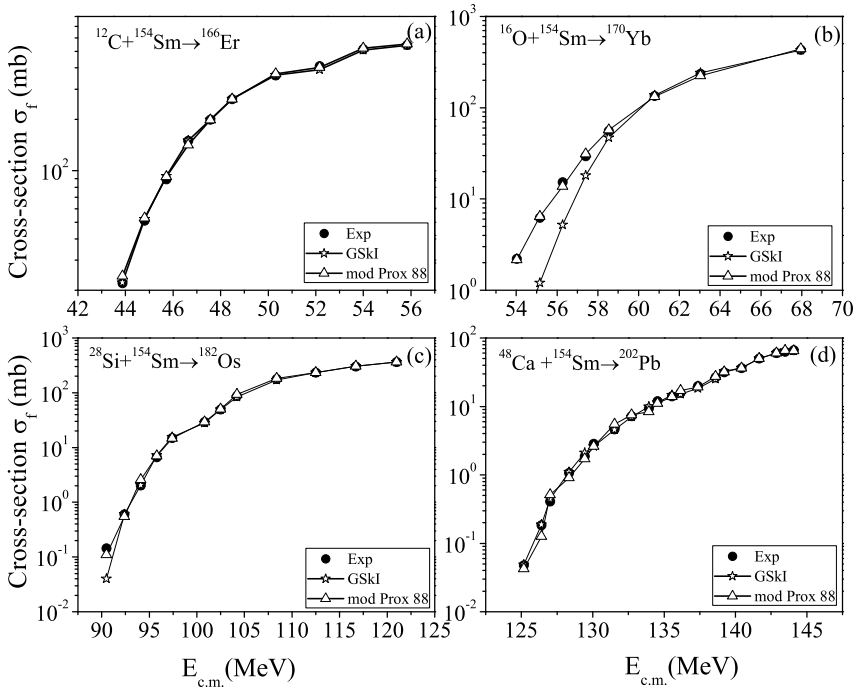

Figure 3.7: The fusion excitation function of ^{12}C+^{154}Sm, ^{16}O+^{154}Sm,^{28}Si+^{154}Sm and ^{48}Ca+^{154}Sm reactions calculated using the GSkI Skyrme force and mod Prox 88 proximity potential are compared with their respective experimental data [20–23].

Skyrme force, which suggests that this reaction requires more barrier alteration as compared to the other considered reactions. The overall comparison with the experimental data implies that the interaction potentials play an important role in controlling the quantum mechanical tunnelling process.

Further, the behavior of different interaction potentials is analyzed in terms of scattering potential V(R), plotted in Fig. 3.8. The figure depicts that the SIII Skyrme force, which could not reproduce the fusion cross-sections for any of the considered reactions, has the highest fusion barrier V_B (= V_C+V_P) in comparison to the GSkI and mod Prox 88 potential. The significant variation in the barrier heights corresponding to the SIII and GSkI Skyrme forces are mainly due to the extension of density-dependent term included in the Skyrme Hamiltonian for the case of GSkI Skyrme force, which possesses additional Skyrme parameters that leads to lowering

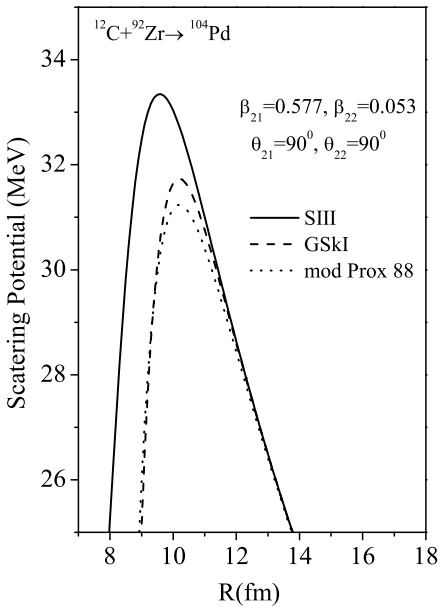

Figure 3.8: Scattering potential V(R) for ^{12}C+^{154}Sm reaction is obtained using SIII [9], GSkI [8] Skyrme forces and mod Prox 88 [25] potential.

of barrier height. However, mod Prox 88 potential, which has modified parameters for surface coefficient term reflects lower barrier in comparison to the chosen Skyrme forces. It is evident from above analysis that, the performance of these interaction potentials strongly depends upon their barrier characteristics. Keeping this in mind, the barrier profile of interaction potentials are further investigated for the different set of reactions under study.

Fig. 3.9 shows the barrier height for the reactions ^{12}C,^{16}O,^{28}Si,^{48}Ca+^{154}Sm calculated using the SIII and GSkI Skyrme forces and mod Prox 88 potential. In Fig. 3.9, it is noticed that the considered reactions exhibit consistent results as discussed in Fig. 3.8 i.e. SIII force has the highest barrier height followed by GSkI Skyrme force and mod Prox 88 potential. For each nuclear potential, the magnitude of barrier height increases with increase in projectile mass (charge), and the mod Prox 88 has the lowest barrier height as compared to the SIII and GSkI forces except for

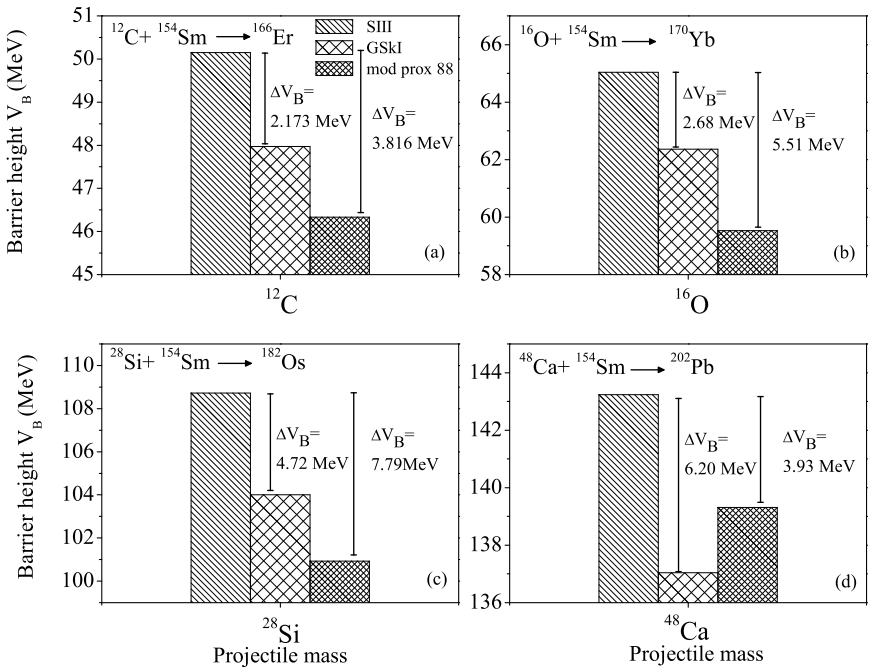

Figure 3.9: Variation in barrier heights of ^{12}C, ^{16}O, ^{28}Si and ^{48}Ca +^{154}Sm reactions calculated using different interaction potentials.

relatively symmetric ^{48}Ca+^{154}Sm reaction. This switching between the behaviors of GSkI and mod Prox 88 potentials for ^{48}Ca induced reaction is probably due to relative symmetric reaction partners. The GSkI force, due to its inbuilt parameters, imparts relatively enhanced barrier lowering effect [8] for the symmetric reaction partners as compared to the asymmetric ones.

Further insight on the performance of GSkI Skyrme force and mod Prox 88 potential is made by extending the study on ^{16}O+^{184}W and ^{48}Ca+^{154}Sm reactions forming the same compound nucleus, ^{202}Pb as shown in Fig. 3.10. This figure clearly illustrates that for the asymmetric reaction i.e. ^{16}O+^{184}W, the GSkI Skyrme force has the higher barrier as compare to mod Prox 88 potential while for the relatively symmetric reaction i.e. ^{48}Ca+^{154}Sm, the barrier is lower.

This implies that the density-dependent GSkI Skyrme force behaves better for more symmetric and neutron-rich cases as compared to the asymmetric ones. Fur-

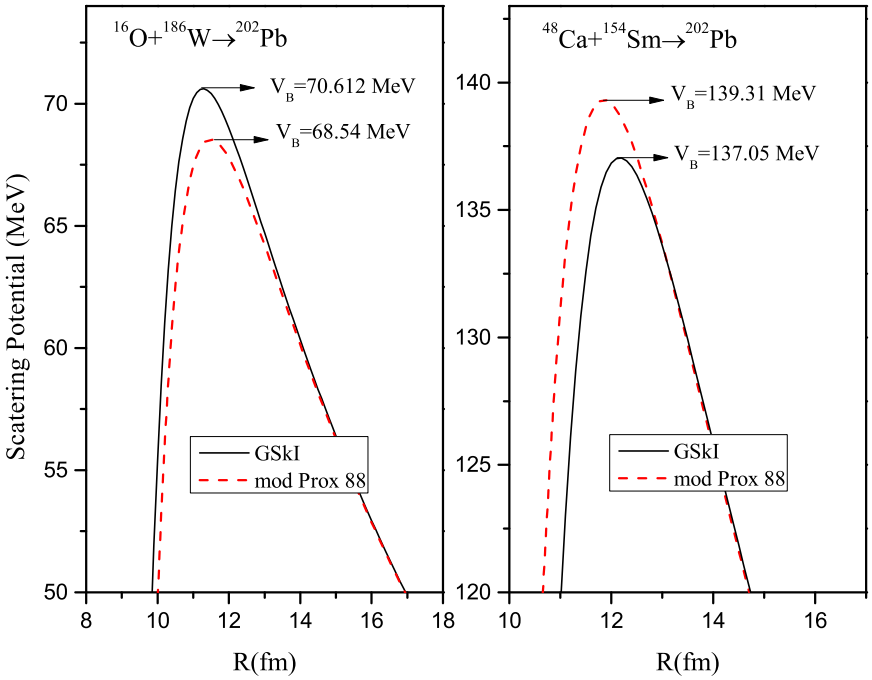

Figure 3.10: Comparison of the barrier heights of ^{16}O + ^{184}W and ^{48}Ca +^{154}Sm reactions forming the same compound system ^{202}Pb determined using the GSkI Skyrme force and mod Prox 88 potential.

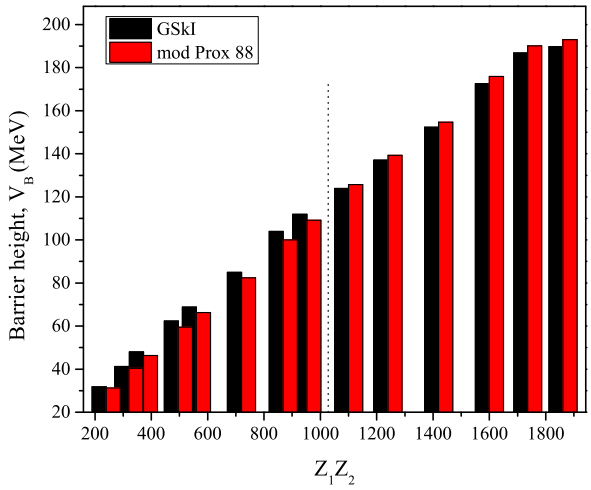

Figure 3.11: Variation in the barrier heights (V_B) of GSkI Skyrme force and mod Prox 88 potential with respect to Z_1Z_2.

ther, a generalized study on the barrier profile of GSkI force and mod Prox 88 potential has been done by analyzing various reactions with Z_1Z_2 varying from 240 to 1900 as shown in Fig. 3.11. It is clear from this figure that the GSkI force switches its barrier characteristics as Z_1Z_2 crosses 1000, i.e. for the symmetric, heavier and neutron-rich nuclei it gives lower barrier height in comparison to the mod Prox 88 potential. From above it can be concluded that the GSkI Skyrme force is more suitable to handle the fusion process of heavier symmetric reactions.

3.3 Conclusions

The fusion cross sections of ^{30}Si $+^{238}$U reaction is examined using Wong and ℓ-summed Wong formula. Within these approaches, the behavior of different Skyrme interactions is tested at energies across the Coulomb barrier. The choice of different Skyrme forces leads to different barrier profile and by choosing appropriate Skyrme interaction in conjunction with Wong formula, one finds better addressal of observed fusion data. It has been observed that SSk and GSkI forces (having similar barrier characteristics) perform better at sub barrier energies, however, the above barrier data is adequately addressed by SkT1, SIII and KDE0v1 Skyrme forces. The SSk force due to lower barrier distribution overestimate the data at higher energies which is accounted within ℓ-summed Wong approach. The effect of optimum orientations across the barrier is also studied using ℓ-summed Wong formula. Observation shows that cold polar configuration is more favorable at sub barrier energies as compared to hot equatorial configuration. Along with this, fusion cross-sections are predicted at extreme energies within the framework of ℓ-summed Wong criteria. At above barrier energies, the predicted cross sections almost overlap for different choices of Skyrme forces, whereas significant difference is observed at sub barrier region. These predictions suggest that different interactions modify the quantum mechanical tunnelling at below barrier energies in different ways.

Besides this, further analysis has been carried out for different set of nuclear reactions

varying from lighter to heavy mass range. The work focuses on the influence of mass (charge), energy, deformation and orientation effect of the interacting nuclei, on the fusion dynamics of heavy-ion induced reactions. The role of different nuclear potentials is also worked out. The study shows that the fusion hindrance in below barrier region persists for SIII Skyrme force and it increases consistently with an increase in the projectile mass (charge). The hindrance to fusion path is treated to some extent by employing the cold orientation approach. On switching the choice of potential from SIII to generalized GSkI Skyrme force and proximity type mod Prox 88, the comparison with experimental data improves significantly. Also, the barrier characteristics of above mentioned interaction potentials demonstrate the effect of incoming channel, which on the other hand, govern the cross-sectional yield significantly. Hence it is concluded that the SIII Skyrme force could not address the experimental data for any of the considered reactions whereas the GSkI force is preferred for heavier symmetric reactions in comparison to the mod Prox 88 potential. The GSkI Skyrme force and mod Prox 88 potential address the fusion hindrance process significantly, because these potentials are modified in such a way that they offer lower barrier height, which consequently helps in enhancing the fusion probability.

After examine the behavior of structural effects and different Skyrme interactions in the fusion process of heavy ion nuclear reactions, further efforts are made to address the fusion and decay process together for the comprehensive analysis of reaction dynamics of intermediate mass nuclei. The results are discussed in subsequent chapters.

Bibliography

[1] K. Nishio *et al.*, Eur. Phys. J. A. **29**, 281 (2006).

[2] K. Nishio, H. Ikezoe, I. Nishinaka, S. Mitsuoka, K. Hirose, T. Ohtsuki, Y. Watanabe, Y. Aritomo and S. Hofmann, Phys. Rev. C **82**, 044604 (2010).

[3] D. Vautherin and D. M. Brink, Phys. Rev. C **5**, 626 (1972).

[4] J. Bartel, K. Bencheikh, Eur. Phys. J. A **53**, 179 (2002).

[5] S. Krewald, V. Klent, J. Speth and A. Faessler, Nucl. Phys. A **281**, 166 (1977).

[6] H. S. Kohler, Nucl. Phys. A **258**, 301 (1976).

[7] H. Krivine, J. Treiner, O. Bohigas, Nucl. Phys. A **336**, 155 (1980).

[8] B. K. Agrawal, S. K. Dhiman, and R. Kumar, Phys. Rev. C **73**, 034319 (2006).

[9] M. Brack, C. Guet and H. B. Hakansson, Phys. Rep. **123**, 275 (1985).

[10] M. Dutra, O. Lourenço, J. S. Sá Martins, and A. Delfino, J. R. Stone, P. D. Stevenson, Phys. Rev. C **85**, 035201 (2012).

[11] B. K Agrawal, S. Shlomo, and V. Kim Au, Phys. Rev. C **72**, 014310 (2005).

[12] F. Tondeur, M. Brack, M. Farine and J. M. Pearson, Nucl. Phys. A **420**, 297 (1984).

[13] R. Kumar, M. Bansal, S. K. Arun and R. K. Gupta, Phys. Rev. C **80**, 034618 (2009).

[14] C. Y. Wong, Phys. Rev. Lett. **31**, 766 (1973).

[15] M. S. Gautam, Rajni and M. K. Sharma, Braz. J. Phys. **46**, 133 (2016).

[16] P. Moller, J. R. Nix, and W. D. Swiatecki, At. Data Nucl. Data Tables **59**, 185 (1995).

[17] M. Beckerman, J.Ball, H. Enge, M. Salomaa, A. Sperduto, S. Gazes, A. DiRienzo, and J. D. Molitoris, Phys. Rev. C **23**, 1581 (1981).

[18] R. K. Gupta, M . Balasubramaniam, R. Kumar, N. Singh, M. Manhas, and W. Griner, J. Phys. G **31**, 631 (2005).

[19] K. Sandhu, M. K. Sharma, and R. K. Gupta, Phys. Rev. C **86**, 064611 (2012).

[20] S. Gil *et al.*, Phys. Rev. C **31**, 1752 (1985).

[21] R. G. Stokstad *et al.*, Phys. Rev. C **21**, 6 (1980).

[22] S. Gil *et al.*, Phys. Rev. Lett. **65**, 25 (1990).

[23] A. M. Stefanini *et al.*, Eur. Phys. J. A **23**, 473-480 (2005).

[24] O. N. Ghodsi and R. Gharaei, Eur. Phys. J. A **48**, 21 (2012).

[25] R. Kumar, and M. K. Sharma, Phys. Rev. C **85**, 054612 (2012).

[26] V. Zagrebaev, A. Karpov, Y. Aritomo, and W. Greiner, Phys. Part. Nuclei **38**, 469-491 (2007).

Chapter 4

Formation and decay dynamics of ^{40,48}Ca+^{96}Zr reactions

In the preceding chapter, the role of various Skyrme interactions along with deformation and optimum orientations of the reacting nuclei were examined in view of fusion process using the Wong and ℓ-summed Wong model. Extending the study for fusion and decay process, ^{136,144}Nd* compound nuclei are examined at energies spread around the Coulomb barrier. The impact of Skyrme interactions and neutron transfer effect are exercised in the sub-barrier region. Different methodologies like Wong, ℓ-summed Wong and dynamical cluster decay model are used for the investigation of fusion and decay processes respectively.

4.1 Introduction

An extensive study on heavy ion induced reactions have been carried out in the last few decades, which explored various aspects of reaction dynamics and many more still remain unsolved. For instance, the fusion process at above barrier energies would be understood on the basis of incident energy and angular momentum effects. But, the complexities in the fusion dynamics at sub-barrier region keep challenging the scientific community. Several difficulties were confronted on both experimental

and theoretical front to investigate the anomalies of heavy ion induced reaction dynamics. Numerous attempts have been made to explore the complex dynamics on the basis of quantum tunnelling effect, nuclear deformations and coupling to the vibrational and rotational degree of freedom etc. These efforts were successful in explaining the inconsistency in the fusion process to some extent.

In 1997, Timmer *et al.* [1] observed that couple channel approach describe the barrier distribution and related fusion dynamics of $^{40}Ca + ^{90}Zr$ reaction. However, the authors could not explain the same in heavier reaction, $^{40}Ca + ^{96}Zr$. Although, both the reactions have almost similar deformation effect and Z_1Z_2 factor, but differ significantly in terms of neutron transfer channel effect, which arises due to positive ground state Q values, and hence impart corresponding effect on the dynamics of these reactions. According to Ref [1], up to 8 neutrons can be transferred from ^{96}Zr to ^{40}Ca with positive Q value. But it is not clear, that how many and up to what extent the transfer channels are exactly participating in the fusion of $^{40}Ca + ^{96}Zr$ reaction. Later on, the analysis on $^{40}Ca + ^{96}Zr$ reaction was carried out by Stefanini et al. [2, 3], where the cross sections were explained on the basis of vibration and rotational degrees of freedom. The role of neutron transfer effect is also explored by different theoreticians [4–6] and afterward the effect of deformations along with neutron transfer effect [7] is used to give the possible explanation of enhancement in experimental data. In coupled channel calculations, coupling to multiphonon with one- and two neutron transfer using the Ch-84 calculations could not explain the data at low energies [2]. However, the revised study of $^{40}Ca + ^{96}Zr$ reaction by Esbensen *et al.* [8] showed that the combined effect of surface excitations and nucleon transfer reaction could reproduce the experimental data. Hence it is desirable to explore the effect of transfer channels for the better understanding of fusion dynamics.

Presently, an attempt is made to re-investigate the fusion data of $^{40}Ca + ^{96}Zr$ reaction in comparison to $^{48}Ca + ^{96}Zr$ at energies across the Coulomb barrier i.e. $E_{c.m.}$ = 84.11 - 106.2 MeV. Here, the nuclear deformations, orientations, different

nuclear Skyrme interactions along with neutron transfer channels are taken into consideration. The Skyrme interactions are found to address the phenomena of enhancement by inducing barrier modification effect. Within the different Skyrme potentials, the requirement of n-transfer channels is different and this is what we intend to study in the present work. Here, the Skyrme interactions [9] such as SIII, GSkI, SkT1, SkT2 and SkT3 based upon Skyrme Energy Density Formalism (SEDF) [10] are used, with a motive to test their performance in reaction dynamics. In recent works [11, 12], the GSkI force emerges out as a better choice for the study of different heavy ion reactions, therefore, in reference to this force, the behavior of SIII, SkT1, SkT2 forces is examined in reaction dynamics around the Coulomb barrier. Subsequent to this, the effect of transfer channels is explored using different nuclear potentials calculated using the above mentioned Skyrme forces.

A detailed study of fusion cross section is carried out using the Wong and extended Wong model (ℓ-summed) [13, 14], in which neutron transfer effect is introduced via transmission probability (for details, see Eq. (2.11) of chapter 2). The fusion cross section calculated with SIII, SkT1, SkT2, SkT3 Skyrme forces indicate the presence of fusion hindrance in sub barrier region. Besides this, the GSkI Skyrme force is used, which provides requisite barrier modification and improves the comparison with experimental data significantly. The prevailing discrepancies are resolved by introducing the neutron transfer effect. The calculation shows that with the inclusion of 1n-transfer effect GSkI force reproduces the experimental data nicely, while the SkT1 force persists with the poor result even for 1n-transfer effect.

After the adequate addressal of fusion of $^{40,48}Ca + ^{96}Zr$ reactions, an attempt is made to examine the decay of $^{136,144}Nd^*$ compound systems formed in the above reactions. We aimed to study the decay of these nuclei to examine the possible role of neutron transfer in ^{40}Ca based reaction. A comprehensive study of $^{40,48}Ca + ^{96}Zr$ reactions has been carried out using the dynamical cluster-decay model (DCM) [15–18]. The role of different potentials is explored here as well with

GSkI and SkT1 Skyrme forces (i.e the forces with extreme barrier characteristics). Besides addressing the experimental data, the DCM also provides structural information of the decaying fragments. The observation notifies that symmetric fission window changes from narrow to broad as we move from neutron deficient ($^{136}Nd^*$) nucleus to neutron rich case ($^{144}Nd^*$). Also, in consistent to Wong calculations, GSkI force seems to provide a favorable choice as it requires lesser barrier modification as compare to SkT1 force or equivalently other similar forces such as SkT2, SkT3 and SIII.

The chapter contains a brief description of the calculations and results obtained in Sec 4.2. Finally, summary and conclusion of the work is discussed in Sec 4.3.

4.2 Calculations and Results

The comprehensive analysis of $^{40,48}Ca+^{96}Zr$ reactions forming $^{136,144}Nd^*$ compound nuclei are carried out in the vicinity of Coulomb barrier. The role of different Skyrme forces is tested in the reaction dynamics and on the basis of their performance, the effect of neutron transfer channel is explored. Additionally, the structural information of decaying fragments of $^{136,144}Nd^*$ compound systems is analyzed using Dynamical Cluster decay Model (DCM). In subsection 4.2.1, the study of the fusion process and neutron transfer effect is carried out within Wong/ extended Wong approach. In subsection 4.2.2, the decay study of $^{136,144}Nd^*$ is investigated using the DCM approach and finally, an attempt is made to correlate the results of fusion and decay mechanisms.

4.2.1 Fusion analysis using Wong model

4.2.1.1 *Testing the performance of different Skyrme forces*

On the theoretical front, the sub barrier fusion anomalies require significant barrier modifications to be in reasonable agreement with experimental data. In this work such modifications are implemented by using a variety of Skyrme forces, based upon

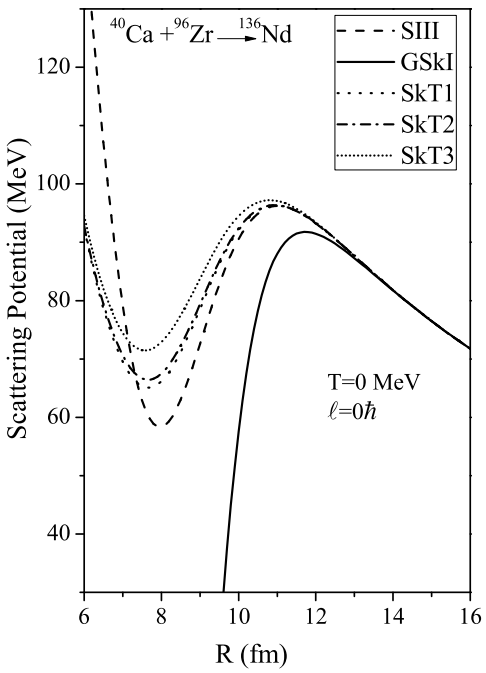

Figure 4.1: Scattering potential of $^{40}Ca +^{96} Zr$ reaction calculated using different Skyrme forces at T=0 MeV.

Skyrme energy density formalism (SEDF). A set of Skyrme forces such as SkT1, SkT2, SkT3, GSkI and SIII from Ref. [10] is used to obtain the nuclear potential. The barrier characteristics of these interactions can be inferred from the scattering plot. The scattering potential V (MeV) as a function of separation distance R(fm) is plotted at temperature, T=0 MeV and ℓ=0 $\hbar$ for $^{40}Ca +^{96} Zr$ reaction as shown in Fig 4.1. Fig 4.1 depicts that SkT3 force has the highest barrier i.e. V_B = 97.22 MeV, followed by SIII, SkT1 and SkT2 forces with V_B = 96.22, 96.30 and V_B = 96.37 MeV respectively (forming similar barrier characteristics), and GSkI having V_B = 91.76 MeV, exhibits significantly different barrier profile and appears at the bottom (lowest barrier). As, SkT3 force offers higher barrier to the colliding nuclei, so we prefer to use SkT1, SkT2, SIII and GSkI forces to explore the behavior of fusion dynamics of $^{40}Ca +^{96} Zr$ reaction.

Firstly, the fusion excitation functions of $^{40}Ca +^{96} Zr$ reaction are calculated

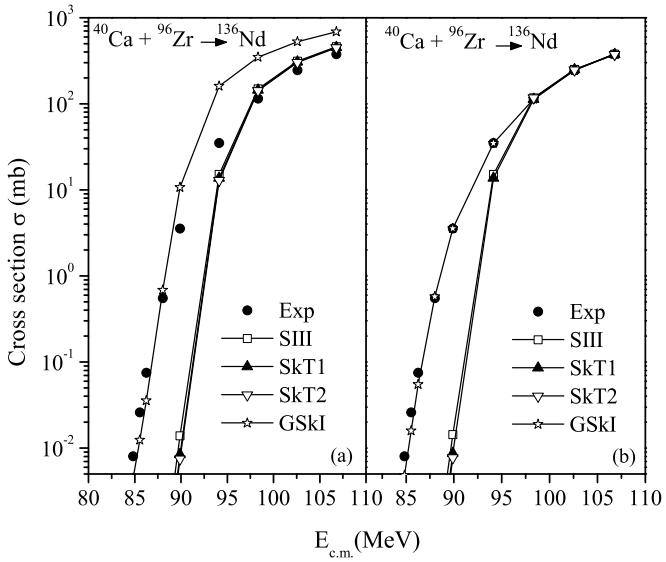

Figure 4.2: Fusion excitation function of $^{40}Ca + ^{96}Zr$ reaction studied within the framework of (a) Wong formula using SkT1, SkT2 and SIII (b) extended Wong model including GSkI force along with same Skyrme forces as in part (a).

within Wong formula by using the Skyrme forces of similar barrier characteristics *i.e.* SIII, SkT1 and SkT2 forces. The calculations are performed over a wide range of incident energies, $E_{c.m.}$= 84.11 to 106.2 MeV, spread across the Coulomb barrier. The comparison of experimental and the calculated fusion cross-sections is shown in Fig 4.2(a). It is clearly observed that the Skyrme forces with similar barrier characteristics perform in the similar fashion at above and below barrier energies. In sub barrier region SIII, SkT1, SkT2 forces suggest the presence of fusion hindrance as the calculated cross sections show deviation from experimental data. This implies that significant modification in the barrier profile is required at sub barrier energies, which may be addressed by choosing the appropriate Skyrme force having appropriate barrier characteristics. Therefore, the GSkI force with low barrier height is used in the calculations and it is found to gives relatively better agreement with the available data, in the sub barrier region (see Fig 4.2(a)). It is noticed that at higher energies GSkI force overestimates the data while, SIII, SkT1, SkT2 Skyrme forces exhibit close accord with the experimental data. This observation seems to suggest

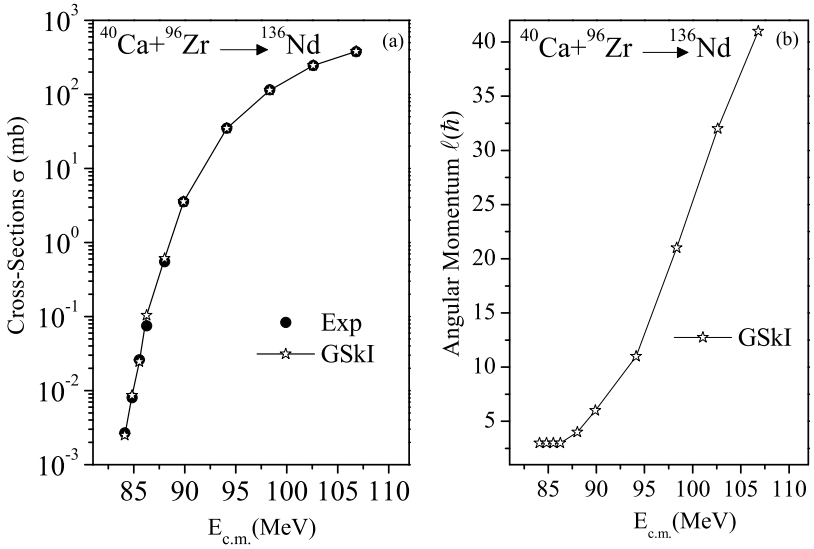

Figure 4.3: (a) Cross sections calculated by taking 1n transfer effect into consideration for $^{40}Ca +^{96} Zr$ reaction deduced using GSkI force is compared with experimental data. (b)Variation in angular momentum with respect to $E_{c.m.}$ is studied for same reaction using same force.

that old Skyrme forces like SIII, SkT1 etc perform better at above barrier region only, whereas relatively new forces like GSkI, seems to address below barrier fusion anomalies but show relatively poor comparison at above the barrier. Hence, to address the problem of overestimation of calculated values at higher energies, extended Wong approach [14] is used. In Fig 4.2(b) calculations carried out with SIII, SkT1, SkT2 and GSkI forces in the framework of extended Wong model are compared with experimental data. The Fig 4.2(b) depicts that all the forces fit the available data at higher energies. But, at lower energies, only GSkI force gives decent agreement with experimental data as compared with other set of chosen Skyrme forces. Thus, the result of Fig 4.2 indicates that the reaction mechanism involved in ^{40}Ca induced reaction changes drastically at sub barrier energies. It may be due to the presence of neutron transfer effect that arises in $^{40}Ca +^{96} Zr$ reaction due to positive Q values of the reaction. This effect increases the quadrupole deformations of the nuclei and reduces the mass asymmetry which in turn decreases the Coulomb barrier and enhances the cross section. Thus, to address the fusion cross sections, especially at

Table 4.1: The fusion cross-section for ^{40}Ca+^{96}Zr reaction deduced using GSkI force within ℓ-summed Wong formula by taking the contribution of 1n-transfer channel.

	X=$\frac{\pi\hbar^2}{2\mu E_{c.m.}}$ $(2\ell+1)$	Y=P^0_ℓ+ v_1/v_0*P^1_ℓ				
ℓ	A	P^0	v_1/v_0*P^1	σ_ℓ= X × Y	σ_{tot}= $\sum_{\ell=0}^{3}$ σ_ℓ	σ_{exp}
			$E_{c.m.} = 84.11MeV$			
0	0.2748	0.00019	0.000414	0.000166		
1	0.8246	0.00018	0.000408	0.000485		
2	1.3744	0.00018	0.000394	0.000789	0.00249	0.00269
3	1.9242	0.00017	0.000375	0.001050		
			$E_{c.m.} = 84.83MeV$			
0	0.2726	0.000657	0.000146	0.000579		
1	0.8178	0.000646	0.00144	0.00171		
2	1.363	0.000626	0.00139	0.00275	0.00861	0.0080
3	1.908	0.000595	0.00132	0.00365		
			$E_{c.m.} = 85.54MeV$			
0	0.2703	0.00220	0.000291	0.000673		
1	0.8109	0.00218	0.00496	0.002171		
2	1.351	0.002131	0.00481	0.00937	0.0246	0.0260
3	1.892	0.00200	0.00461	0.0125		
			$E_{c.m.} = 86.26MeV$			
0	0.2681	0.00761	0.0183	0.0068		
1	0.804	0.00753	0.0176	0.02021		
2	1.340	0.00808	0.0170	0.0336	0.1034	0.0749
3	1.876	0.00694	0.0163	0.0436		

below barrier energy, neutron transfer channels seem desirable. The outcomes of neutron-transfer effects is discussed in the next subsection.

4.2.1.2 *Analysis of neutron-transfer effect using the Skyrme forces*

Using the Eq. (2.15) of chapter 2, the fusion excitation function of ^{40}Ca +^{96} Zr reaction are calculated at low incident energies with GSkI force as it requires lesser barrier modification to address the below barrier data, in comparison to SIII, SkT1 and SkT2 forces. The comparison of calculated values with experimental fusion cross sections is shown in Fig. 4.3(a) and listed in Table 4.1. The analysis shows that

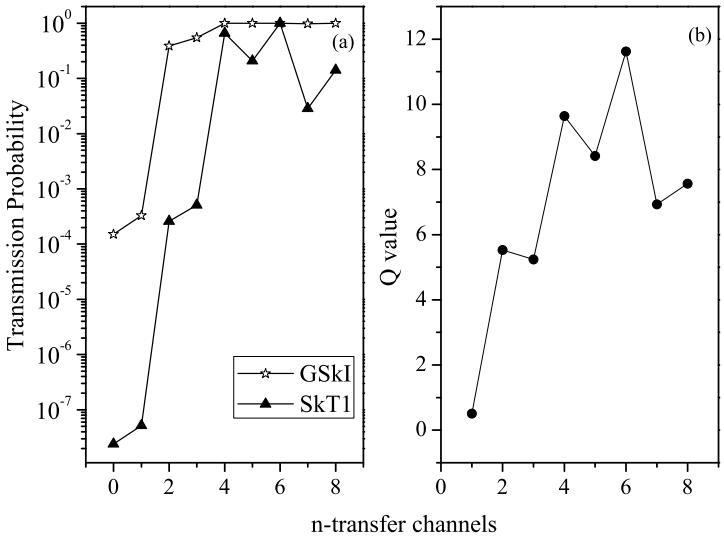

Figure 4.4: (a)Variation in penetrability w.r.t neutron transfer channels analyzed at $\ell = 0$ and (b) variation in Q values w.r.t transfer channels.

inclusion of 1n-transfer channel up to ℓ=3$\hbar$ give decent agreement with experimental data while on adding 2n-transfer channel (not shown here), the experimental value exceeds even at ℓ=0$\hbar$. This is due to the fact that penetrability goes on increasing with increase in the transfer channels and obeys almost same trend as that of Q values of the reaction and therefore for different Skyrme forces, after providing sufficient barrier modification it exceeds the data even at ℓ=0$\hbar$. The variation in penetrability and Q values with respect to neutron transfer channels are shown in Fig. 4.4. Also, the addition of transfer channels smoothen the angular momentum trend with respect to center of mass energy $E_{c.m.}$, shown in Fig. 4.3(b). Further, the same effect is studied for SkT1 force at lowest incident energy, $E_{c.m.}$=84.11 MeV. It is noticed that SkT1 force could not reproduce the data even by including 1n- transfer effect in the calculations. This observation is nearly consistent with [19], wherein the shallow M3Y + repulsive potential corrected for the nuclear incompressibility K $\approx$ 230 (same as for GSkI force), improve the result after one neutron transfer channel. However, SkT1 force is somewhat similar to AW potential which gives poor fit for 1n-transfer channel.

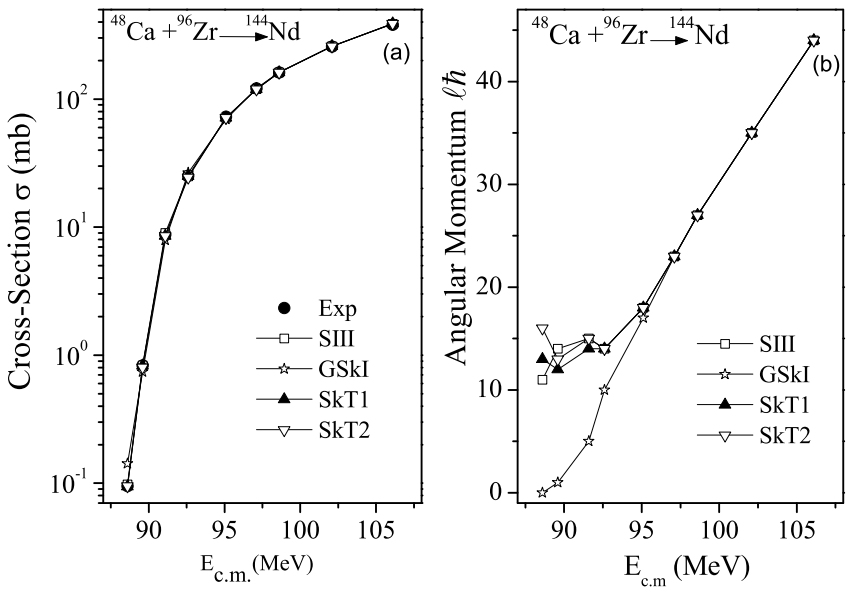

Figure 4.5: (a)Fusion excitation function of $^{48}Ca +^{96} Zr$ reaction is compared with experimental data within extended Wong model,(b)Variation in angular momentum is shown with respect to center of mass energy.

Thus, from the above discussion, one may say that the neutron transfer channels have significant importance in the sub barrier regime. Hence, it is observed that for the addressal of sub barrier fusion anomalies, advanced forces like GSkI are better as they require relatively less barrier alteration as compared to old Skyrme forces like SIII or SkT1.

In addition to this, the fusion of $^{48}Ca+^{96} Zr$ reaction forming $^{144}Nd^*$ is examined across the Coulomb barrier using the extended Wong approach. The fusion excitation function of this reaction are estimated by using SkT1, SkT2, SIII and GSkI Skyrme forces. Fig. 4.5(a) shows the comparison of experimentally and theoretically observed fusion cross sections. It is clearly evident that all the selected forces fit the experimental data at above as well as below the Coulomb barrier. On the basis of available center of mass energies in the sub barrier region, it will be difficult to conclude about the fusion hindrance effect in this reaction. The variation of ℓ_{max}

values for same reaction with respect to $E_{c.m.}$ is shown in Fig 4.5(b). The figure illustrates that ℓ value increase with the increase in center of mass energy. At higher energies, all the forces show smooth variations of ℓ values whereas, at lower energies only GSkI force follows the regular trend as compares to other Skyrme forces. It is because GSkI force is having low barrier and is more sensitive towards isospin effect as compare to SkT1, SkT2 and SIII forces. Here, all chosen Skyrme forces address the fusion cross sections of ^{48}Ca+^{96}Zr reaction without demanding the involvement of n-transfer channel in contrary to that for ^{40}Ca+^{96}Zr reaction. For ^{48}Ca +^{96} Zr reaction also, GSkI gives nice fit with the smooth variation of ℓ_{max} with respect to center of mass energy, $E_{c.m}$. The fusion dynamics of $^{40,48}Ca$ +^{96} Zr reactions show that the neutron transfer effect arises due to positive ground state Q values in ^{40}Ca +^{96} Zr reaction and causes significant change in the fusion cross sections at sub barrier region.

In addition to the fusion process, the decay study of $^{136,144}Nd^{*}$ systems formed in $^{40,48}Ca$ +^{96} Zr reactions is expected to provide useful information about the overall dynamics, so it is worth to examine their decay process. It is well known that the decay of compound system is in general independent of its formation. Hence, the role of neutron transfer channels studied in fusion reaction may not have much significance, once the compound nucleus is formed. But such effects may start contributing when the compound system is at the verge of division. It is relevant to mention that the neck formation between the binary fragments leads to the flow of nucleons between them and provides significant information regarding the decay process [20]. Here, the decay of $^{136,144}Nd^{*}$ nuclei is analyzed in the framework of dynamical cluster decay model and the corresponding results are discussed in the next Section.

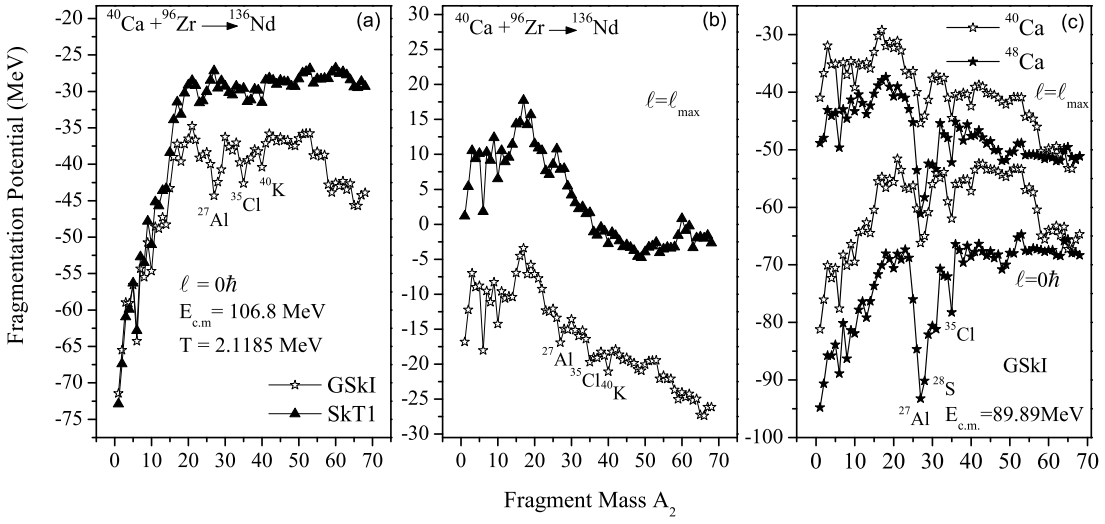

Figure 4.6: Fragmentation potential at $E_{c.m}$= 106.8 MeV using GSkI and SkT1 forces at (a) ℓ=0$\hbar$ and (b) ℓ=ℓ_{max}, and (c) comparison of fragmentation potential in $^{40,48}Ca$ induced reaction at extreme ℓ values.

4.2.2 Decay of $^{136,144}Nd^*$ using DCM approach

In this section, the decay of $^{136,144}Nd^*$ compound systems is studied within the framework of Dynamical Cluster-decay Model (DCM). The previous section shows that GSkI force is relatively favorable in addressing the experimental data, as compare to SkT1, SkT2 and SIII forces. So, the well-performed GSkI force and SkT1 force (from the set of forces with similar barrier profile) are used in further calculations to examine the decay of $^{136,144}Nd^*$ compound systems.

Firstly, the variation in fragmentation potential vs fragment mass A_2 is studied for $^{136}Nd^*$ using GSkI and SkT1 forces. The analysis is done at higher incident energy, $E_{c.m.}$=106.1 MeV over extreme ℓ values as shown in Fig 4.6(a) and (b). These figures exhibit the role of rotational energy in the decay of an excited compound system. At lower ℓ values, light mass fragments seem more prominent contributors towards decay cross sections. As the ℓ value goes on increasing, fission fragments

start competing with light mass fragments. The nuclear interaction potential contributing in fragmentation potential play important role in the evolution of decay dynamics. The GSkI force with lower barrier profile offers lesser magnitude of potential to the decaying fragments as compare to SkT1 force. The structure of potential energy surface (PES) for both forces i.e. GSkI and SkT1 looks similar in light and intermediate mass region, while in the fission region, GSkI force exhibits symmetric distribution of fragments with respect to SkT1 force. Moreover, the deep minima are observed for ^{27}Al, ^{35}Cl, and ^{40}K fragments for GSkI force, which seem to appear due to the deformation effect.

Besides this, the decay mechanism of $^{40,48}Ca +^{96} Zr$ reactions are examined at a common center of mass energy $E_{c.m.}$=89.89 MeV as shown in Fig 4.6(c). The comparison has been done for GSkI force at extreme ℓ values, to acquire structural information in both the reactions. Fig. 4.6(c) illustrates that PES in $^{40,48}Ca$ isotopes are quite similar but the dip of minima for intermediate/heavy mass region for ^{48}Ca channel is large as compared to ^{40}Ca. It is interesting to note that with the increase in neutron number, the symmetric fission window changes from narrow to broader one. Also, the overall fragmentation potential of ^{48}Ca induced reaction (due to neutron excess) is lower in comparison to ^{40}Ca reaction. Besides this, the contribution of light mass fragments at lower ℓ values and fission fragments at higher ℓ values are more prominent for ^{48}Ca as compare to ^{40}Ca. But in the case of ^{40}Ca induced reaction, the penetrability P of the decaying fragments may increase during neck formation in neutron transfer effect. As a result, the cross sections of ^{40}Ca induced reaction enhance with respect to ^{48}Ca reaction. Further, the role of incident energies on the fragmentation potential is analyzed by comparing Figs. 4.6(a), (b) and (c), which depict that deep minima are perceived at lower incident energy and the depth of minima decreases with the increase in the energy of incident beam.

The information of fragmentation potential is further elaborated via preformation probability graph plotted at same energy and ℓ values as Fig 4.7. The Fig.

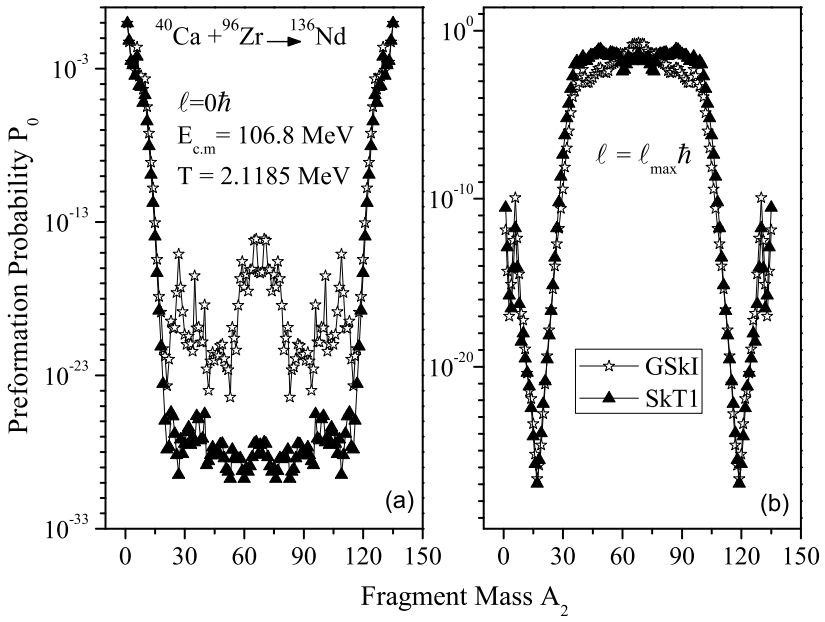

Figure 4.7: Preformation Probability as a function of fragment mass A_2 is calculated at with GSkI and SkT1 forces at (a) ℓ=0 and (b) ℓ=ℓ_{max}.

4.7(a), (b) confirms that probability of light mass fragments is higher at lower ℓ values as compare to ℓ_{max}, where fission fragments start competing. It is noticed that GSkI force gives symmetric type fission while SkT1 force represents the relatively asymmetric fission distribution.

In Ref. [2, 3] the experimental data is available for evaporation residue (ER) only with negligible contribution of fission fragments which means that σ_{fusion}=σ_{ER}+$\sigma_{fission}$ =σ_{ER}. Therefore, the evaporation cross sections are addressed with in DCM approach by adjusting the neck length parameter ΔR. The calculated cross sections are compared with experimental data and tabulated in Table 4.2 for $^{136,144}Nd^*$. From Table 4.2, it is clearly noticed that both the forces give decent agreement with available data for $^{136,144}Nd^*$ compound systems at below and above the barrier region. The behavior of Skyrme forces is analyzed further in terms of barrier lowering ΔV_B. The variation of ΔV_B as a function of $E_{c.m.}$ is examined for $^{136}Nd^*$ nuclei and is shown in Fig. 4.8. The figure depicts that ΔV_B attenuated

Table 4.2: Fusion evaporation cross sections for $^{136,144}Nd^{*}$ nuclei calculated using GSkI and SkT1 forces with in the framework of DCM and are compared with experimental data($\sigma_{Expt.}$) [2, 3].

			$\sigma_{DCM}(mb)$	
$E_{c.m.}(MeV)$	T(MeV)	$\sigma_{Expt.}(mb)$	GSkI	SkT1
		$^{40}Ca +^{96} Zr \rightarrow^{136} Nd^{*}$		
84.11	1.730	0.00269	0.00262	0.00260
84.83	1.734	0.00804	0.00808	0.00802
85.54	1.748	0.026	0.0262	0.026
86.26	1.762	0.075	0.0745	0.747
88.26	1.795	0.552	0.559	0.557
89.89	1.830	3.55	3.536	3.54
94.13	1.906	34.99	34.49	35.01
98.33	1.979	115.2	114.07	115.09
102.60	2.05	246.3	248.08	246.50
106.80	2.12	377.5	375.19	377.01
		$^{48}Ca +^{96} Zr \rightarrow^{144} Nd^{*}$		
88.60	1.664	0.095	0.098	0.0094
89.60	1.683	0.830	0.91	0.831
91.10	1.711	8.73	8.22	8.03
92.06	1.739	25.2	24.75	25.00
95.10	1.784	73.0	72.85	72.80
97.10	1.819	121.0	120.29	120.9
98.60	1.845	161.50	161.13	160.0
102.60	1.905	257.40	254.18	257.20
106.10	1.970	381.0	380.09	380.00

with increasing center of energy, $E_{c.m.}$. The trend is same for both the forces but significant difference lies in their magnitude, especially at lower energy region. The higher magnitude of ΔV_B in SkT1 force implies that it requires more barrier modifications as compare to GSkI force at lower energies. However, at higher energies, ΔV_B becomes comparable for the chosen Skyrme forces. Furthermore, the trend of neck length ΔR which governs the barrier lowering ΔV_B is also examined for GSkI and SkT1 forces. The change in ΔR with respect to $E_{c.m.}$ is shown in the inset of Fig. 4.8. It is depicted that ΔR increases with increase in energy and is higher for GSkI force followed by SkT1 force. For $^{144}Nd^*$ case (not shown here to avoid repetition), the variation of ΔV_B and ΔR with respect to incident energy follow the same trend and exhibit similar result as observed in case of $^{136}Nd^*$ system, where only difference lie in their magnitude. At sub barrier energies, the SkT1 force for $^{144}Nd^*$ demands relatively lesser barrier adjustment than $^{136}Nd^*$ nucleus. It means that the below barrier anomalies are relatively small in neutron rich nuclei as compares to neutron deficient one, as discussed in Section 4.2.1.

Further, the behavior of GSkI and SkT1 Skyrme forces is intended to explore in the fission mass distribution of ^{130,136}Nd compound systems formed via ^{40}Ca+^{90,96}Zr reactions at common center of mass energy $E_{c.m.}$ =106 MeV. The observation is depicted in Fig 4.9, which reveals that fission mass region changes significantly on moving from ^{130}Nd to ^{136}Nd compound system. In ^{130}Nd case, the GSkI Skyrme force with lower barrier height gives relatively symmetric peak in the fission region along with small contribution from the heavy mass fragments while the SkT1 force having higher potential leads to asymmetric mass distribution with comparable contribution from heavy mass region. The similar results are obtained for ^{48}Ca+^{90}Zr reaction as well. This implies that change in the neutron number of decaying compound nucleus (i.e. ^{130}Nd, ^{136}Nd, or ^{138}Nd) modifies the overall mass distribution of the system.

On the basis of results discussed in subsection 4.2.1 and 4.2.2, the following observations are made.

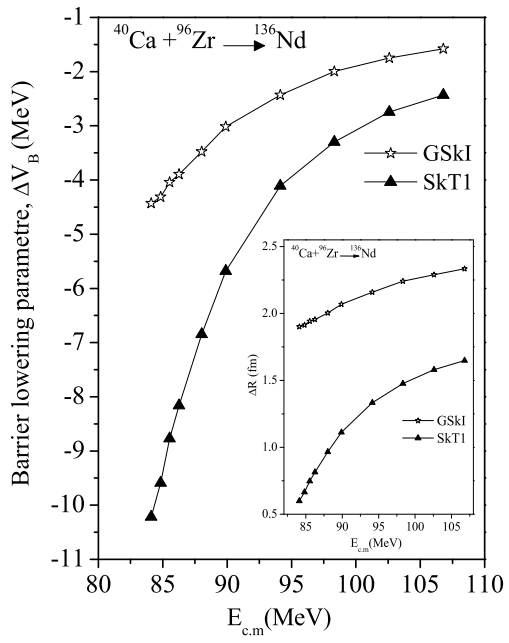

Figure 4.8: Variation of ΔV_B with respect to center of mass energy $E_{c.m}$, calculated for GSkI and SkT1 forces.

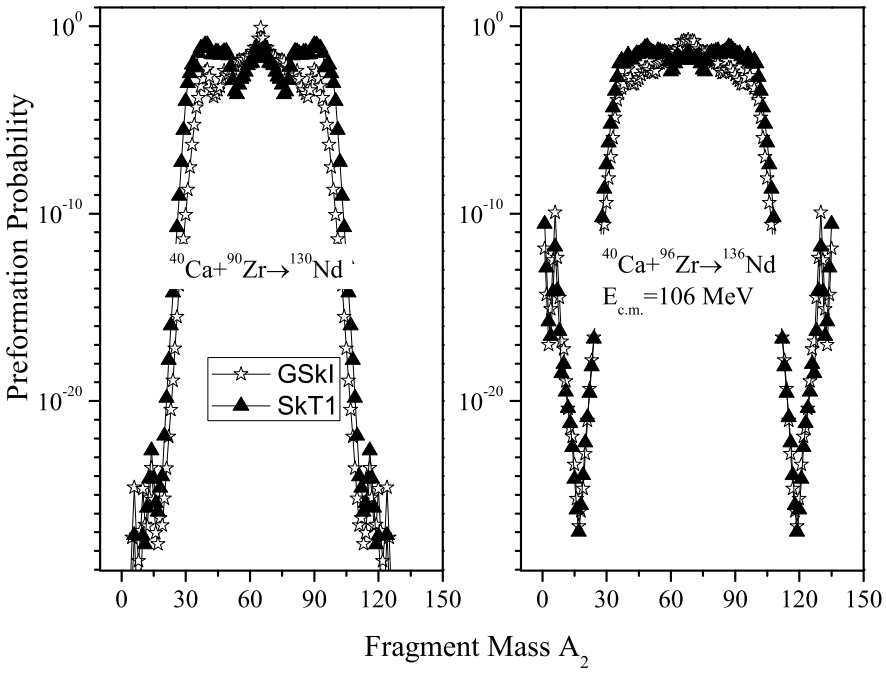

Figure 4.9: Preformation Probability as a function of fragment mass A_2 is obtained using GSkI and SkT1 Skyrme forces for ^{40}Ca+ ^{90,96}Zr reactions.

In the fusion process, the flow of neutrons regulates the fusion mechanism at deep and sub barrier energies. Basically, it forms a neck between the colliding nuclei, which reduces the Coulomb barrier and consequently enhances the fusion cross sections. The neutron transfer effect has been analyzed via transmission probability, P_ℓ which ensures that n-transfer contribution for GSkI force is relatively small in comparison to other considered forces, as it offers lower barrier for the colliding nuclei. On the other hand, the n-transfer effect in the decay can be analyzed on the basis of neck length "ΔR" which provides adequate modification in the barrier distribution of decaying fragments. In case of smaller ΔR, the colliding nuclei come close to each other, thereby the possibility of n-transfer gets enhanced. While, for higher ΔR, the neutrons transfer probability decreases and hence reaction time changes accordingly. On the basis of neck-length ΔR, the relative behavior of Skyrme forces have been examined, where it is observed that GSkI force with higher ΔR requires lesser barrier adjustment in terms of transfer channel, as compared to SkT1 and other chosen forces. Also, one can co-relate the neck length ΔR with the reaction time and conclude that time scale for GSkI force is comparatively smaller than that for other forces opted in the present analysis. Hence, fusion and decay studies suggest that, GSkI force is more preferable over SkT1 force (or SkT2 and SIII forces) particularly in below barrier region.

The present calculations are confined to 1n-transfer effect only. However, it would be of further interest to investigate 2n-transfer effect along with the neutron-neutron pairing correlation in fusion of ^{40}Ca induced reactions [21].

4.3 Conclusions

The fusion, as well as decay analysis of $^{40,48}Ca + ^{96}Zr$ reactions, is carried out using Wong, ℓ-summed Wong and Dynamical Cluster-decay Model (DCM) respectively. The behavior of different Skyrme forces SIII, SkT1 and SkT2 are examined in the sub barrier region of the aforementioned reaction and is compared with the GSkI

force. It is observed that GSkI force exhibits 1n-transfer effect in $^{40}Ca + ^{96}Zr$ reaction. However, the performance of other considered Skyrme forces does not improve even after the inclusion of 1n- transfer effect. The GSkI force with advanced parameters (obtained by fitting various properties of normal and isospin rich nuclei) gives better results across the Coulomb barrier, with the smooth variation in ℓ_{max}-values. Further, the fusion excitation functions of $^{48}Ca + ^{96}Zr$ reaction are reasonably addressed without the requirement of n-transfer effect. Moreover, the decay dynamics of compound systems $^{136,144}Nd^*$ formed in $^{40,48}Ca + ^{96}Zr$ reactions is explored in the framework of DCM. It is noticed that different Skyrme forces give similar fragmentation pattern except for fission region. The mass distribution of out going fission fragments shows a drift from symmetric to relatively asymmetric distribution for GSkI and SkT1 forces respectively. In consistent with Wong observation, the DCM calculations also signify that GSkI force performs better particularly at sub barrier region. It is evident from the neck length parameter ΔR, which shows that GSkI force requires lesser barrier modification as compared to SkT1 force.

After the detailed study of structural effects, Skyrme interactions and various reaction processes for different compound systems, an effort is made to investigate the dynamics of reactions with astrophysical interest at stellar energies i.e. sub barrier energies by using the Skyrme interactions of stellar interest. The results are discussed in chapter 5.

Bibliography

[1] H. Timmer *et. al*, Phys. Lett. B **399**, 35-39 (1997).

[2] A. M. Stefanini *et. al*, Phys. Rev. C **73**, 034606 (2006).

[3] A. M. Stefanini *et. al*, Phys. Lett. B **728**, 639-644 (2014).

[4] Z. Kohley *et. al*, Phys. Rev. C **87** 064612 (2013).

[5] V. I. Zagrebaev, Phys. Rev. C **67** 0610601(R) (2006).

[6] J. J. Kolata *et. al*, Phys. Rev. C **85**, 054603 (2012).

[7] V. V. Sargsyan, G. G. Adamian, N. V. Antonenko, W. Sheid, and H. Q. Zhang, Phys. Rev. C **85**, 024616 (2012).

[8] H. Esbensen, G. Montagnoli, and A. M. Stefanini, Phys. Rev. C **93**, 034609 (2016).

[9] D. Vautherin and D. M. Brink, Phys. Rev C **5** 626 (1972).

[10] M. Dutra, O. Lourenço, J. S. Sá Martins, and A. Delfino, J. R. Stone, P. D. Stevenson, Phys. Rev. C **85**, 035201 (2012).

[11] I. Sharma, R. Kumar, and M. K. Sharma, Eur. Phys. J. A **53**, 140 (2017).

[12] D. Jain, R. Kumar, and M. K. Sharma, Phys. Rev. C **85**, 024615 (2012).

[13] C. Y. Wong, Phys. Rev. Lett. **31**, 766 (1973).

[14] R. Kumar, M. Bansal, S. K. Arun and R. K. Gupta, Phys. Rev. C **80**, 034618 (2009).

[15] R. K. Gupta, M. Balasubramaniam, R. Kumar, D. Singh and C. Beck, Nucl. Phys. A **738**, 479-482 (2004).

[16] R. K. Gupta, M. Balasubramaniam, R. Kumar, D. Singh, C. Beck and W. Greiner, Phys. Rev. C **71**, 014601 (2005).

[17] R. K. Gupta, Clusters in Nuclei, Lecture Notes in Physics 818, Vol. I, editied by C. Beck (Springer-Verlag, Berlin) p. 223 (2010).

[18] M. K. Sharma, S. Kanwar, G. Sawhney, R. K. Gupta and W. Greiner, J. Phys. G: Nucl. Part. Phys. **38**, 055104 (2011).

[19] H. Esbensen, and S. Misicu, Phys. Rev. C **76**, 054609 (2017).

[20] J. Toke *et al.*, Nucl. Phys. A, **440**, 327-365 (1985).

[21] C. Agodi *et al.*, Phys. Rev. C, **97**, 034616 (2018).

Chapter 5

Decay dynamics of ^{28}Si* at stellar energies

In the earlier chapters, various Skyrme forces were employed to examine the reaction process of nuclei belonging to different mass range. Both, the fusion and the decay processes were addressed in the vicinity of Coulomb barrier, where the sub barrier regime was predominantly focused. Extending the study to relatively lighter mass range i.e. ^{28}Si* formed by ^{12}C+^{16}O reaction known for its astrophysical interest is analyzed at sub barrier energies (4-5 MeV). The Skyrme interactions specifically constructed for the study of stellar reactions are examined in the decay dynamics of above mentioned reaction by using the dynamical cluster decay model.

5.1 Introduction

Nuclear reactions play an important role to interpret the fundamental aspects of nuclear physics such as nuclear structure, properties and the dynamics associated with them. The structural information entangled with colliding and decaying fragments gives assess to examine the underlying reaction mechanism and interpret the related phenomenon. With the advent of heavy-ion accelerators, numerous reactions with light heavy-ion beams like ^{12}C,^{16}O were carried out using the variety of target nu-

clei. Eventually, the fusion of light stable beam became an important route for the production of nuclear isotopes with mass A$\leq$20 [1]. The low energy reactions with C and O induced nuclei, emerged as a fertile field for the evolution of new ideas in the nuclear structure physics, which play imperative role in the fusion as well as subsequent fragmentation process. Interestingly, the excitation functions with beams of C and O undergoing ^{12}C+^{12}C, ^{12}C+^{16}O, ^{16}O+^{16}O reactions exhibit the presence of resonant structure [2–5] at lower energies, which trigger the experimental and theoretical studies to investigate the reaction mechanism. Since the study of ^{12}C, ^{16}O induced reactions at sub barrier energies spread $\sim$ 1 MeV - 5 MeV lie in the Gamow energy region, which is the region of the astrophysical interest [6], therefore makes the analysis relatively more attractive.

Various studies have been done with lighter mass nuclei at energies below and above the Coulomb barrier [7–9]. However, the energy range below the Coulomb barrier is of special interest, as it provides an opportunity to investigate many interesting sub barrier phenomena. On combining the experimental results with theoretical descriptions, useful information can be extracted regarding the understanding of the underlying reaction mechanism. An extensive study on the fusion cross-section of light systems has been done by different groups [2, 10] at very low energies. It was noticed that cross-sectional yield changes dramatically with a small change in the projectile and/or target mass. It called for microscopic treatment of fusion and barrier penetration process observed for light mass systems. Other studies at extremely low energies of lighter mass nuclei point towards the fusion hindrance phenomena [6, 11, 12]. This phenomena significantly influences the reaction mechanism and the reaction rate of the studied reactions. Recently, Fang *et al.* [13] revisited the experimental study on ^{12}C+^{16}O system which is of particular interest due to its importance and relevance in the stellar evolution. The estimated cross-sections are of the order of nb-mb at energy range of 3 - 5 MeV, and exhibit the population of n, p and α as exit channels. Many experimental and theoretical investigations have

also been made for this reaction, which confirms the hindrance behavior in the fusion process [12, 14, 15]. Also, the study of fragment emission from $^{16}O+^{12}C$ reaction at very high energies [1] proclaimed the distribution of Li, Be and B fragments in the decay process.

Such reactions have been studied using various theoretical models: One-dimensional barrier penetration model, optical model, coupled channel model and so on by using proximity type potentials. These models gave reasonable addressal of fusion process [5, 6, 16]. However, the adequate addressal of these reactions need an appropriate form of ion-ion potential [10], that have a common feature to reproduce the nuclear matter properties as well as the properties of finite nuclei and neutron stars. For this purpose, the non-relativistic density and momentum dependent Skyrme-type nucleon-nucleon interactions seem more effective [17]. Therefore, efforts are being made to develop new Skyrme forces which may help to address the complexities of nuclear matter around the saturation density so that the Skyrme forces be adequately applied for the study of neutron star as well as finite nuclear matter. This reinforces the extension of Skyrme interactions, which is done in natural way by adding the high-order density-dependent term that simultaneously describes the properties of finite nuclei and influences the equation of state at very high densities [18]. After the analysis of the Skyrme forces by Dutra *et al.* in ref. [19], efforts were made by Zhen Zhang *et al.* [17] to construct three extended Skyrme interactions namely: eMSL07, eMSL08, eMSL09 that can be potentially used for the study of nuclear matter, finite nuclei and neutron stars. In present work, the newly developed Skyrme interactions are compared with the standardized SIII Skyrme force [20] having single density-dependent term and the generalized GSkI [21] interaction known for extended density dependence.

The dynamics of $^{28}Si^{*}$ compound nucleus (CN) formed under low energy range [13] is analyzed using the collective clusterization approach of the dynamical cluster-decay model (DCM) [22–25]. The above mentioned Skyrme forces are used within the

same methodology to have further insight of heavy-ion induced dynamics of nuclei with $A_{CN} \sim 30$. The effect of quadrupole deformations and optimum orientation is taken into consideration as the low energy reaction dynamics depends upon the surface effects. We are aiming to address the decay of $^{28}Si^*$ nucleus using three different forms of Skyrme interactions by exploring the fragmentation paths of possible decay channels such as alpha, neutron, proton and other competing fragments [13]. The emergence of ^{6}Li fragment as a prominent decay channel encouraged us for the detailed study on its dissociation process [26], and the cross-sectional yield with respect to total fusion cross-sections.

It has been observed that different Skyrme forces lead to similar fragmentation behavior for $^{28}Si^*$ at extreme angular momentum values. The fragmentation potential and preformation probability exhibit the dominance of ^{6}Li, ^{10}B and ^{14}N channels (having npα composition) over the xα like structures i.e. ^{8}Be, ^{12}C. The possibility of these exotic channels was also advocated by authors of Ref. [27]. In the present analysis, we are concerned with the study of light particles n, p, α, and Li emitted in the decay of $^{28}Si^*$ CN at sub barrier region. The ^{6}Li has low binding energy so it may further participate in the cross-sections through cumulative yield. The segregation of lithium nucleus is analyzed by comparing the kinetic energy(K.E) acquired by ^{6}Li fragment with the Q value of the reaction (undergoing the dissociation process). It seems that ^{6}Li possesses sufficient energy to undergo break up mechanism. This observation is in agreement with [28, 29] that light elements such as Li, Be, B are relatively more fragile and tend to destroy at stellar conditions. Besides this, ^{6}Li nucleus may undergo capture process (neutron, proton and alpha capture process) due to positive Q values of the reactions.

The results obtained are discussed in Section 5.2, and the conclusion of work is discussed in Section 5.3.

5.2 Calculations and results

In this chapter, the decay of compound nucleus ^{28}Si* formed in the ^{12}C+^{16}O reaction is analyzed at stellar energies span 4 MeV to 5 MeV. Apart from the population of ^{27}Si, ^{27}Al, and ^{24}Mg channels with the complementary neutron, proton, and alpha particles respectively, other possible exit channels are also explored in the framework of Dynamical Cluster decay Model (DCM). It is important to mention that the center of mass energy $E_{c.m.}$ =4.03 MeV is the lowest energy at which the experimental data [13] for proton, neutron and alpha particles is available. Hence, the calculations are carried out at energies where ample evidence of the decaying fragments is reported. At extremely low energies i.e. $E_{c.m.} \leq 5$ MeV, the calculations are generally influenced by the shape and barrier height of the ion-ion potential and thus efforts are made to explore an appropriate form of nuclear potential that overcomes the existence of resonance structure at lower incident energies. The nuclear potentials based on semi-classical Energy Density Formalism (EDF) are used in the calculations. For reactions of astrophysical interest, certain Skyrme forces having specific inbuilt properties can be potentially used for the study of nuclear reactions under the stellar environment. For such calculations, recently developed eMSL07 Skyrme force is used along with generalized GSkI and standardized SIII Skyrme force. The analysis is divided into two subsections: Section 5.2.1 deals with the decay dynamics of ^{28}Si* compound system examined via fragmentation path, preformation probability, and estimation of cross-sections at sub barrier energies and Section 5.2.2 deals with the study of ^{6}Li fragment, which emerges as prominent decay channel for ^{28}Si* compound nucleus.

5.2.1 Decay dynamics of ^{28}Si* compound nucleus

Firstly, the cross-sections of neutron, proton and alpha particle are calculated by employing different Skyrme forces in the DCM. Here, the ℓ_{max} values for the emission of n, p, and α is decided from the scattering plot V(R) as shown in Fig. 5.1. The ℓ_{max}

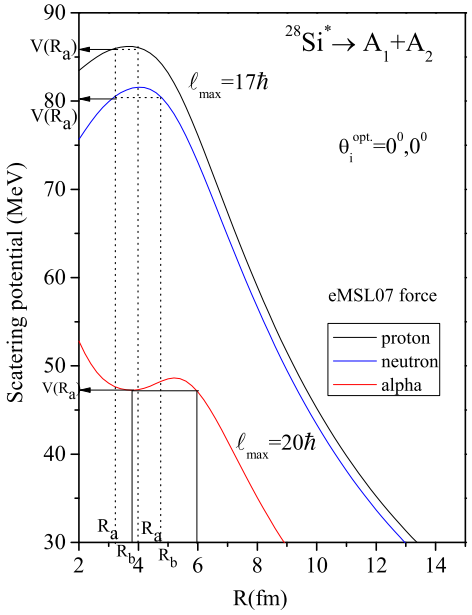

Figure 5.1: Interaction potential (MeV) as a function of R (fm) obtained for n, p, α particles emitted in the decay of ^{28}Si* CN at ℓ_{max} values.

is defined as the maximum value of angular momentum above which the interaction barrier diminishes for the emerging fragments and the penetration probability start approaching the upper limit. The ℓ_{max} for neutron and proton comes out to be 17 $\hbar$ while for heavier alpha fragment the ℓ_{max} is observed to be 20 $\hbar$. Clearly the figure illustrates that scattering potential for lighter particles (n and p) is higher than that of the heavier fragment (α). This might be due to the rotational energy effect, as angular momentum dependent potential is higher for neutron and proton i.e. $V_{\ell n}$=104.938 MeV and $V_{\ell p}$=104.930 MeV, in comparison to that for heavier α particle i.e. $V_{\ell\alpha}$=56.797 MeV.

Next, the structural information from fragmentation potential V(A_2) and the preformation probability P_0 is extracted at $\ell_{min} = 8\ \hbar$ value at energy $E_{c.m.} = 4.03$ MeV. The results are discussed in Figs. 5.2(a) and (b) respectively. The emergence of heavier fragments along with n, p, and α particles is illustrated in Fig. 5.2(a) for three different choices of Skyrme forces. For each Skyrme force, the most probable

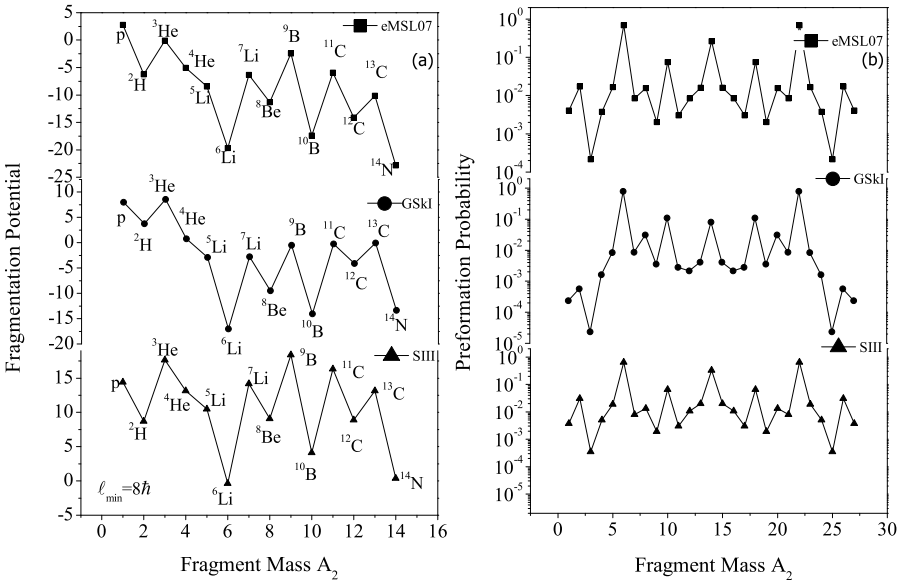

Figure 5.2: Variation in (a) fragmentation potential V(η) (MeV) and (b) preformation probability P_0 with respect to fragment mass A_2 is obtained for $^{28}Si^*$ compound nucleus at $E_{c.m.}$=4.03 MeV and ℓ_{min}= 8 $\hbar$ using SIII, GSkI and eMSL07 Skyrme force.

fragments are identified as ^{6}Li, ^{10}B, and ^{14}N along with their complementary fragments. Each energetically favored fragment has npα like structure, (for instance ^{6}Li $\rightarrow$ n + p + α) that dominates over xα (x=1,2,3,4) like structures say ^{8}Be. The DCM based analysis suggests the possible emergence of lithium, boron, and nitrogen fragments in the decay of $^{28}Si^*$. Also, the temperature corresponding to incident energy $E_{c.m.}$=4.03 MeV is T=2.584 MeV, which means that shell effects may not influence the structural pattern reported in Fig. 5.2. Although there is a significant difference in the magnitude of fragmentation potential and preformation probability, but the relative contribution of exit channels seem independent of the choice of Skyrme force. Also, the higher values of angular momentum sustain the existence of npα like structure as shown in Fig. 5.3(a). The different Skyrme forces exhibit similar structure of the preformation yield at ℓ_{max} values with the highest probability for ^{14}N fragment followed by ^{10}B and ^{6}Li fragments. The penetration probability P is

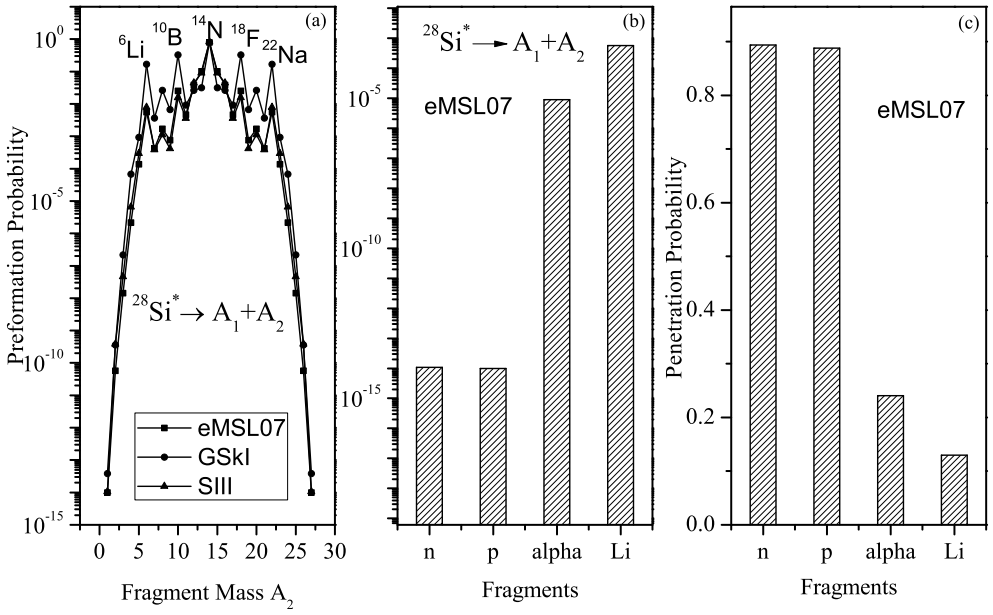

Figure 5.3: (a)Preformation probability vs fragment mass A_2 obtained at optimized value of ΔR at $E_{c.m.}$ = 4.03 MeV and ℓ= 17$\hbar$ using the different Skyrme forces, (b) preformation probability of neutron, proton, alpha and ^{6}Li fragments obtained at respective ℓ_{max} value for eMSL07 force at $E_{c.m.}$=4.03 MeV, (see Fig. 5.1) (c) penetration probability of neutron, proton, alpha and ^{6}Li fragments calculated at respective ℓ_{max} using the eMSL07 Skyrme force.

another important quantity along with preformation probability P_0, to determine the cross-section yield of emerging fragments. Therefore, the variation of preformation and penetration probability of n, p, α and ^{6}Li fragments is compared at ℓ_{max} value and shown in Figs. 5.3(b) and (c). It is evident that the fragments with lower preformation probability have higher probability of tunnelling through the barrier and vice-versa. Since both P_0 and P balance the contribution of light particles in the cross-sectional yield therefore, the cross-section of the decaying ^{28}Si* nucleus is analyzed at available lower incident energies. Table 5.1 shows the comparison of cross-sections of light charged particles evaluated using SIII, eMSL07 and GSkI Skyrme forces with their respective experimental data [13] by optimizing the neck length ΔR, which remains in the limit $\leq$ 2 fm. The observations in Table 5.1 signifies that SIII force overestimates the experimental data for all the light particles even

Table 5.1: Fusion evaporation cross sections of $^{28}Si^*$ compound nucleus calculated using SIII, eMSL07 and GSkI Skyrme forces with in the framework of DCM are compared with experimental data [13].

		$\sigma^{DCM}_{neutron}(mb)$			
$E_{c.m.}$ (MeV)	Temp. (MeV)	SIII (ℓ_{max}=13$\hbar$)	eMSL07 (ℓ_{max}=17$\hbar$)	GSkI (ℓ_{max}=18$\hbar$)	σ_{Exp} (mb)
4.03	2.584	0.151	0.33×10^{-6}	2.93×10^{-6}	$4.38\pm1.00 \times 10^{-6}$
4.20	2.593	0.144	4.08×10^{-6}	2.98×10^{-6}	$8.44\pm2.26 \times 10^{-6}$
4.37	2.603	0.138	4.58×10^{-5}	6.27×10^{-6}	$4.94\pm0.68 \times 10^{-5}$
4.54	2.613	0.129	1.68×10^{-4}	2.28×10^{-5}	$1.16\pm0.12 \times 10^{-4}$
4.67	2.621	0.125	3.46×10^{-4}	1.98×10^{-4}	$1.71\pm0.22 \times 10^{-4}$
4.80	2.630	0.122	1.12×10^{-3}	7.15×10^{-4}	$8.69\pm1.03 \times 10^{-4}$
		$\sigma^{DCM}_{proton}(mb)$			
$E_{c.m.}$ (MeV)	Temp. (MeV)	SIII (ℓ_{max}=13$\hbar$)	eMSL07 (ℓ_{max}=17$\hbar$)	GSkI (ℓ_{max}=18$\hbar$)	σ_{Exp} (mb)
4.03	2.584	0.485	1.07×10^{-5}	1.01×10^{-4}	$2.78\pm0.73 \times 10^{-5}$
4.20	2.593	0.463	5.22×10^{-5}	1.01×10^{-4}	$5.49\pm1.17 \times 10^{-5}$
4.37	2.603	0.447	2.34×10^{-4}	1.64×10^{-4}	$2.30\pm0.22 \times 10^{-4}$
4.54	2.613	0.419	3.31×10^{-4}	3.64×10^{-4}	$5.18\pm0.48 \times 10^{-4}$
4.67	2.621	0.408	1.47×10^{-3}	1.19×10^{-3}	$1.49\pm0.16 \times 10^{-3}$
4.80	2.630	0.390	4.28×10^{-3}	4.76×10^{-3}	$4.79\pm1.01 \times 10^{-3}$
		$\sigma^{DCM}_{alpha}(mb)$			
$E_{c.m.}$ (MeV)	Temp. (MeV)	SIII (ℓ_{max}=14$\hbar$)	eMSL07 (ℓ_{max}=20$\hbar$)	GSkI (ℓ_{max}=32$\hbar$)	σ_{Exp} (mb)
4.03	2.584	0.0123	2.76×10^{-4}	3.81×10^{-4}	$1.67\pm0.73 \times 10^{-5}$
4.20	2.593	0.0120	1.25×10^{-4}	5.46×10^{-4}	$3.49\pm1.17 \times 10^{-5}$
4.37	2.603	0.0114	2.03×10^{-4}	4.27×10^{-4}	$1.56\pm0.22 \times 10^{-4}$
4.54	2.613	0.0112	3.67×10^{-4}	5.26×10^{-4}	$3.94\pm0.48 \times 10^{-4}$
4.67	2.621	0.0109	1.02×10^{-3}	1.03×10^{-3}	$9.18\pm0.16 \times 10^{-3}$
4.80	2.630	0.0103	1.59×10^{-3}	1.91×10^{-3}	$1.60\pm1.01 \times 10^{-3}$

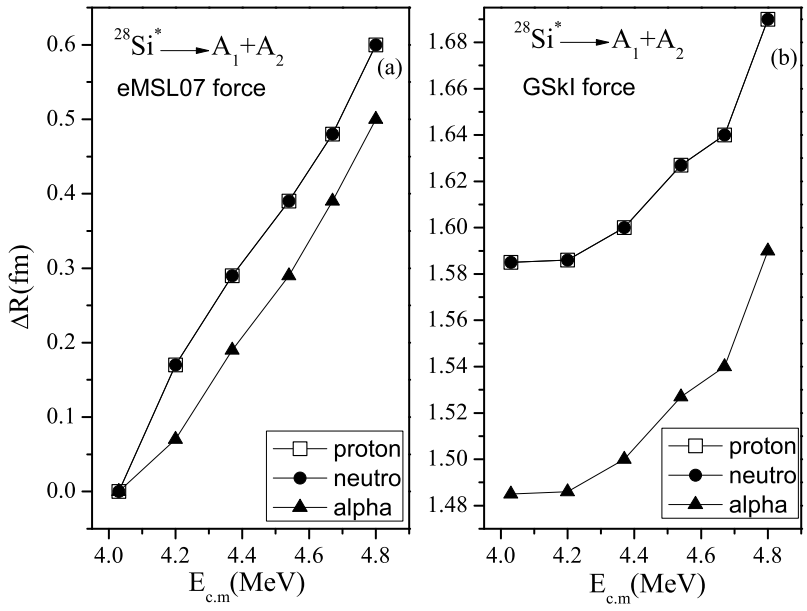

Figure 5.4: Variation of neck length ΔR (fm) with respect to center of mass energy $E_{c.m}$ (MeV) optimized for n, p, and α channels using the (a) eMSL07 and (b) GSkI Skyrme forces.

at ΔR =0 fm. This implies that SIII Skyrme force is not suitable for the dynamics of lighter system and this analysis is in agreement with Ref [30]. The eMSL07 and GSkI Skyrme forces show decent agreement with available data but the later one at relatively higher ΔR value, see Fig. 5.4. From this figure, it is clear that ΔR increases with an increase in center of mass energy. However, the extended GSkI force requires higher ΔR value due to its lower barrier characteristics but always remains in the limit of maximum allowed value. Basically, the ΔR provides information about the reaction time of decaying fragments. Higher the ΔR, faster will be the reaction time and vice-versa. As the light charged particles emit out earlier than heavier fragments, therefore ΔR value for heavier alpha fragment is chosen slightly lesser than neutron and protons i.e. $\Delta R_{n,p}$-0.1. From the comparison, it is depicted that eMSL07 force address the data at $\Delta R \approx 0$ to 0.5 fm while for GSkI force $\Delta R \approx$ 1.50$\pm$ 0.10 fm. The performances of different Skyrme forces is analyzed in view of

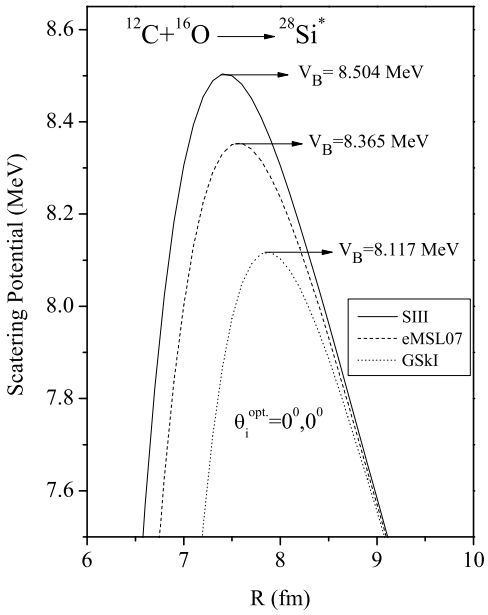

Figure 5.5: (Color online) Scattering potential (MeV) with respect to separation distance R(fm) is determined for SIII, GSkI and eMSL07 Skyrme forces.

fragmentation behavior, preformation probability, cross-sectional yield that consecutively depend on the barrier characteristics such as barrier height, position, and the curvature. Barrier characteristics for chosen Skyrme forces are analyzed from the scattering potential as shown in Fig 5.5. In Fig. 5.5, the scattering potential (MeV) as a function of separation distance R(fm) is plotted for $^{12}C+^{16}O \rightarrow {}^{28}Si^{*}$ reaction using the considered Skyrme forces. The different parameterizations of Skyrme forces are shown to influence the barrier characteristics significantly. The SIII force with old parametrization have higher barrier height and therefore could not address the experimental data. The eMSL07 force has an intermediate barrier height with its Skyrme parameters fitted in such a way that the force is made suitable for the study of stellar as well as heavy-ion induced reactions. Although, GSkI force is considered better in comparison to standardized and generalized Skyrme forces but due to its lower barrier height and higher barrier position the experimental data is reproduced

at higher ΔR values. The eMSL07 Skyrme force reproduces the experimental data nicely by employing lower ΔR values therefore, further calculations are carried out with eMSL07 Skyrme force.

5.2.2 Probing the contribution of ^{6}Li fragment

An analysis is done regarding the contribution of ^{6}Li fragment emerged in the decay of ^{28}Si* compound nucleus at below barrier energies. The low threshold energy of ^{6}Li fragment creates two possibilities that either the lithium fragment survives during the reaction dynamics or it may undergo dissociation process. Regarding these two possibilities, this section is further split into two subsections. In subsection 5.2.2.1, it is assumed that ^{6}Li fragment survives the reaction conditions like temperature and energy, whereas, subsection 5.2.2.2 covers the analysis regarding the dissociation of ^{6}Li, that it could not endure the environmental conditions and undergoes breakup or capture process.

5.2.2.1 *Decay analysis of ^{6}Li fragment*

The study of ^{6}Li fragment is not discussed in the [13], however, its enhanced probability in the decay of ^{28}Si* encourages us to evaluate the relative contribution of light mass lithium (A=6) fragment in the present analysis. As per ref. [1], the decay of ^{28}Si* CN formed via ^{16}O+^{12}C reaction was examined at higher beam energies, and the experimental cross-sections of lithium fragment emerged at higher energies were measured. In view of this the calculations are done with DCM, where the structure of fragmentation potential and preformation probability is examined at higher energies. The observation shows similar result and endorses the presence of ^{6}Li, ^{10}B and ^{14}N fragments with slight variation in the magnitudes (not shown here). The calculations are performed using eMSL07 Skyrme force to evaluate the cross-sections of Li channel available at energies $E_{c.m}$= 50.14, 53.57, 62.14, 68.57 MeV. The results are tabulated in Table 5.2 which depicts that eMSL07 force reproduces the experimental data nicely, except at highest energy, which indicates

Table 5.2: (Upper pannel) The cross sections (mb) of ^6Li fragment emitted from ^{28}Si* compound nucleus are calculated using eMSL07 force with in the framework of DCM at higher energies and thus compared with the available expt. data [1]. (Lower pannel) The excitation function of ^{6}Li are predicted using eMSL07 force at lower incident energies where, the subscript 'a' and 'b' represents the calculations performed using the ΔR same as that used for α particle in Table 5.1 and from linear fit equation respectively.

High barrier energies		$\sigma^{DCM}_{^6Li}(mb)$	
$E_{c.m.}(MeV)$	Temp(MeV)	eMSL07	$\sigma_{Exp}(mb)$
50.14	4.51	40.70	42.68
53.57	4.62	43.96	44.12
62.14	4.92	63.60	68.34
68.57	5.08	64.60	95.16
Sub-barrier energies		$\sigma^{DCM}_{^6Li}(mb)$	
$E_{c.m.}(MeV)$	Temp(MeV)	eMSL07^a	eMSL07^b
4.03	2.584	0.0184	0.396
4.20	2.593	0.0233	0.397
4.37	2.603	0.186	0.390
4.54	2.613	0.264	0.383
4.67	2.621	0.379	0.392
4.80	2.630	0.416	0.391

Table 5.3: Comparison of emission time of light fragments emerged in the decay of ^{28}Si* CN.

eMSL07 force				
$E_{c.m.}(MeV)$	n	p	α	^{6}Li
4.03	0.624×10^{-8}	0.185×10^{-8}	0.600×10^{-15}	0.800×10^{-18}
4.80	0.218×10^{-10}	0.367×10^{-10}	0.169×10^{-15}	0.728×10^{-18}
$E_{c.m.}(MeV)$	Li/n	Li/p	Li/α	
4.03	10^{-10}	10^{-8}	10^{-3}	
4.80	10^{-8}	10^{-8}	10^{-3}	

the possible presence of deep inelastic collision process. The ΔR values optimized at higher incident energies are then extrapolated to extremely low energies using the equation of linear fit, ΔR=0.0305 $E_{c.m}$+0.2603. Extracting the ΔR value for sub-barrier energies, the excitation functions of ^{6}Li are determined (represented by eMSL07^{b}) and compared with the calculations done at same ΔR and ℓ_{max} values as chosen for alpha decay (shown by eMSL07^{a}) see Table 5.2. It is evident that the predictions made via two different ways are comparable at higher energies $E_{c.m}$ =4.54, 4.67, 4.80 MeV. The discrepancies in the cross-sections at lower energies suggest that further investigations are desired in the deep sub barrier region.

Further information regarding the emergence of n, p, α, and ^{6}Li fragments in the decay process is gathered from their respective emission time. The emission time of these particles is determined at respective ΔR values which signifies the sequence at which the particles are emitted from the parent ^{28}Si* compound nucleus. The results are shown in Table 5.3 along with the ratio of emission of ^{6}Li fragment with respect to n, p, and alpha particle. The comparison is shown at extreme sub barrier energies only. The study indicates that ^{6}Li emits out at earlier stage followed by alpha, n, and p. However, the significance of the ratio of emission time points out

Table 5.4: Comparison of kinetic energy (K.E) of ^{6}Li nucleus with the Q value of dissociation reaction.

eMSL07 force			
$E_{c.m.}(MeV)$	TKE(MeV)	K.E (^6Li)(MeV)	$Q_{eff.}$(MeV)
4.03	31.448	24.709	20.642
4.80	37.414	29.519	21.654

the ampleness of particular particle in the decay of excited compound system. The ratio of Li/p is in accordance with the abundance of lithium nucleus as discussed in refs. [31, 32], while the ratio with other particles is predicted for further validation. Further, the isotopic abundance of ^{6}Li/^{7}Li emitted from ^{28}Si* CN is calculated at energy E$_{c.m}$=4.03 MeV which comes out to be 0.075, giving reasonable agreement with the isotopic abundance of lithium as per [32, 33].

Above analysis is useful if ^{6}Li fragment sustains the environmental condition developed during reaction mechanism such as temperature, energy, etc. However, refs [29, 31, 34] suggest that ^{6}Li may not survive at present energy, temperature and therefore, it may undergo secondary decay or radiative capture process.

5.2.2.2 *Analysis regarding the segregation of ^6Li fragment*

Many studies have disclosed that ^{6}Li can easily dissociated at temperature i.e. T $\approx 10^6$ K [33–35] in stellar environment. The fragility of ^6Li nucleus opens up two possibilities that either (i) ^{6}Li may break into its constituent particles and contribute towards the total fusion cross-section via cumulative yield or (ii) it may interact with neutron (proton or alpha) and produce ^{7}Li(^{7}Be or ^{10}B) nuclei, resulting in their abundance in stellar reactions. The studies [28, 29] suggested that lithium nuclei (^{6}Li,^{7}Li) destroy on interacting with the low energy proton(or neutron), as these nuclei can not sustain the temperature of the stellar environment [32]. Hence, the above analysis insists us to further investigate this problem for deep insight of

undergoing mechanism with particular interference to the emergence of ^{6}Li fragment.

In order to analyze the survival of ^{6}Li fragment, the kinetic energy carried away by ^{6}Li fragment is calculated at extreme energies. The kinetic energy so obtained is compared with the Q values of the lithium-depletion reaction i.e. $^{6}\mathrm{Li} \rightarrow \alpha +$ proton + neutron. The study is done using eMSL07 Skyrme force and the result is shown in Table 5.4. Here, TKE represents the total kinetic energy shared among the lightest and heaviest fragments emerged in the decay process, however, kinetic energy (K.E) (as per Eq. (2.55) of chapter 2) represents the fraction of energy carried away by ^{6}Li fragment. The Q values (as discussed in Sec 2.6 of chapter 2) of the reaction are calculated, and it increases with increase in center of mass energy. On comparing K.E of ^{6}Li fragment with the Q_{eff} value, it seems that ^{6}Li fragment acquires sufficient energy to undergo dissociation process and contributes to primary decay via cumulative yield.

Also, it was observed that the relative population of each emerging channel depends upon Q-value of the reaction. For instance, the Q-values of n, p, and α particles are given as

$^{12}\mathrm{C}(^{16}\mathrm{O},\mathrm{p})^{27}\mathrm{Al}$ Q = 5.170 MeV,

$^{12}\mathrm{C}(^{16}\mathrm{O},\alpha)^{24}\mathrm{Mg}$ Q = 6.772 MeV and,

$^{12}\mathrm{C}(^{16}\mathrm{O},\mathrm{n})^{27}\mathrm{Si}$ Q = -0.424 MeV

In reference to [13], α and proton channels have more dominance over the neutron emission channel. This implies that higher the Q value more will be the contribution of that particular channel towards the total fusion cross-sections. In view of this, the Q-value of ^{6}Li channel is observed as

$^{12}\mathrm{C}(^{16}\mathrm{O},^{6}\mathrm{Li})^{22}\mathrm{Na}$ Q = 10.049 MeV

which confirms its possible existence in the decay dynamics of ^{28}Si nucleus. However, ^{6}Li fragment can be destroyed via radiative capture process leading to the

production of other fragments such as

^{6}Li(p, γ)^{7}Be Q = 5.606 MeV,

^{6}Li(n,γ)^{7}Li Q = 7.251 MeV and,

^{6}Li(α,γ)^{10}B Q = 4.461 MeV.

On comparing the Q values of different capture processes, the possible emergence of ^{7}Li fragment seems relatively higher in comparison to ^{7}Be and ^{10}B fragments. Also, these Q values are comparable with the Q values of n, p and α channels, which implies the considerable possibility of radiative capture process of charged and neutral particles via ^{6}Li fragment.

5.3 Conclusions

This chapter aims to explore the dynamics of light mass heavy-ion induced reaction at extremely low incident energies lying in the vicinity of astrophysical interest. The effective Skyrme interactions seem suitable for the study of such reactions, so newly developed eMSL07 force is used in conjunction with the conventional SIII and generalized GSkI Skyrme force. The theoretical analysis is executed using dynamical cluster decay model(DCM). The observations from the DCM model suggest that, the light particles are emitted along with the npα like structure that dominates over xα structure independent of incident energy, choice of Skyrme forces, and angular momentum effects. The cross-sections of n, p, and alpha channels give decent agreement with experimental data for eMSL07 and GSkI Skyrme forces, while standardized SIII Skyrme force overestimate the data at all incident energies. This implies that SIII Skyrme force may not be suitable for the study of nuclear reactions with the light projectile beam(s). Using eMSL07 force, the cross-sections of ^{6}Li fragment are predicted at sub barrier energies. Alternatively, it is emphasized that ^{6}Li may undergo dissociation process. The comparison of kinetic energy and Q value of the ^{6}Li nucleus signifies the possibility of disintegration of ^{6}Li into npα

fragments due to its fragile nature. Moreover, the capture process seems possible due to positive Q values of the neutron, proton and alpha capture reactions.

The chapters 3, 4, and 5 cover extensive analysis on sub barrier region for different reactions spread from light to superheavy mass region. In the next chapter, the decay analysis of $^{244}Am^{*}$ compound nucleus is carried out which actually concerned with above barrier energies. The analysis is done using different Skyrme interactions in the framework of dynamical cluster decay model.

Bibliography

[1] S. Kundu *et al.*, Phys. Rev. C **78**, 044601 (2008).

[2] R. Q. Stokstadf, Z. E. Switkowski, R. A. Dayras, and R. M. Wieland, Phys. Rev. Lett. **37**, 888 (1976).

[3] C. L. Jiang, K. E. Rehm, B. B. Back, and R. V. F. Janssens, Phys. Rev. C **75**, 015803 (2007).

[4] V. Yu. Denisov and N. A. Pilipenko, Phy. Rev. C **81**, 025805 (2010).

[5] M. Notani *et al.*, Phys. Rev. C **85**, 014607 (2012).

[6] E. F. Aguilera *et al.*, Phys. Rev. C **73**, 064601 (2006).

[7] A. Dey *et al.*, Phys. Rev. C **76**, 034608 (2007).

[8] C. Bhattacharya *et al.*, Phys. Rev. C **72**, 021601(R) (2005).

[9] W. Dunnweber *et al.*, Phys. Rev. Lett. **61**, 927 (1988).

[10] Q. Haider and F. B. Malik, Phys. Rev. C **26**, 989 (1982).

[11] H. Esbensen, Phys. Rev. Lett. **85**, 064611 (2012).

[12] C. L. Jiang *et al.*, Phys. Rev. C **71**, 044613 (2005).

[13] X. Fang *et al.*, Phys. Rev. C **96**, 045804 (2017).

[14] L. R. Gasques *et al.*, Phys. Rev. C **76**, 035802 (2007).

[15] M. Pignatari *et al.*, ApJ **762**, 31 (2013).

[16] G. Kocak, M. Karakoc, I. Boztosun, and A. B. Balantekin, Phys. Rev. C **81**, 024615 (2010).

[17] Z. Zhang and L. W. Chen, Phys. Rev. C **94**, 064326 (2016).

[18] Z. W. Zuo, J. C. Pei, X. Yu Xiong, and Y. Zhu, Phys. Rev. C **42**, 064106 (2018).

[19] M. Dutra, O. Lourenço, J. S. Sá Martins, A. Delfino, J. R. Stone, P. D. Stevenson, Phys. Rev. C **85**, 035201 (2012).

[20] E. Chabanat, R. Bonche, R. Haensel, J. Meyer, R. Schaeffer, Nucl. Phys. A **635**, 231-256 (1998).

[21] B. K. Agrawal, S. K. Dhiman, and R. Kumar, Phys. Rev. C **73**, 034319 (2006).

[22] R. K. Gupta, R. Kumar, N. K. Dhiman, M. Balasubramaniam, W. Scheid and C. Beck, Phys. Rev. C **68**, 014610 (2003).

[23] G. Kaur, D. Jain, R. Kumar, M. K. Sharma, Nucl. Phys. A **916**, 260-274 (2013).

[24] D. Jain, R. Kumar, M. K. Sharma and R. K. Gupta, Phys. Rev. C **85**, 024615 (2012).

[25] G. Sawhney, M. K. Sharma, R. K Gupta, Phys. Rev. C **83**, 064610 (2011).

[26] E. M. Tursunov, S. A. Turakulov, A. S. Kadyrov, and I. Bray, Phys. Rev. C **98**, 055803 (2018).

[27] L. R. Greenwood, K. Katori, R. E. Malmin, T. H. Braid, J. C. Stoltzfus, and R. H. Siemssen, Phys. Rev. C **6**, 2112 (1972).

[28] L. ZhiHong *et al.*, Sci. China Phys. Mech. Astron. **54**, 1:s67-s72 (2011).

[29] G. X. Dong, N. Michel, K. Fossez, M. Ploszajczak, Y. Jaganathen and R. M Id Betan, J. Phys. G: Nucl. Part. Phys. **44**, 045201 (2017).

[30] S. J. Krieger and M. S. Weiss, Phys. Rev. C **24**, 928 (1981).

[31] E. Vangioni and M. Cassé, Front. Life Sci **10**, 84 (2017).

[32] A. M. Boesgaard, PASP **88**, 353 (1976).

[33] G. Michaud and P. Charbonneaueau, Space Sci. Rev. **57**, 1-58 (1991).

[34] S. Palmerini, M. Busso, S. Simonucci, and S. Taioli, J. Phys.: Conf. Ser. **665**, 012014 (2016).

[35] A. E. G. Pérez, W. Aoki, S. Inoue, S. G. Ryan, T. K. Suzuki, M. Chiba, A and A, **504**, 353 (2009).

Chapter 6

Probing the role of Skyrme interactions on decay dynamics of $^{6}Li + ^{238}U$ reaction

In preceding chapters, the analysis of diverse reactions comprising of stable projectile-target combinations is carried out by employing Wong/extended Wong and dynamical cluster decay model. Primarily, the sub-barrier energy regime is concentrated wherein the role of deformations, orientations, different Skymre interactions and the neutron transfer effect were analyzed in view of fusion and subsequent decay processes. Extending the analysis for loosely bound case, the fission dynamics of ^{244}Am* compound nucleus formed via ^{6}Li+^{238}U is examined near and above the Coulomb barrier energies by using the NRAPR, SQMC700, SKRA, GSkI, SIII, LNS, KDE0v1 Skyrme forces. The complete and incomplete fusion processes competing at above barrier energies are addressed by using the chosen set of Skyrme forces. Also, the mass distribution of ^{244}Am* compound system and the barrier modification effect induced via different Skyrme forces are explored in the reaction dynamics using the dynamical cluster decay model.

6.1 Introduction

The Skyrme interactions obtained by semi-classical approach of Skyrme Energy Density Formalism (SEDF) [1–3] cover huge set of interaction forces. To obtain the best possible Skyrme interaction that satisfies a wide range of bulk as well as surface properties in the nuclear matter, some macroscopic constraints were imposed on them [3]. In addition to these constraints, more microscopic constraints are applied on the Skyrme forces that reduced the set to 5 forces such as NRAPR, SQMC700, KDE0v1, SKRA and LNS [3]. These forces are assumed to perform well in wide range applications associated with symmetric nuclear matter and pure neutron matter. It is quite interesting to examine the behavior of these selected Skyrme forces in low energy regime of finite nuclei.

The Skyrme forces are represented by the Skyrme Hamiltonian density which contain different set of parameters to explain finite nuclear properties. The recent developments in the related areas introduced some additional higher order terms in the Hamiltonian density. Thus, the Hamiltonian density is modified and based upon this, the Skyrme forces are classified into two categories : Standard form and Non Standard form. The extended form of Skyrme forces (non standard) are introduced by Krewald *et al.* [4], providing GSI-GS6 forces. Further modifications in the Hamiltonian density are introduced by Agrawal *et al.* [5], giving GSkI and GSkII forces that can be effectively used for the study of nuclei ranging from normal to isospin rich region. The selected forces in the present case *i.e.* NRAPR, SQMC700, SKRA, KDE0v1 and LNS are obtained using standard form and are compared with non standard GSkI force.

We intend to analyze the behavior of these Skyrme interactions in ^{6}Li induced reaction involving neutron rich target ^{238}U, using Dynamical Cluster-decay Model (DCM) [6–10]. The available data [11] shows that $^{6}Li + ^{238}U$ reaction contains combined effect of compound nucleus (CN) and non compound nucleus (nCN) processes. In CN process, excited nucleus may de-excite through Evaporation Residue (ER),

Intermediate Mass Fragments (IMF), Heavy Mass Fragments (HMF) and Fission Fragments (FF), whereas nCN gives rise to Quasi Fission (QF) and Deep Inelastic Collision (DIC) etc. Besides this, there is a definite probability of the occurrence of incomplete fusion (ICF), if the projectile has loosely bound structure. The possibility of ICF process in the present case arises due to low threshold energy of ^{6}Li. As a result, ^{6}Li projectile breaks into two fragments and one of these fragment interact with the target, forming compound nucleus, which finally decays via fission. In addition to breakup; transfer induced fission may also come into the picture. In this process, few nucleons are transferred from projectile to target, which further decays into fission fragments. Therefore, the total cross-section in $^{6}Li + ^{238}U$ is a measure of fission fragments from complete fusion (CF) and incomplete fusion (ICF).

The study of fission process in ^{6}Li induced reaction has been addressed within DCM using the effect of deformations and optimum orientation [12], which give average effect of all the possible orientations. It has been observed that inclusion of higher order deformations, and generalized orientations influence the fragmentation potential, but the overall distribution of ER, fission and other competing channels do not change much [13]. Henceforth, we opted for optimum orientation to examine the reaction dynamics over a range of incident energy. Within this approach, the role of different Skyrme forces is analyzed at above and below the barrier energies. The spin orbit part of the forces is fitted to finite nuclei and the NRAPR could reproduce the binding energies of some finite nuclei [14]. Here a comparative study of selected forces is made in the reaction dynamics of $^{6}Li + ^{238}U$. Among the five forces, NRAPR, SKRA and LNS are chosen as they cover the entire barrier profile of the selected set of forces. The theoretical calculations of CCFULL code in reference to [11] account the phenomena of fusion hinderance at below barrier region. In DCM, fusion hindrance is addressed via barrier modification. This barrier modification may be either intrinsic or extrinsic or both, depending on the type of reaction partners involved. Within DCM, the intrinsic barrier modification is achieved either by the

use of deformations and orientations, Skyrme forces or extrinsically via the neck length parameter 'ΔR'.

In the present chapter, we are aiming to test the performance of selected set of Skyrme forces, and subsequently investigate the fission dynamics of $^{6}Li + ^{238}U$ reaction. Most importantly the behavior of Skyrme forces towards fusion hindrance is studied by analyzing percentage change in barrier modification. The results obtained are discussed in Section 6.2. Finally, summary of the work and the conclusions drawn are elaborated in Section 6.3.

6.2 Calculations and Results

The purpose of this analysis is to test the performance of five selected Skyrme forces [3] and examine the dynamics of $^{6}Li + ^{238}U$ reaction within the groundwork of Dynamical Cluster-decay Model(DCM). This section is divided into three subsections. In subsection 6.2.1, the barrier characteristics and related sensitivity issues are addressed in view of use of variety of Skyrme interactions. The fission dynamics and related predictions are explored in subsection 6.2.2. In the end, an effort is made to analyze the incomplete fusion (ICF) contribution with the same forces and the results are discussed in subsection 6.2.3.

6.2.1 Barrier characteristics of Skyrme forces

The scattering potential is plotted as a function of separation distance R(fm) in Fig. 6.1, which depicts the barrier characteristics of NRAPR, SQMC700, SKRA, KDE0v1, LNS, GSkI and SIII forces determined for $^{244}Am^{*}$ at T=1.049 MeV and ℓ=0$\hbar$. Fig. 6.1 illustrates that LNS force has highest barrier and NRAPR along with GSkI force have lowest barrier profile as compared to other set of chosen interactions. The barrier characteristics of SKRA force lies amid LNS and NRAPR forces. The Fig. 6.1 also illustrates that KDE0v1 and SIII forces show almost similar barrier characteristics as that for LNS force. Likewise, SQMC700 and GSkI forces behave

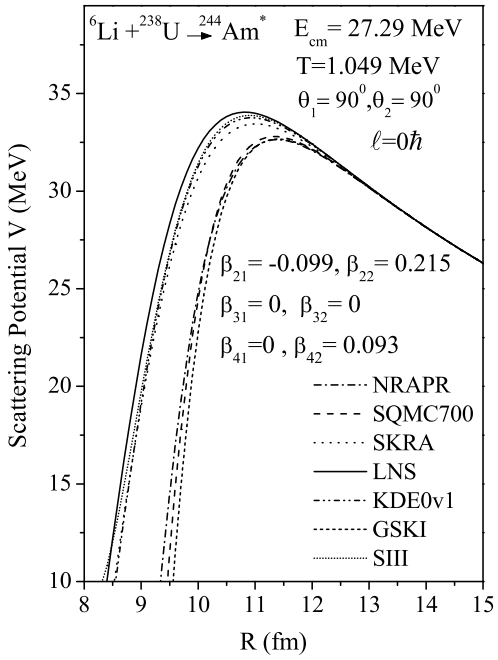

Figure 6.1: Scattering Potential (MeV) vs separation distance R (fm) for deformed choice of colliding nuclei at T=1.049 MeV, and ℓ=0 $\hbar$ is obtained using different sets of Skyrme forces

similar to NRAPR force. The barrier profile of Skyrme forces is found to follow similar trend as governed via the magnitude of structural properties such as effective mass, binding energy per nucleon and incompressibility of the forces. Hence, from the set of five forces, we choose NRAPR, SKRA and LNS forces (with different barrier profile), in order to understand fission dynamics in $^{244}Am^{*}$ compound system.

The interaction potential calculated using chosen set of forces in turn provides us the information regarding barrier characteristics that play significant role to understand the dynamical behavior of heavy-ion induced reactions. In addition to barrier characteristics, it is equally important to acquire information regarding relative performance of different forces. In order to check the sensitivity of interaction potential, the $\frac{dV}{dR}$ is plotted w.r.t separation distance R and the behavior is depicted in Fig. 6.2. One may notice that the $\frac{dV}{dR}$ for NRAPR force changes abruptly. This

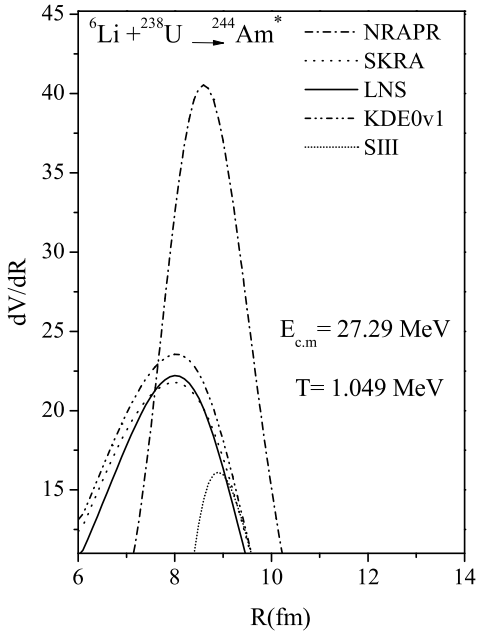

Figure 6.2: Derivative of Scattering potential vs R (fm) for deformed choice of colliding nuclei at T=1.049 MeV, examined for NRAPR, SKRA, KDE0v1, SIII and LNS Skyrme forces.

.

is due to lesser barrier width for NRAPR force, which corresponds to faster rise and fall in the potential values. Moreover, lesser width corresponds to higher tunneling through the barrier and hence larger yield. However, variation of dV/dR for SKRA, KDE0v1 and LNS forces is comparatively small and the variation is even smaller for widely used force SIII.

6.2.2 Fission dynamics and predictions for future experiments

The decay dynamics of compound nucleus $^{244}Am^{*}$ is investigated within the framework of DCM. The relative contribution of decaying fragments can be understood from the fragmentation and preformation profile. Fig. 6.3 gives a description of fragmentation potential of $^{244}Am^{*}$ which is calculated using different forces at

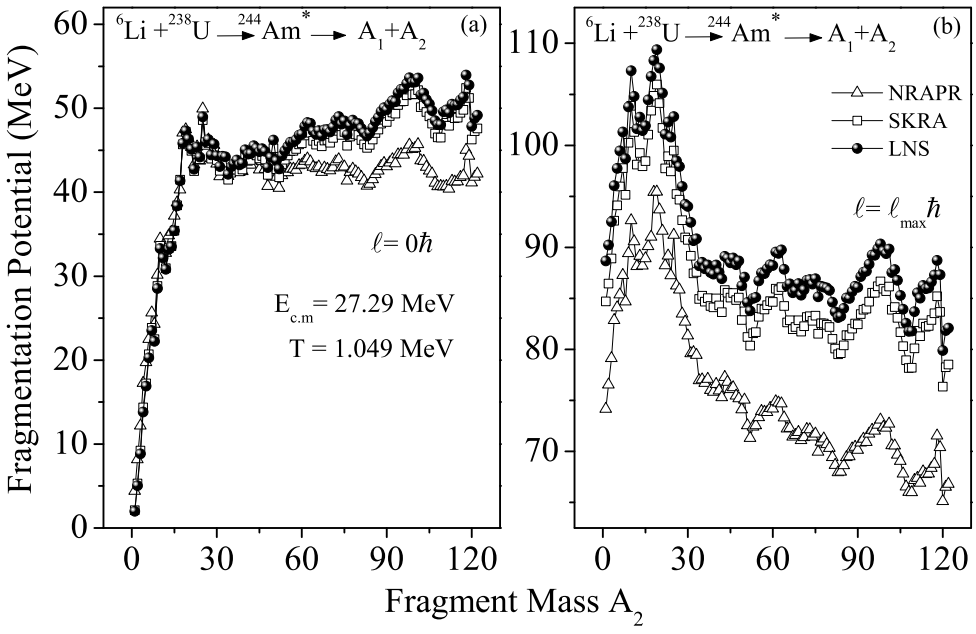

Figure 6.3: Fragmentation Potential (MeV) as a function of Fragment Mass A_2 is calculated using different sets of Skyrme forces at $E_{c.m.} = 27.29$ MeV for the decay of $^{244}Am^{*}$ at (a) $\ell = 0\hbar$, and (b) $\ell = \ell_{max}$

.

$E_{c.m.} = 27.29$ MeV for ℓ=0$\hbar$ and ℓ=ℓ_{max}. From Fig. 6.3(a) and (b) one can clearly observe that the potential energy surfaces of SKRA and LNS forces are almost identical at ℓ=0$\hbar$ and ℓ=ℓ_{max}. The NRAPR force also shows similar structure but with significant change in the magnitude. This change in magnitude is relatively higher for HMF and fission fragments. This may be due to lower potential provided by NRAPR force to the decaying fragments as compares to SKRA and LNS forces. Additionally Fig 6.3(a) illustrates that at lower ℓ-values, ER or light mass fragments dominate and is true for all the forces. However, at higher ℓ-values the fission fragments start appearing at the cost of smaller fragments. This point is further clarified using 3D representation of fragmentation potential at $E_{c.m.} = 40.71$ MeV for $\ell = 0\hbar$ and $\ell = \ell_{max}$, shown in Fig. 6.4 and Fig. 6.5 respectively. The clear description of energetically favored fragments with respect to each Z value is depicted in Fig. 6.4 and 6.5. The fragments with minimum potential have higher probability towards the decay channel. This point is emphasized via preformation probability behavior

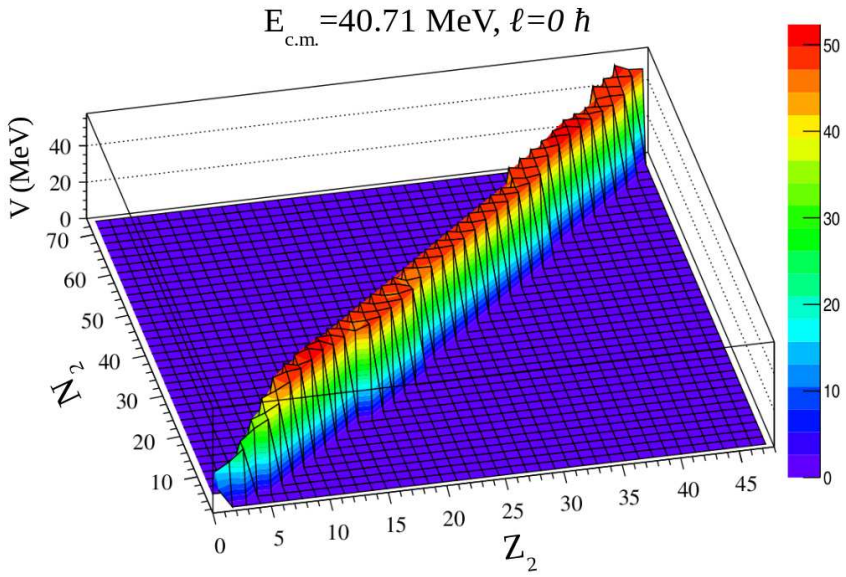

Figure 6.4: (Color online) 3D representation of fragmentation potential at $\ell = 0\hbar$ and $E_{c.m.} = 40.71MeV$ using NRAPR force for $^{6}Li +^{238} U$ reaction.

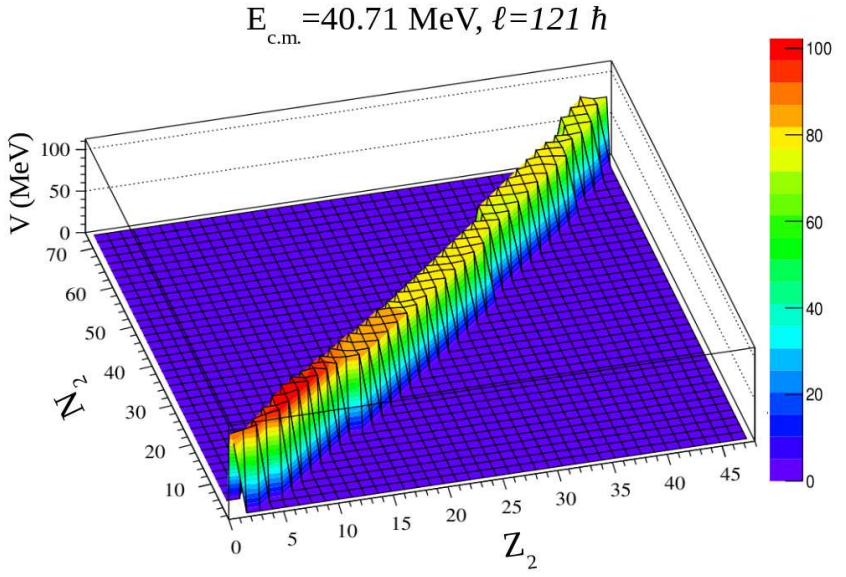

Figure 6.5: (Color online) Same as Fig.4 but at $\ell = \ell_{max}$ using NRAPR force for $^{6}Li +^{238} U$ reaction.

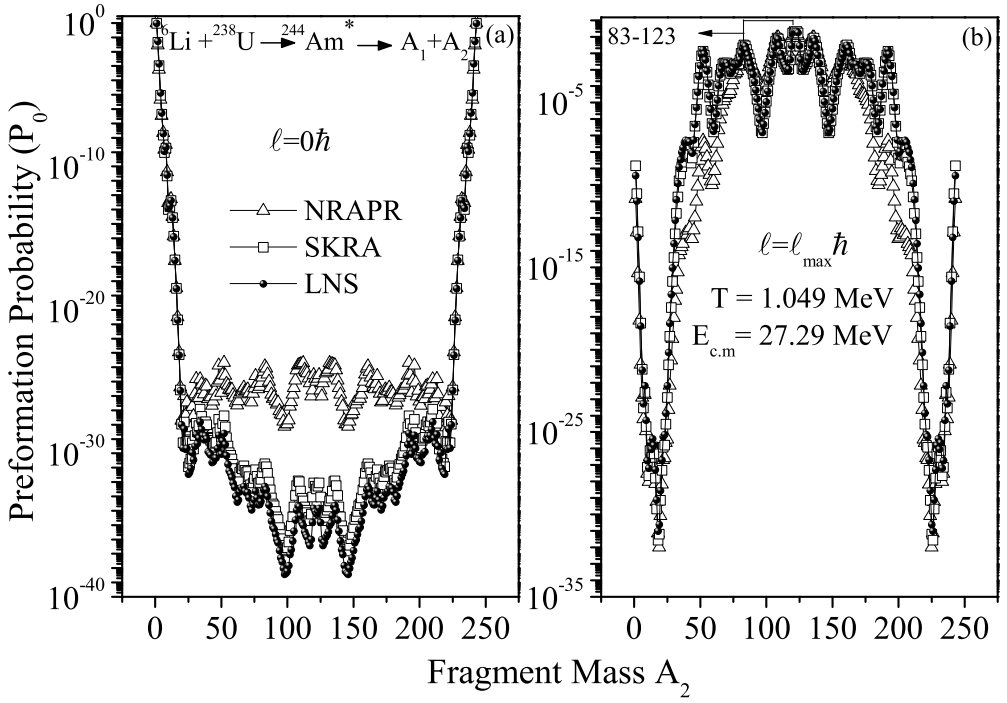

Figure 6.6: Variation in Preformation probability P_0 as a function fragment mass A_2 for deformed choice of colliding nuclei at T=1.049 MeV for (a) $\ell = 0\hbar$ and (b) $\ell = \ell_{max}$. The fission window ranges from A_2 = 83-123 as shown in (b).

depicted in Fig. 6.6. The preformation probability is calculated at $E_{c.m.}$ = 27.29 MeV at ℓ=0$\hbar$ and ℓ=ℓ_{max} using the same set of Skyrme forces. The dominance of light mass fragments over fission fragments at ℓ=0$\hbar$ is seen in Fig. 6.6(a). At higher angular momentum i.e. at ℓ=ℓ_{max} in Fig. 6.6(b), the contribution of fission is more than light mass fragments where fission fragments lie in the range A_2 = 83 - 123. It is important to notice that, independent of the choice of Skyrme force, the relative contribution of different fission fragments is not smooth. The distribution instead shows interesting substructure among the contributing fission fragments. This kind of substructure among the fission fragments may provide further insight for better interpretation of dynamics involved.

The estimation of fission cross sections using DCM is worked out with NRAPR, SKRA and LNS forces over the energy range from $E_{c.m.}$=27.29 to 40.71 MeV. The experimental data and theoretically calculated cross sections are tabulated in Table

Table 6.1: Fission cross sections for $^{6}Li + ^{238}U$ reaction calculated using NRAPR, SKRA and LNS forces with in the framework of DCM are compared with experimental data [11].

				$\sigma_{DCM}(mb)$		
S.No.	$E_{c.m.}(MeV)$	T(MeV)	$\sigma_{Exp}(mb)$	NRAPR	SKRA	LNS
1	25.00	1.012	-	0.00347[1]	-	-
2	26.00	1.026	-	2.7[1]	-	-
1	27.29	1.049	9.55	9.7	9.48	9.92
2	29.07	1.068	33.86	34.27	34.20	34.2
3	31.02	1.086	96.50	94.88	92.20	95.4
4	32.99	1.119	228.5	224.0	226	226
5	34.89	1.151	378.7	375.6	372	372
6	36.83	1.182	597.35	592.2	598	592
7	38.78	1.212	809.394	772.0	768	766
8	40.71	1.242	1021.84	966	956	894

[1]Represents the predicted cross sections at lowest energies.

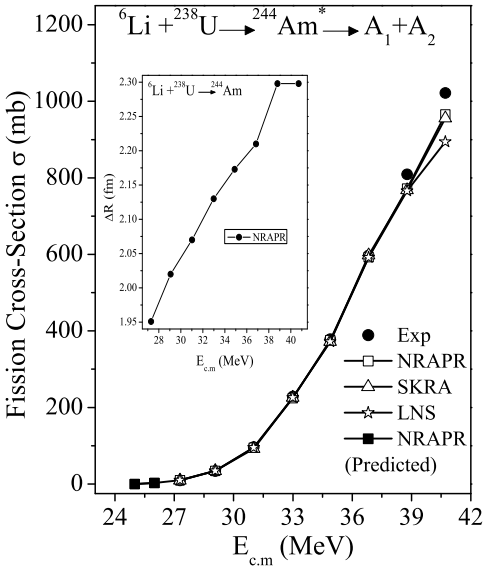

Figure 6.7: The fission cross sections (mb) plotted against $E_{c.m.}$ for $^{6}Li + ^{238}U$ using NRAPR, SKRA and LNS forces, is being compared with experimental data [11]. The predicted cross sections at lowest energies calculated using NRAPR force are represented by filled squares. The change in ΔR w.r.t $E_{c.m.}$ for NRAPR force is shown as an inset.

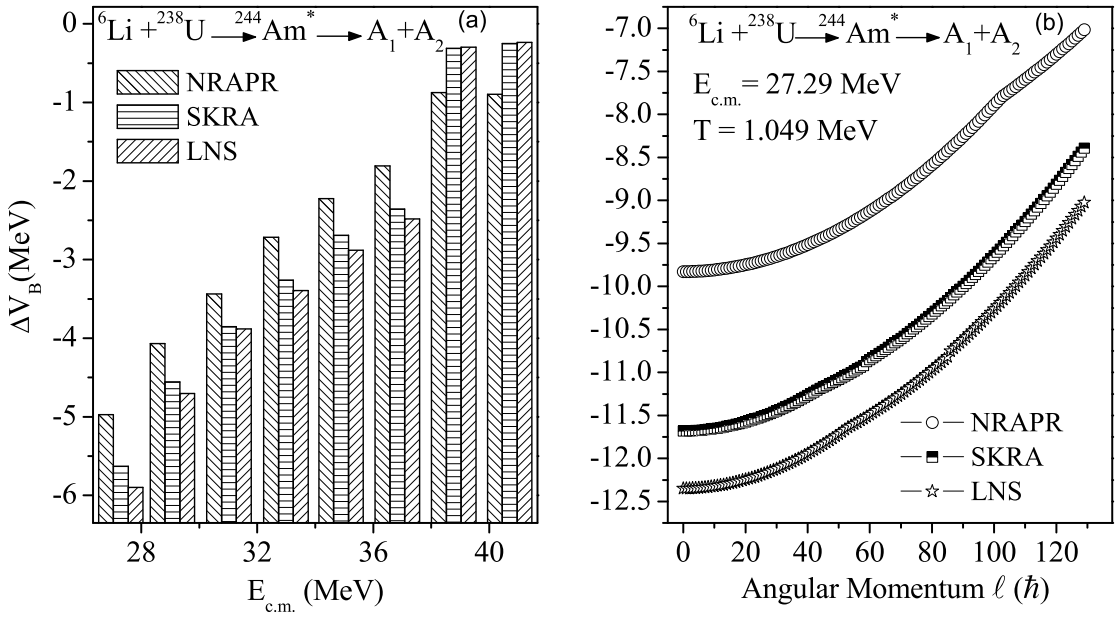

Figure 6.8: ΔV_B as a function of (a)center of mass energy, $E_{c.m.}$ (MeV) and (b) angular momentum $\ell(\hbar)$, deduced using NRAPR, SKRA and LNS Skyrme forces for $^6Li + ^{238}U$ reaction.

6.1 and in Fig.6.7. Apparent from Fig. 6.7 all the forces give excellent agreement within DCM at below barrier energies. However, at higher energies we get somewhat lower cross sections. The variation in neck length with center of mass energy $E_{c.m.}$ is shown for NRAPR force in the inset of Fig. 6.7. The suppression of data suggests the possible contribution of non-compound nucleus (nCN) process, which arises due to low threshold energy of ^6Li and is discussed in subsection 6.2.3.

From the scattering potential, we noticed that different Skyrme forces have different barrier characteristics. Therefore, they require some barrier modifications in order to address the data. Barrier modifications are introduced by neck length ΔR that regulates the barrier lowering parameter ΔV_B [15]. In Fig. 6.8(a), the variation of ΔV_B w.r.t center of mass energy $E_{c.m.}$ is shown for the selected Skyrme forces. It is seen that for all the three forces, the magnitude of ΔV_B decreases with increase in $E_{c.m.}$. At higher energies, unusual trend of forces suggest inadequate addressal of

cross sections. The change in ΔV_B with respect to angular momentum $\ell(\hbar)$ at $E_{c.m.}$ = 27.29 MeV and T = 1.049 MeV for NRAPR, SKRA and LNS forces is shown in Fig. 6.8(b). Here also ΔV_B decreases with increase in ℓ values and it is found that SKRA and LNS forces have higher magnitude than NRAPR force independent of the choice of ℓ values. As SKRA and LNS forces depicted in Fig. 6.8(b) show larger requirement of barrier adjustment, so NRAPR seems to provide an alternate choice to address the dynamics of chosen reaction. In agreement with earlier results, barrier modification is observed to be larger at lower incident energies and angular momentum values.

Furthermore, the variation in $\%\Delta V_B$ obtained by experimental and theoretical fitting of data, helps to provide information about the behavior of forces towards fusion hindrance. Further, the cross sections are obtained using Wong formula at $E_{c.m.}$ = 27.29 MeV, which give comprehensive information of fusion hindrance with all three forces. The theoretical cross sections obtained using Wong formula are then fitted by DCM and their respective $\Delta V_B^{theor.}$ are calculated. On the other hand, $\Delta V_B^{Exp.}$ is deduced by fitting experimental data within the DCM. The difference in $\Delta V_B^{Exp.}$ and $\Delta V_B^{theor.}$ signifies the amount of modifications required by individual force to overcome the fusion hindrance phenomena. The variation in $\Delta V_B^{Exp.}$ and $\Delta V_B^{theor.}$ is expressed in terms of % ΔV_B by

$$\%\Delta V_B = (\Delta V_B^{Exp.} - \Delta V_B^{theor.})/V_B \times 100 \tag{6.1}$$

where V_B is the potential barrier of the Skyrme forces. The % ΔV_B at extreme ℓ-values is studied with selected forces and is shown in Table 6.2. In Table 6.2, it is depicted that percentage ΔV_B is higher at $\ell = 0\hbar$ and decreases with increase in ℓ-values. One can see that NRAPR force shows small % ΔV_B as compare to other two forces at extreme ℓ-values. Thus, NRAPR can be seen as a possible choice for addressing the fusion hindrance.

Apart from these calculations, an attempt is made to predict the data at en-

Table 6.2: % ΔV_B calculated as ($\Delta V_B^{Exp.}$- $\Delta V_B^{theor.}$)/V_B×100 at $E_{c.m.}$ = 27.29 MeV for extreme ℓ-values using NRAPR, SKRA and LNS forces, to address fusion hindrance phenomena in ^6Li +^{238} U reaction. $\Delta V_B^{theor.}$ and $\Delta V_B^{Exp.}$ are evaluated by fitting $\sigma_{theor.}$=0.187, 0.0354, 0.0276 mb for NRAPR, SKRA and LNS forces respectively and $\sigma_{exp.}$=9.55 mb, within DCM and V_B is the barrier height of the respective Skyrme forces.

		$\%\Delta V_B = (\Delta V_B^{Exp.}$- $\Delta V_B^{theor.})/V_B\times100$		
S.No.	$\ell(\hbar)$	NRAPR	SKRA	LNS
1	0	7.11	8.20	12.03
2	ℓ_{max}	1.95	1.96	2.31

ergies below the Coulomb barrier. The predictions are made on the basis of neck length, ΔR. Here, the values of ΔR at low energies are extrapolated using second order polynomial *i.e.* ΔR=0.210+0.0911$E_{c.m.}$-0.001$E_{c.m.}^2$, and then cross sections at $E_{c.m.}$=25.0 and 26.0 MeV are predicted with DCM using prefered NRAPR force. The predicted values of cross section at these energies are represented with filled squares as shown in Fig. 6.7 and also reported in Table 6.1.

6.2.3 ICF dynamics

In the above subsections, the behavior of different Skyrme forces has been analyzed for complete fusion process (CF). In this subsection, the possible emergence for incomplete fusion process (ICF) observed at highest energies is explored. In case of incomplete fusion process, the projectile i.e. ^6Li [11] is supposed to break into α and d(deutron). In reference to [13], α has higher probability to interact with target as compare to deuteron. Since the breakup fragment carries a fraction of total energy of projectile, so the new compound system thus formed acquires lower excitation energy as compared to the compound nucleus formed in complete fusion process. In this case, we suppose that beam energy is equally shared by the nucleons of projectile and the nucleon energy of projectile before breakup can be worked out as per Eq. (2.65) of chapter 2. The new projectile with normalized energy fuses with

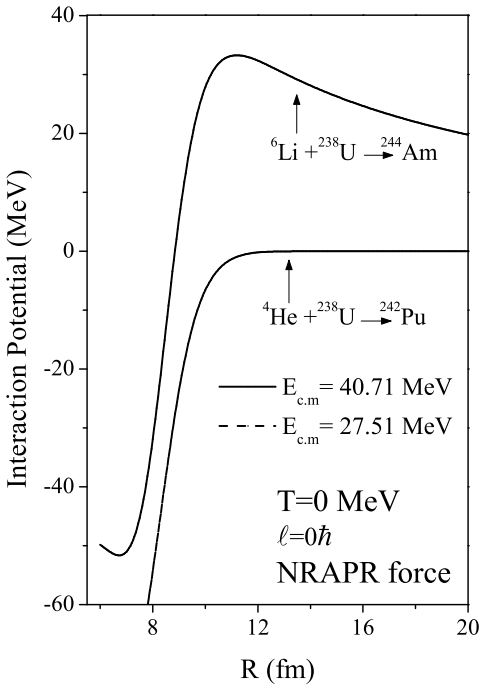

Figure 6.9: Interaction Potential V (MeV) plotted with respect to separation distance R (fm) for $^{6}Li + ^{238}U$ and $^{4}He + ^{238}U$ reactions using NRAPR force.

the target, forming compound nucleus which may decay into corresponding fission fragments.

In view of present work, it is of interest to analyze how barrier characteristic changes due to breakup of projectile. The corresponding scattering potential is calculated at two extreme energies for CF and ICF channels separately at $E_{c.m.}$ = 40.71 MeV and $E_{c.m.}$ = 27.51 MeV respectively using NRAPR force as shown in Fig. 6.9. This figure clarifies that the barrier profile of both the reactions are significantly different. The breakup reaction has low barrier as compare to complete fusion case. This is due to charge reduction in the breakup channel that leads to low Coulomb barrier.

Along with the fitting of data, the behavior of selected forces is also examined in ICF process. The fission cross sections for $^{4}He + ^{238}U$ reaction are estimated by $\sigma_{ICF} = \sigma_{exp}$ - σ_{CF} and compared with calculated cross sections. The calculations are

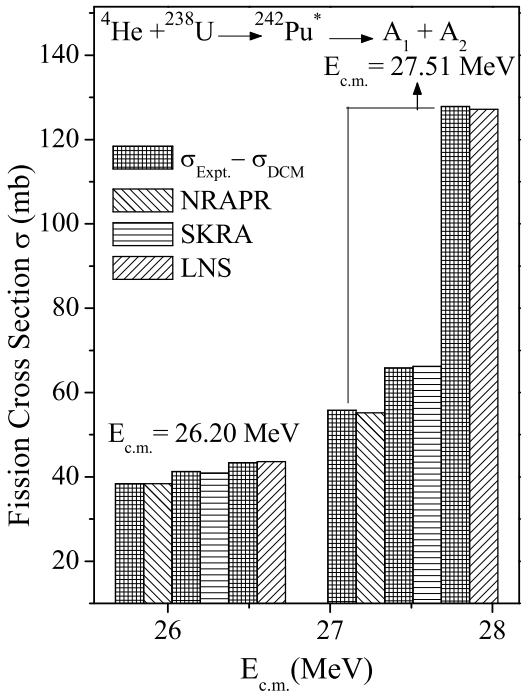

Figure 6.10: Fission cross section for $^4He+^{238}U$ reaction as a function of $E_{c.m.}$ is calculated at extreme energies using NRAPR, SKRA and LNS forces and is compared with σ_{exp} - σ_{CF}.

carried out at highest two energies *i.e.* $E_{c.m.}$= 26.20 and 27.51 MeV with NRAPR, SKRA and LNS forces. The results of ICF are represented by bar graph in Fig. 6.10. It is seen from the figure that the calculated values give close result to σ_{exp} - σ_{CF}. From this graph, we emphasize that suppression in cross section is mainly due to the contribution of ICF process and is in agreement with the conclusions of Dasgupta *et al.* [16].

6.3 Conclusions

In this work, the role of different Skyrme forces is analyzed for compound and non compound nuclear processes using dynamical cluster-decay model. In order to understand the behavior of selected Skyrme interactions (that are assumed to perform better in neutron-rich systems), we have investigated the ^6Li +^{238} U reaction and

the barrier characteristics are compared with earlier studied SIII and GSKI forces. Barrier characteristics show that KDE0v1 is identical to SIII, while NRAPR and SQMC700 are alike GSkI force. Among the selected Skyrme forces, NRAPR, SKRA and LNS forces covering wide range of barrier characteristics, are chosen to illustrate the fission dynamics of $^{244}Am^{*}$. The fission cross sections of $^{244}Am^{*}$ are obtained using NRAPR, SKRA and LNS Skyrme forces over the energy ranging from $E_{c.m.}$ = 27.29 to 40.71 MeV. At higher energies, the calculated fission cross sections start deviating from experimental data and hence suggest the occurrence of fusion suppression, which is addressed in terms of incomplete fusion (ICF) contribution. The ICF calculations are done at $E_{c.m.}$ = 26.20 and 27.51 MeV using same forces and seems to address the difference due to suppression factor. The percentage barrier modifications help to provide useful information about addressal of fusion hindrance phenomena within the DCM. The force with small $\%\Delta V_B$ seems to be better in resolving fusion hindrance phenomena. Less $\%\Delta V_B$ suggests that there is some inbuilt intrinsic barrier modification in the said Skyrme force. Thus, it is evident from ΔV_B variation that NRAPR and its identical SQMC700 and GSkI forces (having barrier characteristics similar to NRAPR) require lesser barrier modifications and can be used as an alternate choice for estimating the nuclear interaction potential. Additionally, the cross sections are also predicted at energies below the Coulomb barrier using NRAPR Skyrme force with in the DCM, for which an experimental verification is called for. In future, a systematic study of variety of reactions may be taken up to strengthen the conclusion regarding appropriate choice of Skyrme forces.

After examining the role of various Skyrme forces in decay dynamics of complete and incomplete fusion processes, it is of further interest to investigate the reaction mechanism in view of isotopic and isobaric (also even-odd) effect, which substantially influence the shell structure of the out going fragments and hence the decay path of the excited compound system. Besides the Skyrme interactions, the proximity 77 potential is used to address the experimental data of evaporation residue and fission

fragments. The results are discussed in chapter 7.

Bibliography

[1] D. Vautherin and D. M. Brink, Phys. Rev C **5**, 626 (1972).

[2] M. Brack, C. Guet and H. B. Hakansson, Phys. Rep. **123**, 275 (1985).

[3] M. Dutra, O. Lourenço, J. S. Sá Martins, and A. Delfino, J. R. Stone, P. D. Stevenson, Phys. Rev. C **85**, 035201 (2012); earlier references therein.

[4] S. Krewald, V. Klent, J. Speth and A. Faessler, Nucl. Phys. A **281**, 166 (1977).

[5] B. K. Agrawal, S. K. Dhiman, and R. Kumar, Phys. Rev. C **73**, 034319 (2006).

[6] R. K. Gupta, R. Kumar, N. K. Dhiman, M. Balasubramaniam, W. Scheid and C. Beck, Phys. Rev. C **68**, 014610 (2003).

[7] G. Kaur, D. Jain, R. Kumar and M. K. Sharma, Nucl. Phys. A **916**, 260-274 (2013).

[8] D. Jain, R. Kumar, M. K. Sharma and R. K. Gupta, Phys. Rev. C **85**, 024615 (2012).

[9] G. Sawhney, M. K. Sharma and R. K Gupta, Phys. Rev. C **83**, 064610 (2011).

[10] M. K. Sharma, S. Kanwar, G. Sawhney, R. K. Gupta and W. Greiner, J. Phys. G: Nucl. Part. Phys. **38**, 055104 (2011).

[11] A. Parihari, S. Santra, A. Pal, N. L. Singh, K. Mahata, B. K. Nayak, R. Tripathi, K. Ramachandran, P. K. Rath, R. Chakrabarti, S. Kailas, Phys. Rev C **90**, 014603 (2014).

[12] R. K. Gupta, M. Balasubramaniam, R. Kumar, N. Singh, M. Manhas, and W. Greiner, J. Phys. G: Part. Phys, **31**, 631 (2005).

[13] G. Kaur and M. K. Sharma, Nucl. Phys. A **884**, 36-50 (2012).

[14] P. D. Stevenson, P. M. Goddard, J. R. Stone and M. Dutra arXiv: **1210.1592v1**, (2012).

[15] R. Kumar, M. Bansal, S. K. Arun and R. K. Gupta, Phys. Rev. C **80**, 034618 (2009).

[16] M. Dasgupta *et. al.*, Phys. Rev. C **70**, 024606 (2004).

Chapter 7

Isotopic and isobaric analysis of Hf^* and Pt^* nuclei

In low energy nuclear reactions, the isotopic effect or N/Z distribution holds the special interest as this degree of freedom imparts useful information regarding the nuclear dynamics. Such effects are not prominent during the evaporation stage but still impart significant and sufficient impact on the overall reaction dynamics. Apart from isotopic effect, the isobaric or Z effect also plays significant role in reaction dynamics via influencing the shell effects of fragments. In view of above mentioned facts, a systematic study of isotopic and isobaric effect is carried out by varying the projectile mass and charge, over a range of incident energies. In the previous chapters, Skyrme interactions are used to probe the reaction dynamics, however, in this chapter nuclear potential is calculated by using the proximity based Prox 77 potential. The analysis is done for $^{170,174}Hf^*$ and $^{170,174}Pt^*$ nuclei using the dynamical cluster decay model.

7.1 Introduction

Recently, an experiment was performed with Ti projectile to examine the low energy regime of Ti+Sn reaction and compare its results with Ca+Sn and Ni+Sn

reactions [1]. The fusion analysis of these reactions was done using CCFULL code. As we know that the decay analysis of excited compound nuclei sheds light on various dynamical processes tangled with the decay mechanism, henceforth, the decay of ^{170,174}Hf*, ^{170,174}Pt* compound systems formed via ^{46,50}Ti+^{124}Sn [1] and ^{58}Ni+^{112,116}Sn [2] reactions respectively are examined in the framework of Dynamical Cluster decay Model (DCM). The analysis of Yb* compound system formed via Ca+Sn reaction was carried out earlier [3] and the focus of present study mainly lies in the relative analysis of the decay of Hf* and Pt* compound systems formed via Ti+Sn and Ni+Sn reactions respectively. In the decay process, the potential energy landscape is an important ingredient that is enriched with an ample information regarding the macroscopic and microscopic effects of the composite system and the constituent nuclei [4]. The topography of potential surface is sensitive to the nuclear charge, N/Z ratio and deformation effects of the system [5, 6]. Such effects have been studied for actinide series which show substantial variations in potential energy structure [7, 8]. The potential energy for actinide nuclei exhibit a gradual change from single-humped to double humped mass distribution with an increase in Z-values. Now it will be of further interest to analyze the impact of nuclear charge and N/Z ratio in relatively lighter nuclei. For the purpose, decay of Hf* and Pt* nuclei is studied by exploring the isotopic and isobaric effect of these systems. Making the use of structural information, the fusion evaporation and fusion-fission cross-sections are calculated for wide range of energies (or equivalently temperature), via optimizing the neck length "ΔR". Further employing the shape elongation via neck length ΔR, time scale of the fission fragments is calculated for Hf and is compared with the time scale of light charged particle. The time taken for compound nucleus to decay is primarily depends on the statistical as well as dynamical properties of the fissioning nuclei. For the calculations of the fission time, deformations, elongation (neck length), Z and A of the fission fragments are used as input in semi-statistical approach [9]. The fission time for heavier system comes out of the order of zepto

second, which is in agreement with Refs. [10–12].

The decay process is studied using the dynamical cluster-decay model [7, 13–15] which treats different decay modes such as evaporation residue(ER), intermediate mass fragments (IMF), heavy mass fragments (HMF)and the fission fragments on equivalent footing. Within DCM, the dynamical evolution of nuclei is inferred by considering the potential energy structure, temperature and deformation effects. The neck length parameter ΔR in DCM helps to examine the flow of nucleons via neck formation that consequently induce the barrier modifications, influence the cross-sectional yield and helps to interpret the time scale of exit channel. The calculations done after inclusion of deformation show that isotopic effect is more prominent for Hf^* nuclei as compared to Pt^*. The heavy mass fragments and fission fragments are evident in both the cases, but the contribution of HMF's is relatively small for Pt^* case. On the contrary, for the spherical case isotopic and isobaric effect is almost negligible in the decay analysis. Further, evaporation cross-sections of Hf^* [1] and Pt^* [2] nuclei are addressed by optimizing the neck length over wide range of excitation energies. The calculated results give decent agreement with respective experimental data. However, the fission cross sections of Hf^* and Pt^* nuclei show suppression at higher temperature even after the inclusion of HMF. The deviation of fission cross sections at highest temperature of Hf^* and Pt^* nuclei advocate the possible presence of non-compound nucleus channel [1]. Finally, using the optimized ΔR, the timescale of fission fragments is calculated, which comes out of the order of (0.7-1)$\times 10^{-21}$s while for light charged particle it is observed to be (0.5)$\times 10^{-21}$s. This suggests that light particles are emitted at earlier stage as compared to fission fragments, suggesting that higher the ΔR value lesser will be the time scale [11, 12] and vice versa. The corresponding calculations and results are presented in section 7.2. Finally, the outcomes of work is concluded in section 7.3

7.2 Calculations and results

The detailed study on the decays of Hf* and Pt* nuclei is carried out using the dynamical cluster-decay model. The motive of this study is (i) to analyze the structural properties of decaying $^{170-174}$Hf* and $^{170-174}$Pt* nuclei in view of deformation, isotopic and isobaric effect,(ii) evaluate the cross-sectional yields of excited compound nuclei by optimizing the neck length ΔR at energies (or equivalent temperatures) around the Coulomb barrier. The ΔR provides the information about the neck formation between the nascent clusters and in turn (iii) helps to estimate the time scale of fission and evaporation residue channels.

The fragmentation potential and preformation probability are the main constituents of dynamical cluster-decay model that provide the much needed information about the structure of decaying fragments. As the behavior of fragmentation potential is better explained via preformation probability, P_0. Therefore, the preformation probability obtained from the fragmentation potential is analyzed for Hf* nuclei varying from A_{CN} = 170 - 174. The analysis is done at excited compound nucleus temperature T $\approx$ 2.0 MeV, for the spherical choice of fragmentation at ℓ=ℓ_{max}. The comparison of $^{170-174}$Hf* nuclei is done by consecutively adding one neutron in ^{46}Ti projectile nucleus keeping the target nucleus same. Subsequently, the role of neutron excess and even-odd mass of the nuclei is analyzed in reference to decay path of excited systems. The preformation probability of even mass ^{170,174}Hf* along with their immediate odd mass ^{171,173}Hf* nuclei are depicted in Fig. 7.1 for spherical choice of fragmentation. The figure illustrates that (i) fission forms the dominant decay mode of ^{170,174}Hf* nuclei at higher ℓ values, whereas the contribution of competing decay modes such as heavy mass fragments (HMF) and light mass fragments (LMF) is rather small. (ii) A slight transition is observed in the encircled fission region that changes from asymmetric to symmetric pattern for neutron rich cases. From this figure, it is evident that for spherical fragmentation no significant variation is observed in preformation probability of $^{170-174}$Hf* nuclei.

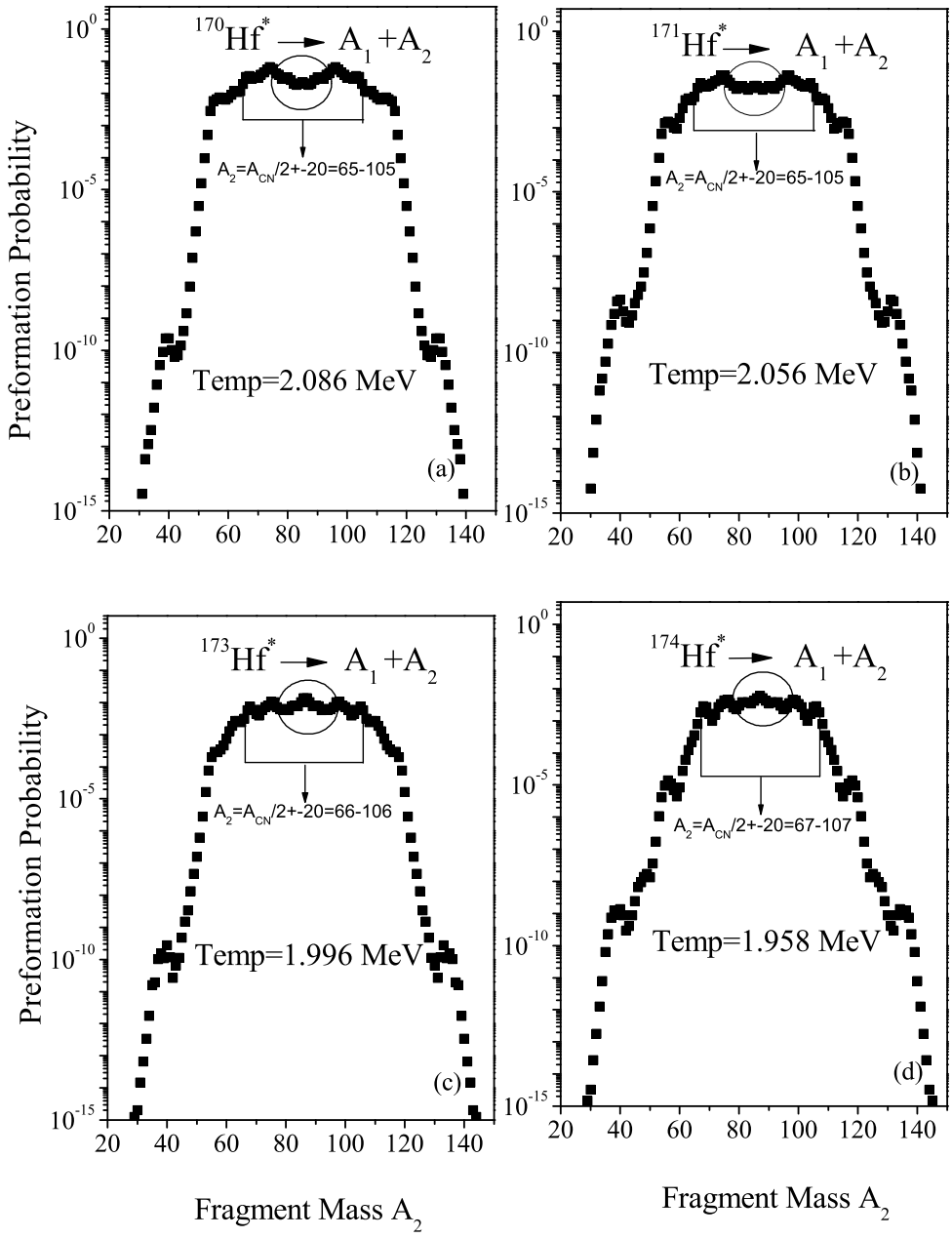

Figure 7.1: Variation in preformation probability plotted against fragment mass A_2 analyzed for (a) $^{170}Hf^*$, (b) $^{171}Hf^*$, (c) $^{173}Hf^*$ and (d)$^{174}Hf^*$ nuclei at temperature T $\approx$ 2.00 MeV. These calculations are done for the spherical case.

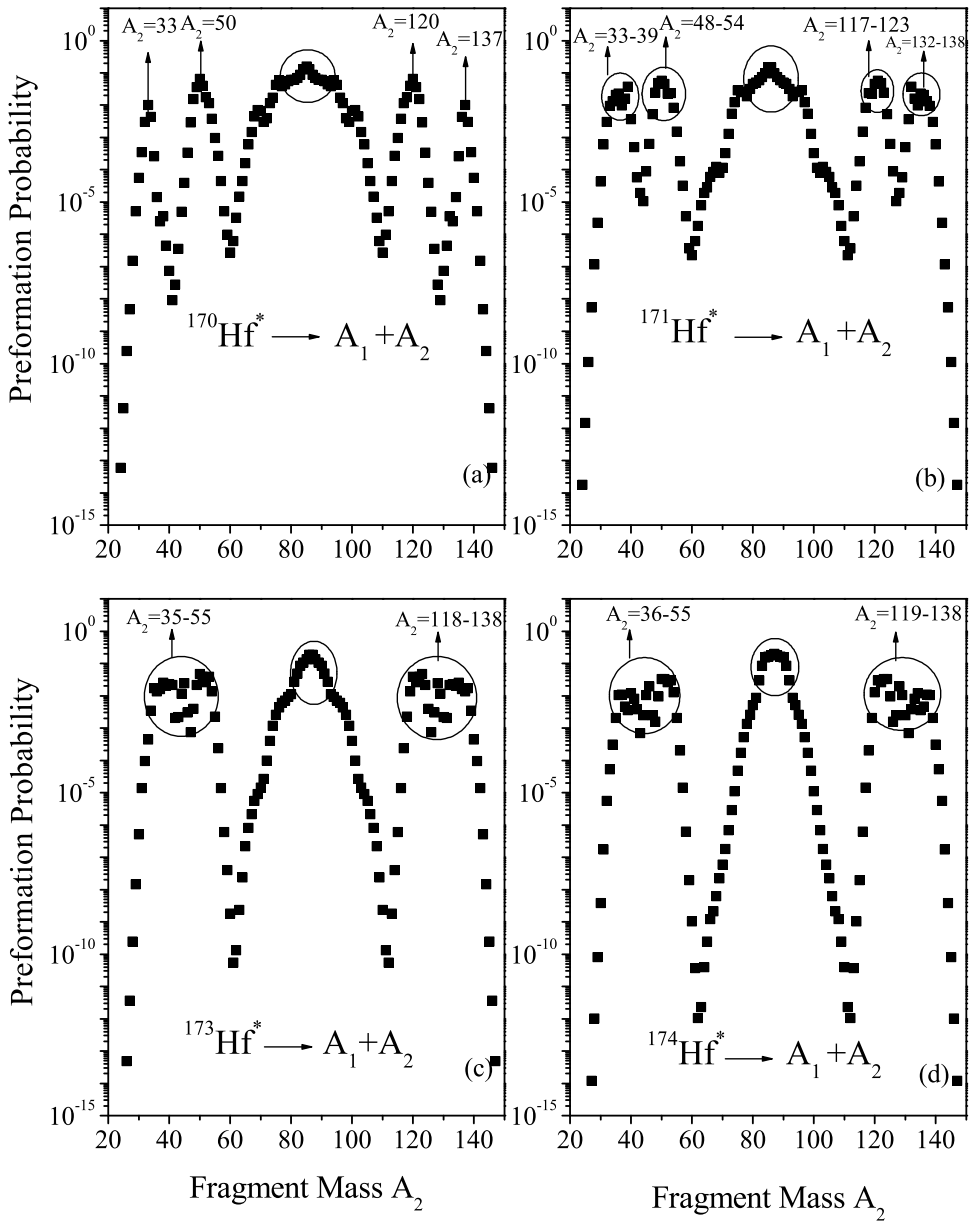

Figure 7.2: Same as Fig. 7.1 but for deformed nuclei.

When the deformations are added, the preformation probability as shown in Fig. 7.2 depicts an abrupt variation in the structure of $^{170-174}$Hf* nuclei. From Fig. 7.2, it is noticed that (i) for ^{170}Hf* nucleus, two asymmetric peaks near A_2 = ^{33}P and ^{50}Ti contribute in heavy mass region, along with evident contribution of the fission fragments, (ii) the two asymmetric peaks tend to merge into a single asymmetric peak with the increase in the number of neutrons as we move from neutron deficient ^{170}Hf* to neutron rich ^{174}Hf* nuclei, (iii) the contribution of clusters in heavy mass region increases with the increase in neutron excess. This is because the addition of one neutron changes the nucleonic distribution and consequently different fragments having different deformation effects are minimized in the decay channel, which on the other hand affect the preformation probability of the decaying nuclei. In other words, the deformation effects lead to change in the mass and Z - distribution of decaying clusters as one moves from ^{170}Hf* to ^{174}Hf* nucleus, (iv) it is observed that deformations (β_{2i}) are varying from 0.16 -0.35 on moving from ^{170}Hf* to ^{174}Hf* nuclei as a result, the highly deformed fragments lie in the bottom region due to instability against the deformation effect, (v) However, the clusters appearing in heavy mass region are the ones in the neighborhood of magic or near magic shell nuclei, where highest peak corresponds to Z=22 and N=28 cluster, which emerges consistently in all the decaying $^{170-174}$Hf* nuclei, (vi) along with the heavy mass region, fission region also exhibit noticeable variation in terms of fission width. It is seen that symmetric fission region becomes narrow for neutron rich fragments in the decay channel. Conclusively, one can say that neutron excess (or even-odd nuclear mass effect) accompanied with deformation effects show significant variation on the fragmentation structures of decaying $^{170-174}$Hf* nuclei.

Further, the same analysis is done for ^{170,174}Pt* nuclei as shown in Fig. 7.3. The study clearly indicates that (i)symmetric fission persists in both the decaying systems, with and without including the deformation effects (ii) for the deformed case, asymmetric peaks in heavy mass range also contribute along with fission clusters.

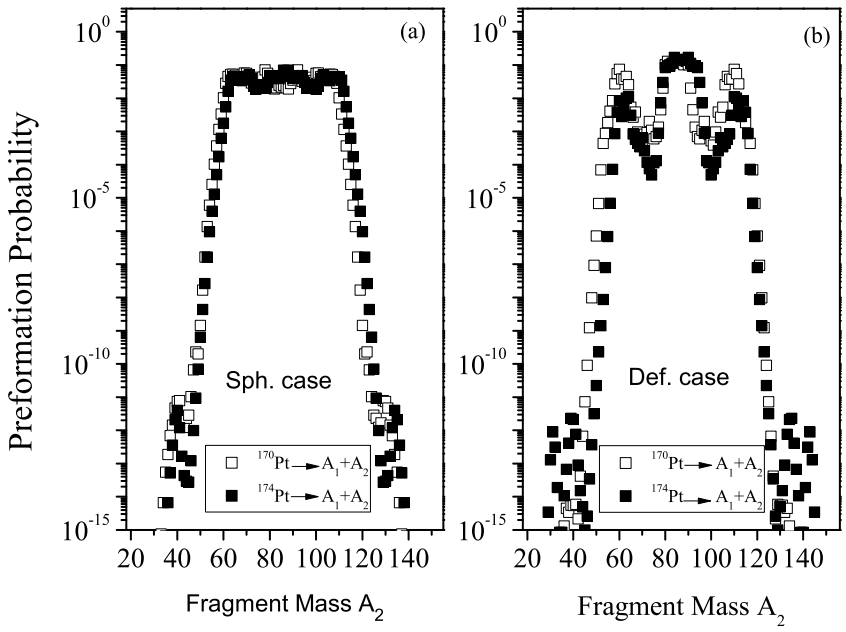

Figure 7.3: Preformation probability vs fragment mass A_2 estimated at T=1.611 MeV for $^{170,174}Pt^*$ nuclei. Figure (a) corresponds to spherical case and figure (b) corresponds to deformed case.

Here, the clusters/fragments lying in the asymmetric peak region have proton magic shell closure, for instance the lighter cluster A_2=60, Z_2=28, and its complimentary heavier cluster A_2=110, Z_2=50 are proton magic with near spherical configuration i.e. $\beta_{2i} < 0.02$ (iii) the clusters appearing in the dip region are the deformed ones having $\beta_{2i} \approx 0.14$, hence lie in the valley region. As the magnitude of deformations in Pt case is relatively smaller, therefore spherical and deformed preformation distributions look similar.

Besides this, no noticeable effect of neutron excess as well as even-odd masses of parent nuclei is observed for Pt* systems. Thus, comparing Figs. 7.1, 7.2, and 7.3, one can say that deformation plays an effective role in the decay dynamics of Hf* and Pt* systems. However, for the Hf* nuclei the neutron excess effect is more prominent when deformations are taken into consideration. While the spherical cases of both the nuclei exhibit similar decay pattern (symmetric fission).

After analyzing the neutron excess or isotopic effect for Hf* and Pt* nuclei,

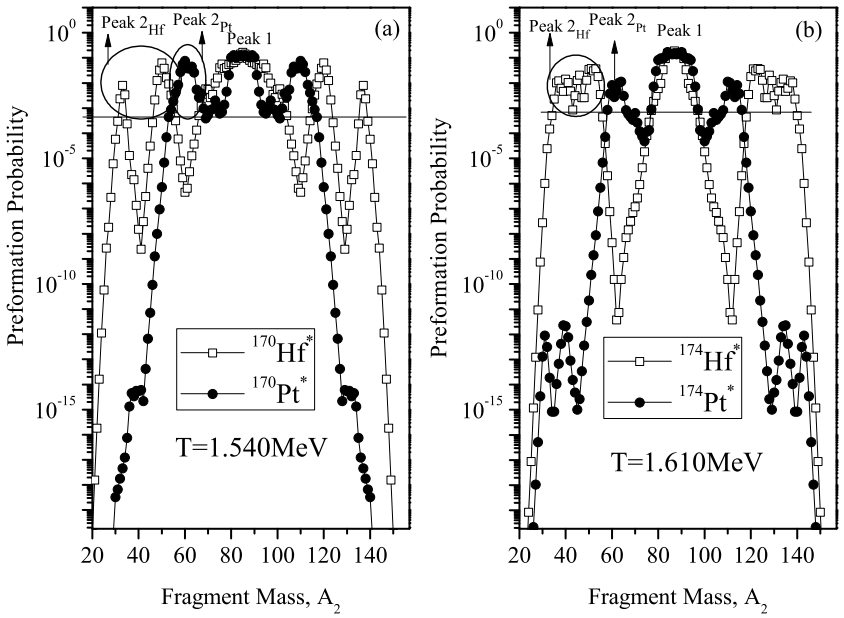

Figure 7.4: Preformation potential vs fragment mass A_2 explored (a) for ^{170}Hf*, ^{170}Pt* and (b) for ^{174}Hf*, ^{174}Pt* nuclei at their respective common temperatures.

an effort is made to study the isobaric or the Z-effect in the decay process. Fig. 7.4 interpret the preformation yield of nuclei having different Z_{CN} and same A_{CN} values, where superscript CN represents compound nucleus. The study is carried out at common temperature and angular momentum value for Hf* and Pt* systems, for deformed choice of fragmentation and the relative contribution of heavy mass and fission fragments is analyzed. The result shows transient effect of Z_{CN} on the decay structure of different compound systems. The increasing Z_{CN} has its influence on the macroscopic part of the fragmentation potential, which consequently affects the preformation probability of the decay channels.

From Fig. 7.5, one can see that the contribution of fission window and the asymmetric peaks of heavy mass region change significantly with increase in the Z_{CN} value. The contribution of heavy mass cluster with respect to fission is different for both Hf* and Pt* nuclei. It is apparent from the ratio of peak$_2$/peak$_1$ (i.e. ratio of asymmteric/symmteric fission) as plotted in Fig. 7.5 for both the compound

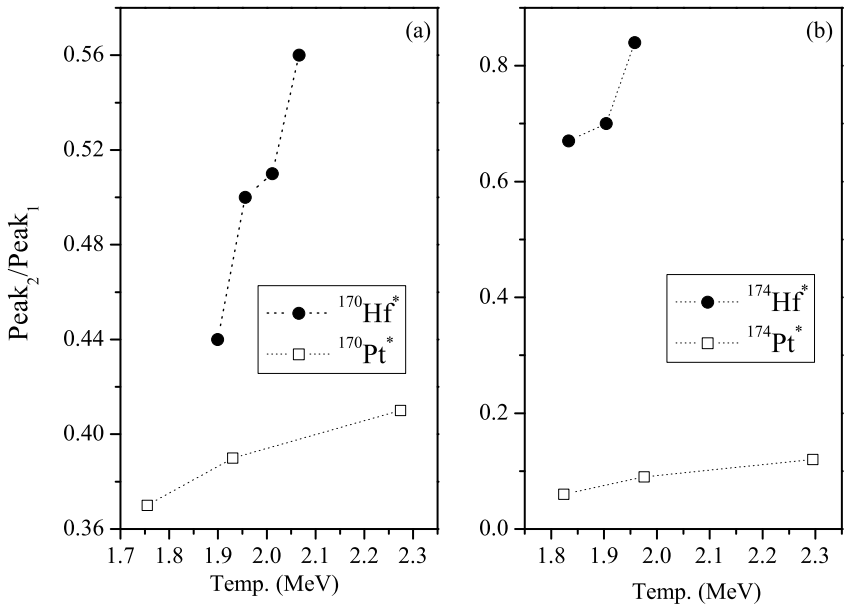

Figure 7.5: Variation in $Peak_2/Peak_1$ with respect to temperature for (a) $^{170}Hf^*$, $^{170}Pt^*$ and (b) $^{174}Hf^*$, $^{174}Pt^*$

.

nuclei. Since the fission cross-sections are available at higher incident energies [1], therefore, the ratio of the peaks is evaluated at the temperatures corresponding to higher energies. Here, the two asymmetric peaks appearing at $A_2 = 33$ and $A_2 = 50$ for ^{170}Hf case are considered as single $peak_2$, while fission mass region is chosen as $peak_1$. It may be noticed from Fig. 7.5 that $peak_2/peak_1$ ratio increases with increase in the temperature. The increasing trend is same for Hf* and Pt* systems but its magnitude is relatively higher for Hf* nucleus(lower Z_{CN} case).

Apart from isotopic and isobaric effect, the variation of summed up preformation probability is examined as a function of angular momentum ℓ for ^{170}Hf* nucleus at temperature T= 1.470 MeV, see Fig 7.6. It is clearly evident that light particles are favorable at lower angular momentum values, while the fission dominates over higher ℓ-values. The result is independent of energy, temperature, isotopic and isobaric nature of the compound system and is true for the decaying systems ^{170,174}Hf* and ^{170,174}Pt* (not shown here to avoid repetition). Further, the penetration probability

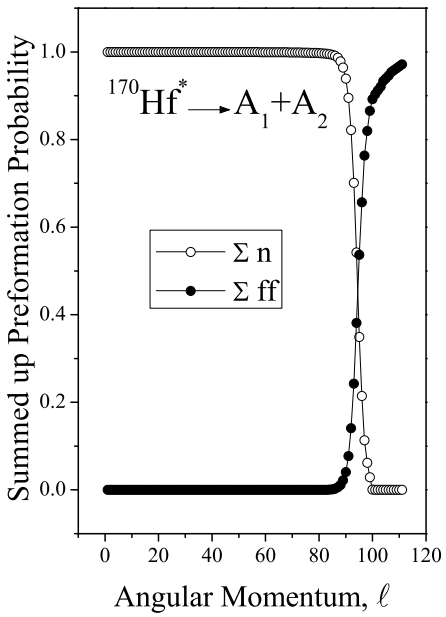

Figure 7.6: Summed up preformation probability as a function of angular momentum ℓ analyzed at T= 1.047 MeV for $^{170}Hf^{*}$ nucleus.

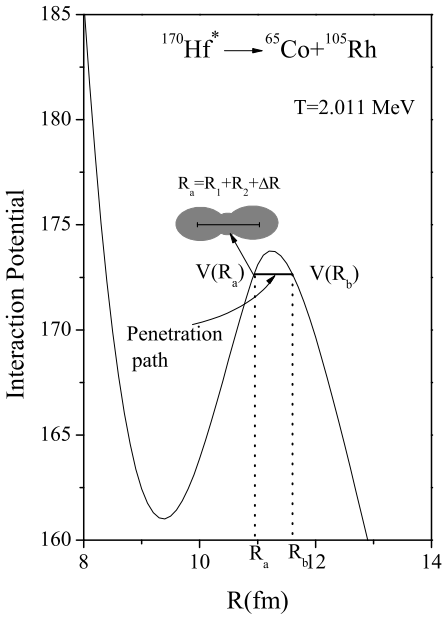

Figure 7.7: Interaction potential plotted against range R(fm) for asymmetric fission of ^{170}Hf* nucleus.

is estimated through the interaction barrier V(R) shown in Fig. 7.7 for fission channel i.e. ^{170}Hf$^{*}\rightarrow^{65}$Co+^{105}Rh at ℓ_{max}. The figure clearly illustrates the entrance (R_a) and exit (R_b) points of the barrier where V(R_a)=V(R_b)=Q_{eff}. At each angular momentum ℓ value, the penetrability P of the decaying fragments is eventually calculated using Eq. (2.54) of Chapter 2.

After obtaining the values of P_0 and P for decay channel, further study has been done to address the cross sections of Hf* and Pt* nuclei at temperatures corresponding to energies around the Coulomb barrier. The fusion evaporation cross-sections of Hf* and Pt* nuclei are obtained by optimizing the value of neck length parameter ΔR. It is important to account the contribution of ΔR within the decay process because the compound system undergoes shape elongation by generating neck between the nascent fragments [10–12,16,17]. The inclusion of neck between the dinuclear system provides space for the unrestricted flow of nucleons between the nuclei and open up the doorway for most prominent exit channels by modifying their interaction barrier. In this way, the neck length ΔR governs the flow of mass drift and provides barrier modification effect.

Optimizing the value of ΔR, the fusion evaporation cross- sections of xn (x=1,2,3,4) particles are calculated for $^{170,174}Hf^{*}$ and $^{170,174}Pt^{*}$ nuclei over the temperature ranging from T = 1.335-2.066 and 1.283-1.810 MeV respectively. The calculated cross sections are compared with available experimental data as tabulated in Table 7.1. This table shows that DCM based calculations address the experimental data nicely for all the excited nuclei. The magnitude of ΔR increases with increase in temperature as seen from Fig 7.8(a), which on the other hand governs barrier adjustment, in terms of barrier modification parameter ΔV_B. The analysis of ΔV_B is made for ^{170,174}Hf* nuclei and is shown in Fig 7.8(b) as a function of temperature T(MeV). This figure illustrates that magnitude of ΔV_B decreases with increase in temperature. The magnitude of ΔV_B is relatively large for ^{170}Hf* nucleus which reflects the requirement of more barrier modification as compare to ^{174}Hf* nucleus. It

Table 7.1: Comparison of evaporation residue cross sections of DCM with experimental data of ^{170,174}Hf* and ^{170,174}Pt*. The values of optimized ΔR of respective system are also shown below.

Y= $^{170}Hf^{*}$				Y= $^{174}Hf^{*}$			
Temp. (MeV)	ΔR (fm)	σ_{DCM} (mb)	$\sigma_{Expt.}$ (mb)	Temp. (MeV)	ΔR (fm)	σ_{DCM} (mb)	$\sigma_{Expt.}$ (mb)
1.470	1.124	0.12	0.14	1.335	1.02	0.040	0.042
1.506	1.220	0.675	0.68	1.394	1.186	0.609	0.614
1.546	1.311	2.45	2.50	1.413	1.300	3.38	3.39
1.580	1.398	7.60	7.82	1.467	1.398	10.88	11.24
1.613	1.483	20.11	20.85	1.503	1.490	33.90	34.22
1.657	1.540	39.86	40.53	1.537	1.598	87.88	88.00
1.684	1.619	68.86	69.39	1.588	1.650	144.00	145.98
1.734	1.692	190.0	191.68	1.637	1.699	201.5	208.60
1.780	1.728	126.0	126.70	1.684	1.742	280.01	281.18
1.825	1.770	253.78	254.40	1.730	1.750	317.00	317.04
1.871	1.796	306.00	307.38	1.775	1.776	362	363.34
1.899	1.794	296.47	297.59	1.833	1.802	440	440.00
1.956	1.823	382.24	383.59	1.904	1.798	465.24	466.47
2.011	1.870	462.23	463.46	1.958	1.830	515.0	525.98
2.066	1.860	444.00	448.71	-	-	-	- -
Y= $^{170}Pt^{*}$				Y= $^{174}Pt^{*}$			
1.140	1.600	1.90	1.94	1.283	1.700	6.82	6.94
1.543	1.627	23.1	23.57	1.611	1.865	35.5	35.61
1.739	1.526	16.60	16.86	1.810	1.870	40.00	41.26

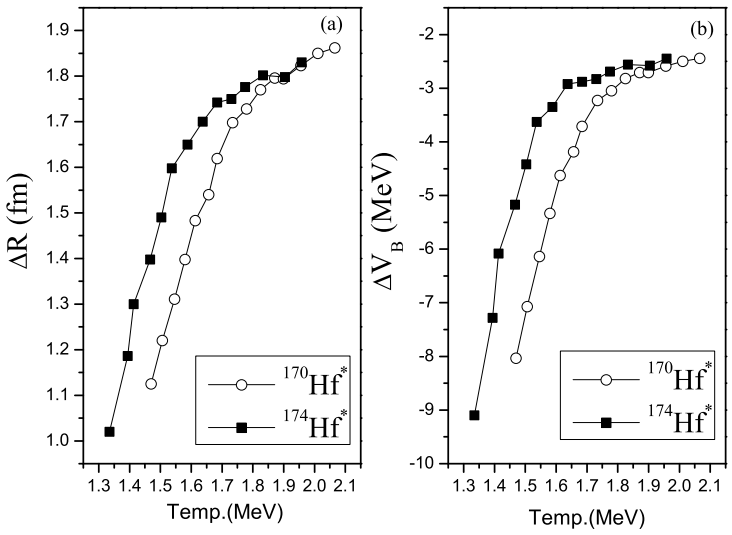

Figure 7.8: Variation in ΔR and ΔV_B as a function of temperature T(MeV) is plotted for ^{170,174}Hf* nuclei

is pertinent to mention that the increasing magnitude of ΔR (see Table 7.1) reduces the corresponding ΔV_B. The higher value of neck length ΔR for ^{174}Hf* nucleus imparts lesser barrier modification in comparison to ^{170}Hf* nucleus. From these observations, effective role of neck formation and consequently the barrier modification is analyzed in the decay process.

Along with σ_{ER}, the fusion fission(ff) cross sections σ_{ff} of Hf* and Pt* nuclei are calculated within the DCM approach. From Ref. [1], σ_{ff} of ^{170,174}Hf* nuclei are extracted as σ_{ff}= σ_{CCFull}-$\sigma_{expt.}$ while the σ_{ff} of Pt* nuclei are taken from Ref. [2]. The motive behind addressing the fission cross sections of Pt* and Hf* nuclei is (i) to make comparative study of their fission fragmentation and (ii) to obtain the value of optimized ΔR, which is further used to determine the time scale of fission fragments.

The σ_{ff}^{DCM} of ^{170}Hf* nuclei gives decent agreement with experimental data at temperature T=1.899,1.956,2.011 MeV, except for T=2.066 MeV. At highest temperature, fission cross sections show significant deviation from experimental data. Since the contribution of asymmetric peaks or heavy mass fragments (HMFs) is significant particularly at higher temperature (see Fig. 7.5), therefore DCM based

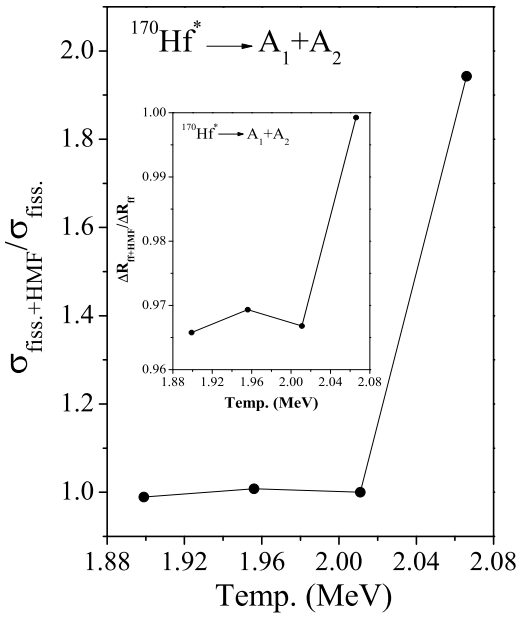

Figure 7.9: Variation in $(\sigma_{fiss.+HMF})$ / $(\sigma_{fiss.})$ with respect to T(MeV) is studied for ^{170}Hf* nucleus.

calculations demand the inclusion of heavy mass component in the total fission cross sections. The cross sections corresponding to HMF's are determined at same ΔR as that for fission fragments. The ratio of $(\sigma_{fiss.+HMF})$ / $(\sigma_{fiss.})$ is depicted in Fig. 7.9. The figure represents that the variation of $(\sigma_{fiss.+HMF})$ / $(\sigma_{fiss.})$ remains the same at all temperature, except at higher T=2.066 MeV, where the contribution of (fiss.+ HMF) fragments is much higher indicating major contribution from HMF window. Thus for the better addressal of experimental data at highest temperature, the fission fragments along with the HMFs are taken into consideration. Also, it is observed that the change in $(\sigma_{fiss.+HMF})$ / $(\sigma_{fiss.})$ follows the similar trend as that of the $\Delta R_{fiss+HMF}/\Delta R_{fiss}$, shown in the inset of Fig.7.9. The comparison of theoretical calculations with the measured data for ^{170,174}Hf* and ^{170,174}Pt* nuclei is shown in Table 7.2. From Table 7.2, it is evident that even $\sigma_{fiss.+HMF}$ could not address the experimental data for ^{170,174}Pt* nuclei. The deviation in the Hf and Pt fission cross sections at higher temperatures indicate the contribution of nCN processes. As Z_1Z_2 for Hf* and Pt* reactions is ≥ 1000, therefore it seems that some

Table 7.2: Same as Table 7.1 but for fission cross sections.

Y= $^{170}Hf^*$				Y= $^{174}Hf^*$			
Temp. (MeV)	ΔR (fm)	σ_{ff+HMf} (mb)	$\sigma_{Expt.}$ (mb)	Temp. (MeV)	ΔR (fm)	σ_{ff+HMf} (mb)	$\sigma_{Expt.}$ (mb)
1.899	1.242	73.2	75	1.833	1.247	118	118
1.956	1.265	74.4	76	1.904	1.330	172.8	194
2.011	1.281	86.2	87	1.958	1.336	189.4	225
2.066	1.339	175.6	191				
Y= ^{170}Pt				Y= ^{174}Pt			
1.755	1.269	157.2	211.8	1.824	1.270	185.2	266.58
1.930	1.277	144.4	264.9	1.976	1.283	184	295.75
2.274	1.298	120.8	448.4	2.295	1.296	161.6	456.66

nCN processes compete at higher temperatures [1].

As discussed earlier, the preformation probability provides an idea of the fragmentation structure of decaying isotopic and isobaric nuclei and provide essential information about the evolution of the decay process. This study on the other hand gives assess to estimate the dynamical aspects in the decay process. For further analysis, the dynamical properties of the decaying nuclei are calculated in terms of (a) distance between the two nascent fragments, (b) relative velocities and (c) time scale of fission fragments and the light charged particle.

The theoretical calculations are done by using simple classical concept, where Coulomb repulsion is meant to produce kinetic energy among the binary fragments, which on the other hand give assess to fission velocities [16,18]. As the kinetic energy of the fragments depends upon the separation distance between them. Therefore, the separation distance of decaying nuclei is estimated as a sum of their radii and the optimized neck length ΔR formed between them. The separation distance D as expressed in Ref. [9] is represented by R_b where V(R_b)= V(R_a) and R_a is given by

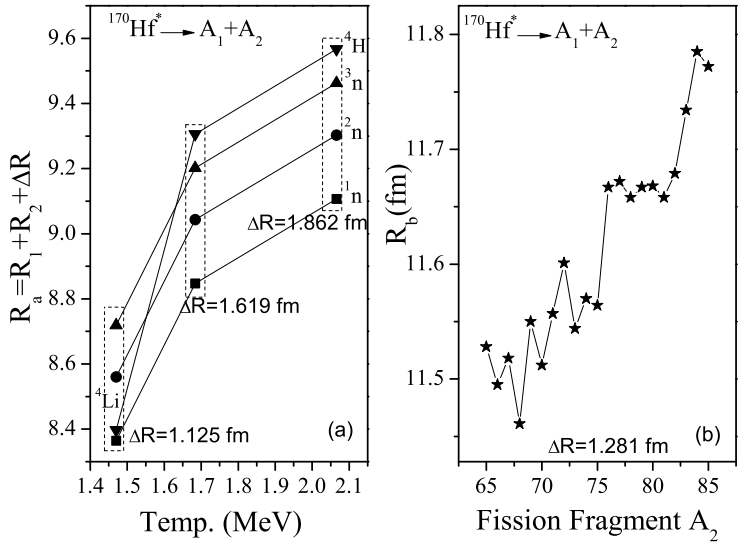

Figure 7.10: (a)Distance as a function of temperature T(MeV) for (a) light particles and (b) fission fragments A_2 is examined for $^{170}Hf^{*}$ nucleus.

Eq. (2.57) of Chapter 2.

For light charged particles emitted during the decay of $^{170}Hf^{*}$ nuclei, the variation of R_a (fm) as a function of temperature is analyzed at T = 1.470, 1.684 and 2.066 MeV, shown in Fig 7.10(a). The observation manifests that R_a increases with increase in temperature, having higher magnitude for ^{4}H followed by 3n,2n and 1n fragments. As the temperature increases, the probability of ^{4}H and other light mass fragment increases consistently. The ^{4}Li minimized at lowest temperature reflects small shape elongation due to the deformation effect with respect to other emitted fragments. The graph clearly demonstrates that R_a of the composite system increases consistently with the increase in T (MeV) and the fragments mass A_2. The analysis for fission fragments is done at temperature T=2.011 MeV. For comparative basis, the change in R_b (fm) w.r.t fragments mass A_2 varying from A_2 =$A_{CN}/2$ - 20 to $A_{CN}/2$ is presented in Fig 7.10(b). The analysis reveals that the separation distance for binary fragments is higher for symmetric channels as compare to asymmetric ones, due to increase in the mass number A_{CN}. The variations in R_b values seen in the graph originate due to the deformation effects which impart huge significance in the dynamics of nuclear systems. The total kinetic energy as

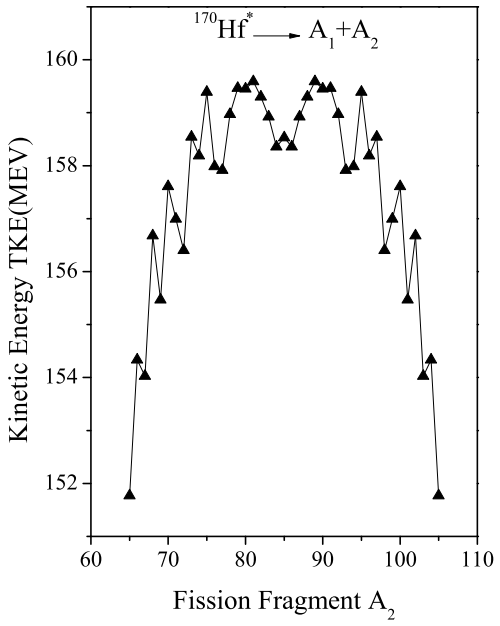

Figure 7.11: Kinetic energy distribution of fission fragment A_2 studied for $^{170}Hf^{*}$ nucleus.

given in Eq.(2.58) of Chapter 2 is estimated at temperature T=2.011 MeV, at R_b values shown in Fig. 7.10(b). The variation in kinetic energy distribution of fission fragments as shown in Fig 7.11, clearly demonstrates that increasing Z_1Z_2 value enhances the competition between the repulsive Coulomb potential and the attractive surface tension effects. As a result, the heavier fragments are more fissile than the lighter one. The variation of TKE follows the same trends as observed in [19], however, the structure appears due to the influence of R_b or equivalent deformations on TKE (see Fig.7.10).

In Fig. 7.12(a), the velocity of fission fragments as per Eq. (2.59) of Chapter 2 is determined for fragment A_2 in mass range A_2=$A_{CN}/2$ - 20 to $A_{CN}/2$. It is seen that lighter fragments travel with higher velocity as compares to the heavier one, following the momentum conservation law. Using the distance and the velocity relationship, the timescale of fission fragments A_2=65-85 is evaluated, and the observation is displayed in Fig. 7.12(b). Here, one can see that time scale is of the order of τ= 10^{-21}, and it increases with increase in the fragment mass. The observation is in

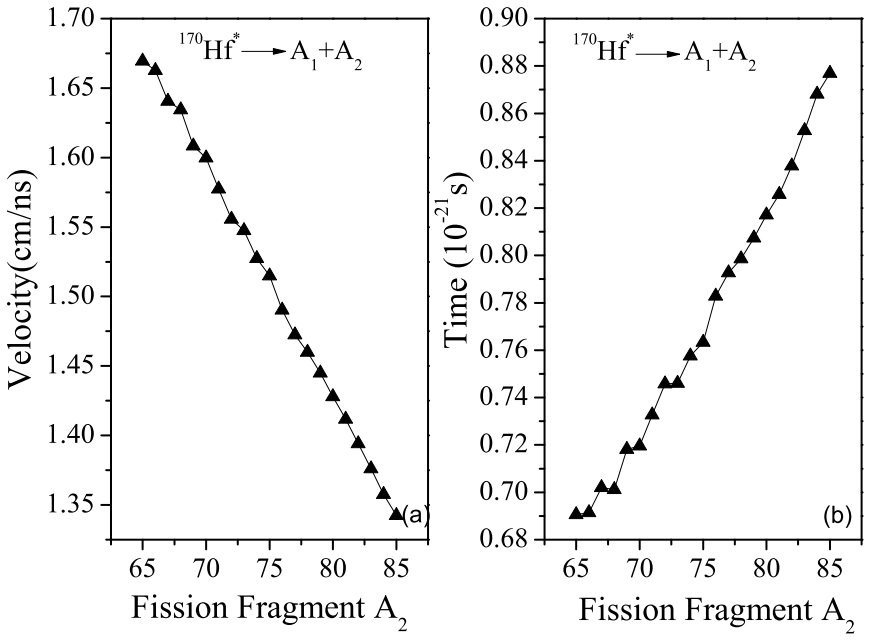

Figure 7.12: (a) Velocity and (b) fission time scale as a function of fragment mass A_2 is studied for ^{170}Hf* nucleus.

agreement with Refs. [10–12,20]. Further calculations are done to compare the time of lightest charged particle i.e. ^{4}H minimized in DCM calculations in the decay of ^{170}Hf*. The time scale for LP, $\tau_{LP} \approx 0.52 \times 10^{-21}$ s while the fission time scale is $\tau_{ff} \approx 1 \times 10^{-21}$s. This means that emission of light particle takes place at early stage as compared to fission fragments Ref. [21]. It implies that higher the ΔR value, lesser will be the time scale Ref. [12].

It is observed that trend of distance R_b(fm), TKE, velocity and time scale remains the same for ^{174}Hf, ^{170}Pt and ^{174}Pt systems at different temperatures as well, while the slight change in their magnitudes is noticed. For the isotopes, magnitude of time scale increase with increase in A_{CN}, while for isobars it decreases with increase in Z_{CN}.

7.3 Conclusions

An extensive study on the decay dynamics of ^{170,174}Hf*, and ^{170,174}Pt* nuclei is done in the vicinity of their respective Coulomb barriers. The analysis shows that (i) isotopic effect is more prominent in ^{170,174}Hf* nuclei as compare to ^{170,174}Pt* nuclei, (ii) The spherical fragmentation shows symmetric fission distribution for all studied nuclei, and clusters in heavy mass region start appearing in, after the deformation effects are included. The contribution of heavy mass fragments (HMF) cross section dominates for Hf* systems, (iii) the effect of odd-even masses accompanied by deformations impart significant influence on the structures of Hf* systems, (iv) isobar reflects the equivalent transition in the potential energy structure of ^{170}Hf*, $^{170}Pt^*$ and ^{174}Hf*, ^{174}Pt* systems, indicating the role of Z_{CN} on the fragmentation path. The fission cross sections at higher temperature show suppression in the calculated values even after the inclusion of HMF. Henceforth, it suggests the possible presence of some nCN channel at higher temperatures. Finally making use of above information, the dynamical properties of fissioning nucleus ^{170}Hf* are analyzed, wherein the velocities of fission fragments and the dynamical time scale of fission fragments are calculated. The time scale of lighter fragment minimized in DCM is compared with fission time scale, which in turn suggest that the emergence of lighter fragments is faster as compared to the fission fragments.

After examining the reaction dynamics of variety of compound nuclei from fusion and subsequent decay dynamics, the overall the analysis is summarized in chapter 8.

Bibliography

[1] J. F. Liang, J. M. Allmond, C. J. Gross, P. E. Mueller, D. Shapira, and R. L. Varner, Phys. Rev. C **94**, 024616 (2016).

[2] K. T. Lesko, W. Henning, K. E. Rehm, G. Rosner, J. P. Schiffer, G. S. F. Stephans, B. Zeidman and W. S. Freeman, Phys. Rev. C **34**, 2155 (1986).

[3] D. Jain, M. K. Sharma, Rajni, R. Kumar, and R. K. Gupta, Eur. Phys. J. A **50**, 155 (2014).

[4] K. H. Schmidt, B. Jurado, http://arxiv.org/abs/1804.10421v1, (2018).

[5] M. Kaur, R. Kumar, and M. K. Sharma, Phys. Rev. C **85**, 014609 (2012).

[6] R. Mittal, D. Jain, and M. K. Sharma, Nucl. Phys. A **968**, 436-452 (2017).

[7] N. Grover, G. Kaur, and M. K. Sharma, Phys. Rev. C **93**, 014603 (2016).

[8] Hemdeep, S. Chopra, A. Kaur, and R. K. Gupta, Phys. Rev. C **95**, 014609 (2017).

[9] J. L. Rodriguez-Sanchez *et. al*, Phys. Rev. C **91**, 064616 (2015).

[10] J. Cabrera et al, Phys. Rev. C **68**, 034613 (2003).

[11] D. Jacquet, M. Morjean, Prog. Part. Nucl. Phys. **63**, 155 (2009).

[12] K. Ramachandran et. al, Pramana-J Phys. **85**, 335-343 (2015).

[13] R. K. Gupta, M. Balasubramaniam, R. Kumar, N. Singh, M. Manhas and W. Greiner, J. Phys. G: Nucl. Part. Phys. **31**, 631 (2005).

[14] A. Kaur, S. Chopra, and R. K. Gupta, Phys. Rev. C **90**, 024619 (2014).

[15] S. Chopra, A. Kaur, Hemdeep, and R. K. Gupta, Phys. Rev. C **93**, 044604 (2016).

[16] B. D. Wilkins, E. P. Steinberg, and R. R. Chasman, Phys. Rev. C **14**, 1832 (1976).

[17] A. Szanto de Toledo, B. V. Carlson, C. Beck and M. Thoennessen, Phys. Rev. C **54**, 3290 (1996).

[18] M. Caamañ*o et. al*, Phys. Rev. C **88**, 024605 (2013).

[19] K. Sandhu, G. Kaur, M. K.Sharma, Nucl. Phy. A **921**, 114 - 130 (2014).

[20] D. J. Hinde, R du Rietz and M. Dasgupta, EPJ Web of Conferences **17**, 04001 (2011).

[21] D. J. Hinde, D. Hilscher, H. Rossner, B.Gebauer, M. Lehmann, and M. Wilpert, Phys. Rev. C **45**, 1229 (1992).

Chapter 8

Summary and concluding remarks

In this thesis work, a comprehensive study of heavy ion induced reactions in view of formation and decay process is carried out for variety of reactions lying in the mass range, A=28-268. In low energy nuclear reactions, the nuclear interaction potential is one of the important inputs to understand the related dynamics of the colliding partners. Therefore, emphasis is put to examine the behavior of different nuclear interaction potentials that help to address the dynamical evolution of heavy ion induced collision. In this thesis, semi-classical energy density formalism based Skyrme interactions and the proximity theorem based proximity 77 potential are used. The choice of Skyrme interactions are made from the work of Dutra *et al.* while proximity 77 is chosen for consistency in the earlier works. Using different nuclear interactions, the role of deformations, optimum orientations, excitation energy, angular momentum, isotopic (N/Z) and isobaric (Z) effect are investigated. A detailed description of reaction mechanism followed by formation and decay process is discussed in the chapter 1. To address the different reaction mechanisms, distinct methodologies are used. For the formation process, Wong and ℓ-summed Wong model are preferred while for the decay process, Dynamical Cluster-decay Model (DCM) is used. In the Wong and ℓ-summed Wong model, the penetration probability is defined in terms of barrier characteristics by Hill Wheeler approximation that helps to assess the total fusion cross sections. Whereas, in the DCM model,

penetration probability obtained using WKB approximation and the preformation probability, which is known to account the structural effects are used to determine the decay cross sections. The detailed description of methodologies is presented in chapter 2 with brief outline of interactions potentials. Using these methodologies, the reaction mechanisms of different compound systems are analyzed and the results are presented in chapters 3-7.

In chapter 3, the fusion dynamics of super heavy ^{268}Sg compound nucleus is analyzed at energies across the Coulomb barrier. The fusion-fission cross sections are reproduced using the Wong and ℓ-summed Wong model. The role of deformations and different Skyrme interactions such as SkT1, SIII and KDE0v1, SSk, GSkI are exercised to address the fusion hindrance phenomena perceived at sub barrier regime. In order to have better comparison with data, optimum orientations are employed within the ℓ-summed Wong formalism. It is observed that Cold polar orientation is preferred at sub barrier energies, while the above barrier regime seems independent of the structural effects as well as the choice of Skyrme interactions. The observation implies that among the chosen Skyrme forces, SSk (or equivalently GSkI) Skyrme force is more suitable to reproduce the experimental data. Therefore, using SSk and GSkI forces the cross sections are predicted at above and below barrier energies. Further, the effect of mass, deformations and orientations on the fusion dynamics of ^{12}C+^{154}Sm, ^{16}O+^{154}Sm, ^{28}Si+^{154}Sm and ^{48}Ca+^{154}Sm reactions is analyzed using Skyrme forces GSkI, SIII and the proximity potential mod Prox 88. The study shows that the fusion hindrance in below barrier region persists for SIII Skyrme force and it increases consistently with an increase in the projectile mass (charge). The hindrance to fusion path is treated to some extent by employing the cold orientation approach. On switching the choice of potential from SIII to generalized GSkI Skyrme force and proximity type mod Prox 88, the comparison with experimental data improves significantly.

In chapter 4, the complete analysis of ^{136,144}Nd compound systems in reference to fusion and decay process is carried out. As discussed in chapter 3, the SSk and GSkI

Skyrme force lead to similar result and seems more suitable for the study of reaction dynamics, therefore, in chapter 4, GSkI Skyrme force (either of the two forces) is carried forward to analyze the comparative behavior with SkT1, SkT2 and SIII Skyrme forces in the intermediate mass range. To address the hindrance phenomena in ^{40}Ca+^{96}Zr reaction, the GSkI force requires 1n-transfer effect at sub barrier energies while, other considered Skyrme forces perform consistently bad even after including 1n-transfer channel effect. However, for neutron rich case i.e. ^{48}Ca+^{96}Zr reaction no signature of fusion hindrance and transfer effect is observed and all the Skyrme forces reasonably addressed the excitation function across the Coulomb barrier. These calculations are performed using the Wong and ℓ-summed Wong model by incorporating the deformation effect. Further, the decay of $^{136,144}Nd^*$ so formed in $^{40,48}Ca + ^{96}\ Zr$ reactions is explored in the framework of DCM. Here, the calculations are carried out with GSkI and SkT1 Skyrme forces, which emphasis that mass distribution of out going fission fragments shows a drift from symmetric to relatively asymmetric distribution for GSkI and SkT1 forces respectively. Evidently from neck length parameter ΔR, it is confirmed that GSkI force performs better particularly at sub barrier region as it requires lesser barrier modification to address the experimental data as compare to SkT1 force.

The observations from chapter 3 and chapter 4 lead to consistent result that GSkI force is better for the addressal of reaction dynamics across the barrier. Also it seems suitable for the study of neutron rich cases and the stellar reactions. Therefore the validation of GSkI Skyrme force in conjunction with recently developed eMSL07 and the standardized SIII force is tested for light mass reactions. The decay of ^{28}Si* compound nucleus is examined using the dynamical cluster decay model at energies span 4-5 MeV. The observation shows that independent to the choice of Skyrme interactions and the incident energy light particles are emitted along with the npα like structure that dominates over xα structure. The excitation functions of n, p and alpha particle are decently addressed with generalized GSkI and eMSL07 forces, however the standardized SIII Skyrme force could not reproduce the experimental

data. Further, the analysis is carried for the ^{6}Li fragment which appears to be most probable fragment in the decay path of ^{28}Si* CN. The fragile nature of ^{6}Li further opens up two possibilities that whether it survive the stellar conditions of undergo segregation process. On the basis of these possibilities further calculations are performed using eMSL07 Skyrme as it requires lesser barrier modification in comparison to GSkI Skyrme force. The comparison of kinetic energy and Q value of the ^{6}Li nucleus signifies the possibility of disintegration of ^{6}Li into npα fragments. Moreover, the capture process seems possible due to positive Q values of the neutron, proton and alpha capture reactions.

Further, the role of Skyrme interactions is tested in view of a loosely bound projectile case, wherein complete and incomplete fusion processes start competing at above barrier energies. For this purpose, $^{6}Li + ^{238}U$ reaction is chosen because of three major reasons; firstly, ^{6}Li has low threshold/breakup probability, therefore it easily undergoes breakup process; secondly, the reaction is extremely asymmetric in nature that further enhances the breakup probability and lastly, it forms neutron rich compound system that seems to be suitable for the testing of NRAPR, SKRA , SQMC700, KDE0v1 and LNS Skyrme interactions in comparison to SIII and GSkI Skyrme forces. The barrier characteristics emphasized that KDE0v1 is identical to SIII Skymre force while NRAPR and SQMC700 are similar to GSkI force. Based upon the barrier profile NRAPR, SKRA and LNS forces cover wide range of barrier characteristics therefore chosen to illustrate the fission dynamics of $^{244}Am^{*}$ compound system. Using these Skyrme force, the fission cross sections of excited $^{244}Am^{*}$ compound system are calculated in the framework of dynamical cluster decay model over the energy ranging from $E_{c.m.}$ = 27.29 to 40.71 MeV. At higher energies, the DCM based calculations exhibit deviation from the experimental data which indicates the fusion suppression, that is addressed in terms of incomplete fusion (ICF) contribution. In view of this, calculations for ICF are performed using same Skyrme forces at relatively higher incident energies. Besides this, the

percentage barrier modification helps to provide useful information regarding the addressal of fusion hindrance. The force with small $\%\Delta V_B$ seems to be better in resolving fusion hindrance phenomena. Less $\%\Delta V_B$ suggests that there is more intrinsic barrier modification due to Skyrme force used as compare to extrinsic one. Thus, it is evident from ΔV_B variation that NRAPR and its identical SQMC700 and GSkI forces (having barrier characteristics similar to NRAPR) require lesser barrier modification and hence can be used as an alternate choice for estimating the nuclear interaction potential. Additionally, the cross sections are also predicted at energies below the Coulomb barrier using NRAPR Skyrme force with in the DCM.

Next, chapter 7 aims to carry out the detailed study on decaying fragments via analyzing the role of deformations, angular momentum, isospin (N/Z), isobars (only Z effect) on the decay path of heavy mass system. Also, the dynamical effects such as kinetic energy, velocity and time scale of the fission fragments are estimated. The nuclear interaction part is determined using the proximity based prox 77 potential. The calculations are performed for ^{170,174}Hf* nuclei, whose isobars ^{170,174}Pt* are available in the literature. The spherical choice of fragmentation results in symmetric distribution of fission fragments, which on adding the deformation effect gives rise to the clusters in heavy mass region. It is observed that isotopic effect is more pronounced in the case of Hf* nuclei than Pt* nuclei. Also, it is noticed that even-odd effect accompanied by deformations impart significant influence on the structures of Hf* systems. On the other hand, the transition in the potential energy surfaces of isobars indicates the influence of Z-effect on the fragmentation potential. The fusion excitation function for evaporation residue give decent agreement with experimental data. However, the fission fragments exhibit suppression in the cross sections at higher incident energies. This implies that non compound nucleus process may compete at higher energies. Further, the dynamical properties of fissioning nucleus ^{170}Hf* are analyzed, wherein the velocities of fission fragments and the dynamical time scale of fission fragments are calculated. The time scale of lighter fragment minimized in DCM is compared with fission time scale, which in turn suggests that

the emergence of lighter fragments is faster as compared to the fission fragments

This work can be extended for further study. The impact of surface properties such as nuclear radii, diffuseness parameter along with the bulk properties such as effective mass, incompressibility can be analyzed on the density as well as barrier profile of various colliding nuclei. Further, the contribution of CF and ICF processes can be distinguished using the appropriate methodology. In addition to this, the dynamics of non compound nucleus processes such as quasi fission and fast fission can be studied via angular momentum distribution effect.